Performance Characterization and Quantification of Dielectric Barrier Discharge Plasma Actuators

Vom Fachbereich Maschinenbau
an der Technischen Universität Darmstadt
zur
Erlangung des Grades eines Doktor-Ingenieurs (Dr.-Ing.)
genehmigte

D i s s e r t a t i o n

vorgelegt von

Dipl.-Ing. Jochen Kriegseis

aus Lahn-Gießen

Berichterstatter:	Prof. Dr.-Ing. C. Tropea
Mitberichterstatter:	Prof. Dr.-Ing. E. Moreau
Tag der Einreichung:	01.11.2011
Tag der mündlichen Prüfung:	07.12.2011

Darmstadt 2011
D17 (Diss. Darmstadt)

Hiermit versichere ich, die vorliegende Doktorarbeit unter der Betreuung von Prof. Dr.-Ing. C. Tropea und Dr.-Ing. S. Grundmann nur mit den angegebenen Hilfsmitteln selbständig angefertigt zu haben.

Darmstadt, den 1. November 2011,

Abstract

The present work is an attempt to improve the characterization and quantification of the performance of dielectric barrier discharge (DBD) plasma actuators for aerodynamic flow-control applications. Existing measurement and evaluation strategies, together with additional new approaches have been applied and are discussed extensively. Novel scaling numbers are introduced that yield universal and partly non-dimensional key quantities for an improved evaluation of the electrical discharge characteristics and of the environmental influences about the behavior of plasma actuators. The existing strategies to quantify the momentum transfer from the plasma to the surrounding air are reviewed and have been applied to achieve a comprehensive and comparative analysis of the respective differences based on experimentally obtained data. Direct and implicit as well as differential and integral force estimation approaches are discussed. To counteract influences of the environment on the discharge and thus assuring constant plasma-actuator performance, a closed-loop control circuit of the electrical setup is introduced and successfully demonstrated in a proof-of-concept experiment.

Kurzfassung

Ziel dieser Arbeit ist die Verbesserung der Charakterisierung und Quantifizierung des Arbeitsverhaltens von dielektrischen Barriereentladungsplasma-Aktuatoren im Hinblick auf Anwendungen zur aerodynamischen Strömungskontrolle. Bei den durchgeführten Untersuchungen kamen bestehende und neue Mess- und Auswertungsstrategien zur Anwendung, die ausführlich diskutiert werden. Es werden neuartige Maßzahlen eingeführt, die als universelle und teilweise dimensionslose Kenngrößen eine verbesserte Evaluierung der Leistungsfähigkeit von Plasma-Akuatoren gestatten. Mit Hilfe dieser neuen Kennzahlen ist sowohl eine zuverlässige Erfassung von Entladungszustand und -intensität als auch eine präzise Beurteilung der Umgebungseinflüsse auf das Verhalten des Plasma-Aktuators möglich. Im Rahmen einer umfangreichen Vergleichsstudie fanden Experimente zur Quantifizierung der Impulsübertragung vom Plasma auf die umgebende Luft statt. Dabei kamen alle aktuell exisitierenden Verfahren zur Anwendung. Sie werden auf der Basis der erhaltenen experimentellen Daten gegenüberstellend analysiert. Besondere Beachtung findet dabei sowohl die Trennung von direkten und indirekten Methoden als auch die Unterscheidung zwischen integralen und differentiellen Verfahren zur Bestimmung der Kraft. Um dem Einfluss der Umgebungsbedingungen auf die Gasentladung entgegenzuwirken, wurde das vorhandene elektrische Plasma-Aktuatorsystem um einen Regelkreis erweitert, dessen Wirksamkeit an einem Beispiel erfolgreich demonstriert wird.

Acknowledgements

First of all I want to thank my doctoral adviser Prof. Dr.-Ing. Cameron Tropea, who gave me the chance to accomplish my Ph.D project during my employment as a doctoral researcher at the Institute of Fluid Mechanics and Aerodynamics (SLA) and the Center of Smart Interfaces (CSI) of the Technische Universität Darmstadt. The infrastructure provided by him served as an excellent scientific environment for my research throughout the last five years. I would also like to thank Prof. Eric Moreau from the Université de Poitiers for refereeing this thesis.

A special word of thanks is owed to my mentor Dr.-Ing. Sven Grundmann for all the valuable advises and fruitful discussions. The frequent exchange of ideas and conclusions with him considerably improved the scientific level of the present work. In this context, I gratefully acknowledge the support of Dr.-Ing. Bettina Frohnapfel in the period, while Sven was not available in Griesheim.

Emphasis has to be placed on the pleasant climate at work, which consists of and is cultivated by the group of friendly people at the wind-tunnel facilities in Griesheim. In particular I wish to thank Dipl.-Ing. Andreas Güttler, Dr.-Ing. Matthias Kinzel, Dipl.-Ing. Lars Opfer and Dipl.-Ing. Andreas Reeh, who actually became good friends beyond work and research.

I am truly grateful to my students B.Sc. Tobias Corneli, Dipl.-Ing. Tobias Dehler, M.Sc. Imdat Maden, Dipl.-Ing. Benjamin Möller, Dipl.-Ing. Clarissa Schönecker (née Steffes), B.Sc. Daniel Schröter and B.Sc. Clemens Schwarz. With their work they reasonably contributed to my research. Further acknowledgement is dedicated to Dipl.-Ing. Katrin Barckmann, Dipl.-Ing. Jürgen Frey and Dipl.-Ing. Armin Kurz for the technical assistance using the wind-tunnel facilities in Griesheim and Dresden. Additional words of thanks go to Ilona Kaufhold, Martin Weiß and their workshop teams for the ongoing support concerning the experimental setups.

I would like to acknowledge the encouragement I have received over the years from all my friends and my family, especially from my parents. Finally, I wish to express my gratefulness to Isabel for all the love, patience, understanding and unconditional support during the last years.

Contents

1 Introduction

1.1 Motivation

Dielectric barrier discharge (DBD) plasma actuators have been proposed for a wide range of flow control situations, although they have yet to reach the true application stage. An overview of possible applications is provided by Moreau [155] or Corke *et al.* (e.g. [45, 46]). Despite the large number of recent publications on this topic, there still remain some very basic questions regarding performance, effectiveness and efficiency of these actuators, which up to now have only been addressed in an *ad hoc* or empirical manner. There are several reasons why these questions should now be answered more systematically and the present study examines especially the electrical quantities as a measure of actuator performance.

The first motivation for being more precise about how optimal an actuator is performing is simply to achieve the most effective flow control. For most applications the effectiveness of the actuator will depend on the momentum imparted into the boundary layer by the actuator and maximization of this quantity will normally be desirable and beneficial. However, another important reason for being more quantitative about the actuator performance is the increasing need to compare actuator designs and effectiveness between different research groups and geometric configurations. 'A widely accepted standard for plasma actuators does not exist', as recently reported by Little *et al.* [144] in the context of comparability. Up to now there have been no non-dimensional parameters suggested to characterize actuator operation and this renders direct comparison of results from different studies much more difficult. Finally, by quantifying the actuator performance, models for the induced body forces used in numerical simulations can be more realistic and can take into account the actual actuator operational conditions.

It is the objective of the present work, partly already published or presented [124–130], to provide guidelines how to characterize and quantify the performance of dielectric barrier discharge plasma actuators, thus contributing to an improved documentation and prediction of discharge-based flow control in aerodynamic applications.

1.2 Organization of the Thesis

Chapter 2 provides a brief introduction into plasma physics, broken down step by step from the general classification of plasmas to the gas-discharge application of DBD plasma actuators for aerodynamic flow control.

Chapters 3 and 4 address the discharge specific quantities involved in the operation of plasma actuators, i.e. electrical and optical characterization of the discharge. Existing methods are reviewed and extended to obtain novel quantities, which can serve as robust measures for the discharge performance and its quantification.

The momentum transfer of the discharge device to the surrounding air is discussed in Chapters 5 and 6. Direct thrust measurements as well as implicit body-force determination approaches are applied to provide a comprehensive overview of existing momentum transfer estimation strategies. Derived from differential and integral approaches the respective characteristics are extensively discussed in a comparative analysis.

The plasma actuator is commonly assumed to manipulate the airflow but not vice-versa. In Chapter 7 it is demonstrated that this in fact is an oversimplification. Moreover, a novel closed-loop circuit for the electrical plasma-actuator setup is introduced to counteract such performance changes and to assure constant performance regardless of the environmental influences.

State-of-the-art reports corresponding to the respective research topics as discussed in Chapters 3-7 are embedded in the introductory paragraphs and alongside the discussion of results and insights of the respective chapters to put the present work into context with respect to existing literature.

Finally, Chapter 8 summarizes the main insights and conclusions and gives an outline for possible future efforts to achieve further improvements of characterization, application and optimization of dielectric barrier discharges for aerodynamic flow control.

2 Dielectric Barrier Discharge Plasma Actuator

In Section 2.1 a brief overview is given concerning plasma characteristics and in particular dielectric barrier discharges in order to classify the DBD plasma actuator. Subsequently, in Section 2.2 working principles and typical applications of the DBD usage for flow control applications are described, which are finally classified and quantified with respect to performance and efficiency in Section 2.3.

To gain a more detailed and comprehensive insight into plasma physics and gas discharges the reader is referred to related literature (e.g. Raizer [182], Hollahan and Bell [100], Roth [189, 190]).

2.1 Physical Background

In physics and chemistry the term plasma describes fully and partly ionized gases and is also commonly known as the fourth state of matter. Since the transition from gas to plasma occurs smoothly, the latter state usually consists of electron gas, ion gas and neutral gas. Ionized gases span a wide range of thermodynamic properties and regimes, which can be found in different environmental scenarios as well as in various (industrial) applications. Therefore, further distinction and classification of plasmas is made in the following, to identify the characteristics of DBD plasma actuators within the property and parameter space of plasmas.

2.1.1 Classification of Plasma

At macroscopic scales plasmas are quasi-neutral, i.e. the concentrations of positive and negative charges are approximately equal (Hollahan and Bell [100]). At microscopic scales this is not necessarily the case, since despite the large-scale equality, space charges are possible within a particular range. The characteristic quantity to distinguish these two scales is the Debye

length

$$\lambda_D = \left(\frac{\varepsilon_0 k T_e}{n e^2} \right)^{\frac{1}{2}}, \tag{2.1}$$

where $\varepsilon_0 = 8.854 \times 10^{-12}$ C/(Vm) is the permittivity of free space, $k = 1.381 \times 10^{-23}$ J/K is Boltzmann's constant, T_e is the kinetic electron temperature, n is the electron number density and $e = 1.602 \times 10^{-19}$ C is the electronic charge. The Debye length λ_D defines the spatial range of a plasma, which can comprise a charge imbalance [100]. Furthermore, λ_D, referred to as Debye shielding distance, characterizes the thickness of sheaths, which form between plasmas and electrodes or walls (Roth [189]).

Plasmas are generally classified by their kinetic temperature T and number density of charged particles n. Such a classification is sketched in Figure 2.1 based on diagrams from Boeuf [25], Braithwaite [33], Hollahan and Bell [100], Jolibois [108] and Smirnov [207]. Since the kinetic temperature T specified in Kelvin [K] is an inconveniently small unit to quantify the plasma temperature [189], the relation

$$kT \equiv eT' \tag{2.2}$$

is commonly used to express the kinetic temperature T' in electron volt units [eV]. Hence, 1 eV is equivalent to 11604 K based on the conversion factor k/e. In contrast to the temperature T_g of neutral gases the different species of an ionized gas can (but do not necessarily have to) have significantly different temperatures. For (thermodynamic) equilibrium plasmas all electrons, ions and neutrals have identical temperatures $T_e = T_i = T_n$, which implies negligible amounts of energy fluxes within the gas. These requirements are not satisfied for non-equilibrium plasmas, where the electron temperature is in the range of $T'_e = 1 \ldots 10$ eV [26, 30], whereas the temperature of ions and neutrals does not exceed ambient temperature significantly, $T_i \approx T_n \approx T_g \gtrapprox 300$ K [182]. This difference between electron and gas temperature is illustratively demonstrated by Kunhardt [131], where the kinetic temperature of the neutral gas is shown to be insufficient to cause skin burn.

The charge number density n quantifies the number of charges within a particular volume of gas. The ratio

$$\alpha = \frac{n_i}{n_i + n_n} \tag{2.3}$$

of the number density of ions n_i and neutrals n_n defines the degree of ionization (Delobeau [50]). For weakly ionized gases ($\alpha \ll 1$) it can be

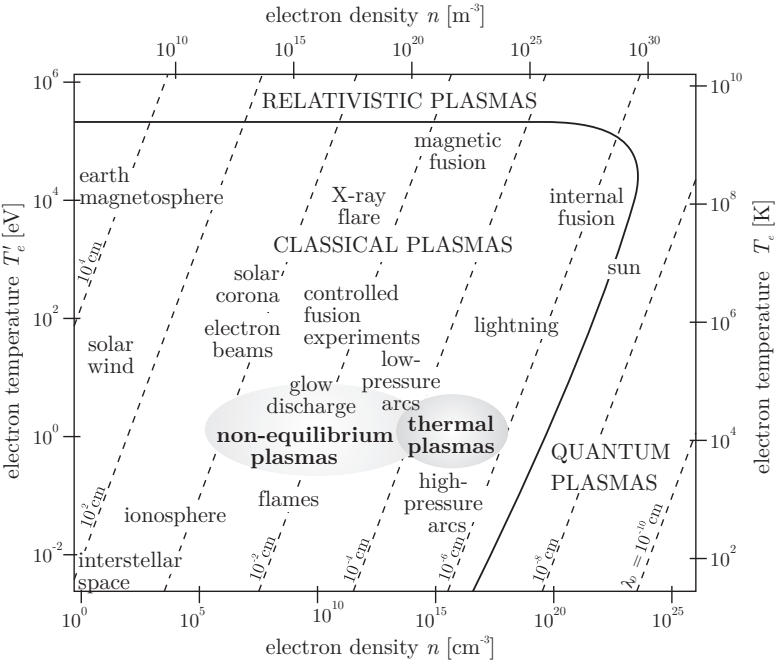

Figure 2.1: Two dimensional classification of plasmas characterized by electron number density n and electron temperature T_e (summarized from [25, 33, 100, 108, 207]).

assumed that collisions mainly occur between charged and neutral particles and those among charged particles can be neglected (Lifshitz and Pitaevskiĭ [140]). The number of momentum transferring collisions per time scales with the number of molecules within a given volume of gas as illustrated by Christophorou and Olthoff [41]. Therefore, the collision frequency ν_m is proportional to the density n_n and consequently to the pressure p of the gas

$$\nu_m \propto n_n \propto p, \tag{2.4}$$

but is to a first approximation no function of the collision velocity (Smirnov [206]).

Between two collisions the charges are accelerated in random directions. Provided the presence of an (uniform) external electric field $\vec{E}$, this random motion is superimposed by a systematic motion along the direction of the

field, which is referred to as drift (Raizer [182]). Averaging this motion over many collisions yields the drift velocity

$$\vec{v}_d = \begin{cases} \mu\vec{E}, & \text{for positive charges;} \\ -\mu\vec{E}, & \text{for negative charges,} \end{cases} \tag{2.5}$$

where the mobility

$$\mu = \frac{e}{m\nu_m} \tag{2.6}$$

is the proportionality coefficient between drift velocity and the electric field [182]. Due to their heavy mass m and the corresponding inertia, the mobility of ions is several orders lower than the electron mobility, i.e. $\mu_i \ll \mu_e$. Note that (2.5) is valid for any electric field strength, since in first approximation the mobility (2.6) is only a function of the collision frequency but independent of the absolute collision velocity [206].

2.1.2 Gas-Discharges

To better understand plasma actuators as gas-discharge devices, this Section provides some basic understanding of discharge states and mechanisms. Former research on gas discharges mainly concentrated on low pressure discharge tubes as depicted in Figure 2.2, which resulted in today's well-known fluorescent light tubes. For this relatively simple one-dimensional DC discharge of such tubes and reactors the corresponding mechanisms can be defined and distinguished precisely, as extensively described in the literature (e.g. Druyvesteyn and Penning [54, 55], Flügge [72, 73], Meek and Craggs [150], Raizer *et al.* [183], Roth [189, 190]).

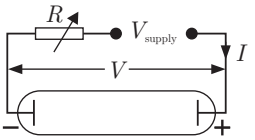

Figure 2.2: Electrical discharge tube (based on Francis [80]).

Plasma actuators, in contrast, are AC devices in the lower radio frequency (RF) range with inhomogeneous and at least two-dimensional electric fields. This implies more complexity for the corresponding discharge mechanisms and therefore does not allow an exact definition of the discharge properties. Despite this difference, the discharge mechanism of the

DC case can be assumed to properly describe the basics of the AC case as well (Gadri and Roth [84]) and therefore is shortly outlined in the following, closely based on the descriptions of Roth [189][1].

2.1.2.1 Voltage-Current Characteristic

Raising the voltage between the two electrodes of a low pressure discharge tube according to Figure 2.2 leads to a nonlinear voltage-current interrelation. A respective characteristic voltage-current curve is sketched in Figure 2.3, which contains different discharge regimes.

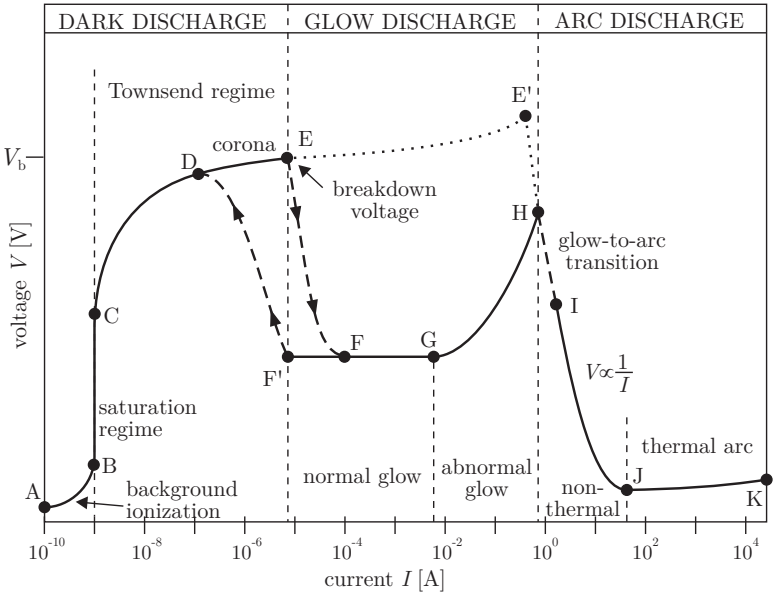

Figure 2.3: Characteristic voltage-current curve for DC low pressure electrical discharge tubes according to Roth [189].

Dark Discharges At very low applied voltage (A-B) only background radiation contributes charges to the current flow. In this *background ionization regime* an increasing amount of the thus generated charges

[1] It should be noted that in earlier literature (eg. Druyvesteyn and Penning [54], Francis [80], von Engel [228]) the nomenclature and the corresponding order of some discharge sub-regimes partly differs from the descriptions of the present work.

is accelerated towards the electrodes at increasing voltage. Once all charges produced by background ionization reach the electrodes there is a current stagnation in the *saturation regime* (B-C), in which the energy level is too low to create new (secondary) charges. In the *Townsend regime* (C-E) the electric field strength is high enough for the primary charges to partly ionize the background gas. Since the new charges as well acquire enough energy from the field to ionize the gas, discharge avalanches occur, which lead to an exponentially increasing current at increasingly applied voltage.

Unipolar *corona discharges* may occur in later stages of the Townsend regime, where between D and E a locally increased field concentration exceeds the breakdown field strength of the gas. These local concentrations are caused by sharp tips or edges or asperities of the electrodes. Apart from the exception of the corona discharge, the discharge of regime (A-E) remains invisible to the unaided eye and therefore is termed *dark discharge*.

Glow Discharges Once the breakdown voltage V_b is reached at point E, an electrical breakdown occurs followed by a transition (E-F) to the *glow discharge regime*[2]. The large potential difference between the electrodes collapses due to the significantly increased current flow and the plasma becomes visible. This transition is followed by the *normal glow discharge* (F-G), which is characterized by a current that is increased almost independent from the voltage over several orders of magnitude. Thereby, the plasma starts covering the cathode until the latter is entirely covered at point G. Beyond that point the discharge turns to an *abnormal glow* (G-H). Since the cathode is entirely covered, a considerably strong voltage increase is required to achieve an abnormally high current density at the cathode. This results in successively heated electrodes and an incandescent cathode at point H.

Following the voltage-current curve from point G to lower currents typically results in an hysteresis, since the glow discharge is maintained below F, once it has been established. At point F' the transition back to the Townsend regime occurs without running through the Townsend or corona discharge again.

[2]Note that the term *glow discharge* is often referred to as *silent discharge* in the English-speaking literature, which emerged as a translation error of the term *Glimmentladung* from the German literature of the 19$^{\text{th}}$ century (e.g. Andrews and Tait [10], Eliasson and Kogelschatz [59]). See Roth [190] (p.43) for more details.

Arc Discharges Between H and I the *glow-to-arc transition* takes place under thermionic emission of electrons from the highly heated cathode. This transition is followed by the regime of *non-thermal arcs* (I-J), where the voltage required for the discharge decreases rapidly due to the additional charges form the thermionic emission. Since this influence increases with increasing electron heating, the effect corresponds to a negative resistance characteristic. Beyond the (local) voltage minimum at point J the voltage-current curve rises again in the regime of *thermal arcs* (J-K) towards thermal equilibrium at point K.

As mentioned at the beginning of this section, the above introduced discharge characteristic mainly describes low pressure discharges. For high (ambient) pressure levels and further inhomogeneous electric fields a direct arc breakdown can occur, which is maintained at sufficient current delivery. These types of discharges are indicated with the dotted branch and point E' in Figure 2.3. Depending on geometric and gas conditions a direct transition from Townsend or corona discharge to arc discharge (E'-I) is possible as well (cp. Loeb [146]).

2.1.2.2 Breakdown Voltage and Paschen Curve

The breakdown voltage V_b (ignition potential) is specified by point E in Figure 2.3. It is an instability of the system resulting in discharge and high current flow. Before that point (C-E) discharge is only possible by means of secondary electron emission. Beyond point E the ionization avalanche provides a sufficient amount of electrons to maintain a self-sustained discharge [212].

The breakdown voltage V_b and corresponding electric breakdown field $\vec{E}_b$ depend on the electrode material, geometry and distance d, the gas species and the pressure p. In the year 1889 Paschen [169] reported that for a given gas the breakdown voltage V_b is only a function of the product pd. In particular, he concluded that the ignition potential depends on the number of molecules between the electrodes - independent of the pressure-distance combination. An example for this empirical relationship is shown in Figure 2.4, which comprises the so-called Paschen curves for different gases.

For all gases there exists a minimum breakdown voltage $V_{\mathrm{b}_{\mathrm{min}}}$ for a specific value of pd, which corresponds to the Stoletow point of most efficient discharge properties (Raju [184]). According to Corke *et al.* [44], the RF

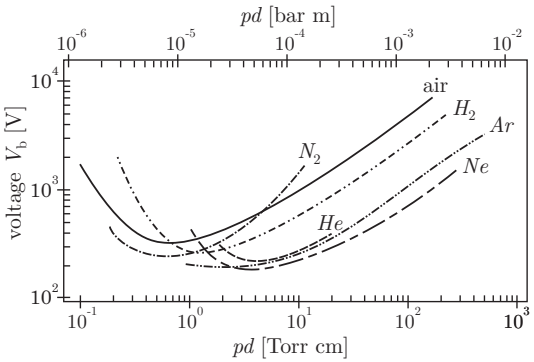

Figure 2.4: Paschen curves for different gases (according to Vollrath [227]).

glow discharges operate at the Stoletow point.

2.1.3 Dielectric-Barrier Discharge Plasma

Dielectric barrier discharge (DBD) setups are characterized by at least one insulating dielectric layer, which is placed between the electrodes [116]. Since DC current cannot pass this barrier, an AC operation is required for DBD operation [115]. However, the advantage of an AC barrier discharge is the possibility to insulate the electrodes from the discharge volume, separated by the discharge chamber itself [183]. This can be especially advantageous when, for instance, highly aggressive gases are considered.

In contrast to most other non-equilibrium discharges the dielectric barrier discharges are non-equilibrium gas discharges that can be operated at elevated pressures ($10^{-1} \ldots 10^{1}$ bar) [59]. One of the first reports of a dielectric barrier discharge was published in 1857 by Siemens [202] who observed a glow between two coaxial glass tubes while generating ozone. Since the electrodes of his experimental apparatus were outside the tubes, covered by the glass as a dielectric material, strictly speaking this arrangement produced a DBD plasma.

Today's importance of dielectric barrier discharges is demonstrated by the variety of DBD-based applications in many branches of industry. The field of applications mainly comprises ozone generation, gas depollution, ultraviolet exclaimer and fluorescent lamps, discharge lasers, surface treatment and display panels as comprehensively summarized by Kogelschatz

[115]. An extract of possible geometric configurations is given in Figures 2.5 and 2.6 for volume discharges (VD) and surface discharges (SD), respectively.

The most salient difference between these two electrode-dielectric arrangements is that in the case of VD the breakdown occurs across a gas gap, whereas SD periodically grows on the dielectric [87]. Note that the presence of a dielectric layer is inevitable for any formation of surface discharges, since the insulation prevents from reasonable current flow [83]. The consequences of this difference on the discharge behavior and the corresponding electrical properties will be extensively discussed in Chapter 3.

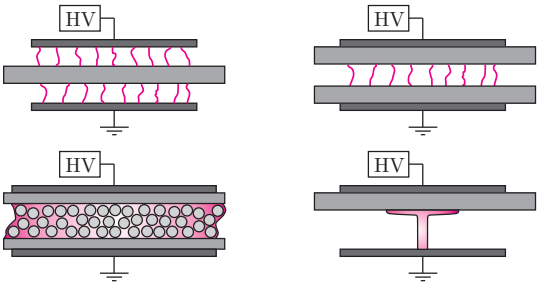

Figure 2.5: Basic volume dielectric barrier discharge configurations; ■ electrodes, ■ dielectric, ■ plasma (summarized from Allégraud [7], Gibalov and Pietsch [87] and Kogelschatz [115]).

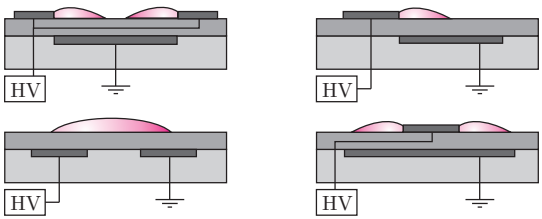

Figure 2.6: Typical surface dielectric barrier discharge configurations; ■ electrodes, ■ dielectric, ■ carrier material, ■ plasma (summarized from Guaïtella [99], Stanfield [211] and Temmermann [215]).

Table 2.1: discharge specific properties and parameters characterizing DBD plasma actuators for flow control.

near atmospheric pressure weakly ionized gas non-equilibrium plasma	$p = 10^{-1} - 10^{1}$ bar $\alpha = 10^{-4} - 10^{-3}$ $T_e' = 1 - 10$ eV, $T_i, T_n \approx 300$ K ($\hat{=}$0.0259 eV)
operating voltage operating frequency wave type	$V = 1 - 50$ kV $f = 0.2 - 25$ kHz sine, square, triangle

2.1.4 Characterization of DBD Plasma Actuators

The discharge regime of plasma actuators usually is classified as a (slightly filamentary) glow discharge within the group of non-equilibrium plasmas, in which the electron temperature is about two orders higher than ion and neutral temperature ($T_e' = 1 - 10$ eV, $T_i, T_n \approx 300$ K $\hat{=}$0.0259 eV). According to the low degree of ionization ($\alpha = 10^{-4} - 10^{-3}$, [25]), the DBD of plasma actuators produces a thin volume of a weakly ionized gas [18], where the number density of charges is around $n = 10^{16}$ charges/m^3.

Plasma actuators for flow control are usually operated at voltages and frequencies in the range of $V = 1 - 50$ kV and $f = 0.5 - 25$ kHz, respectively, where the AC signal usually is a sine, square or triangle wave. Corresponding to the respective flow-control purpose, the gas pressure p ranges between the order of 10^{-1} bar for flow-control under cruise flight conditions (e.g. [20, 236]) and 10^{1} bar for internal flow control in compressors and turbines (e.g. [225, 226]).

The typical range of plasma parameters and properties characterizing the surface discharge of DBD plasma-actuator operation is summarized in Table 2.1.

2.2 Application as Flow-Control Device

One of the first reports of discharge-based flow control was published in 1968 by Velkoff and Ketcham [224]. They demonstrated the effect of electrical fields on fluid boundary layers by means of corona wires, which were placed a small distance from the surface of a flat plate. In the 1990s the group of John Reece Roth at the University of Tennessee developed

a new way to generate uniform surface dielectric barrier discharge, which was referred to as a *One Atmosphere Uniform Glow Discharge Plasma* (OAUGDP^{TM}). This new type of plasma is protected by a US patent since 1995 [188]. The first flow-control results based on OAUGDP^{TM} were published by Roth *et al.* [191] in 1998.

Today, flow control using barrier- and/or corona-discharge based plasma actuators is of great interest for a wide range of aerodynamic applications. Plasma-based control devices become especially attractive when moving parts have to be avoided and a fast time response is required for the flow-control application. Advantages and disadvantages of plasma actuators are discussed alongside other actuators for active flow control by Cattafesta and Sheplak [36].

2.2.1 Plasma-Actuator Working Principle

The key feature of any plasma actuator's working principle is the momentum transfer from accelerated ions to the surrounding neutral gas by particle-particle collisions. Despite their high drift velocities, the momentum-transfer contribution of electrons is negligible due to the infinitesimal mass. The momentum transfer to the airflow is typically referred to as plasma-actuator body force or volume force.

Since plasma actuators are operated with AC voltages, the underlying electrical field periodically changes its sign. The consequences of this periodic sign conversion have led to ongoing debates concerning momentum-transfer details with partly contradictory explanations concerning the working principles. According to Font *et al.* [75] and Porter *et al.* [177], for instance, the main discussion centers about the question about the temporal nature of the actuation. The community has still not reached an agreement about whether the plasma strongly pushes (accelerates) the flow downstream during one half cycle and weakly pulls (decelerates) it upstream in the other half cycle, or whether the plasma pushes the flow downstream in both half cycles. Correspondingly, the two opposing theories are referred to as the *push-pull theory* and the *push-push theory*. Reports supporting the push-pull theory are e.g. given by Font *et al.* [77] and Porter *et al.* [177]. The push-push theory is endorsed e.g. by Baird *et al.* [13], Boeuf *et al.* [28] and Font *et al.* [75]. Both cases are possible according to reports of Enloe *et al.* [62] or Likhanskii *et al.* [141], for instance. However, the details of this debate go far beyond the scope of the present work. Therefore, to gain a more detailed insight into the description and modeling approaches at microscopic scales, the reader is referred to appropriate literature (e.g.

Boeuf *et al.* [28, 29], Lagmich *et al.* [134], Likhanskii *et al.* [142, 143], Macheret *et al.* [147], Singh and Roy [204, 205]).

Another issue that arises alongside the above controversy is the difference of scales. The typical spatial and temporal scales of gas-discharge processes are $4 - 8$ orders smaller than those of the resulting airflow scenario (Shneider *et al.* [200]). At spatial and temporal scales relevant for aerodynamic flow-control in first approximation the body force imparts a quasi-steady momentum to the surrounding airflow. As a result, the flow field changes such that a quasi-steady wall jet is developed under quiescent air conditions or an existing velocity profile is steadily manipulated, which is sketched in Figure 2.7. This characteristic behavior is the core of any flow control application, where the purpose is the achievement of reasonable improvement of the respective flowfield properties by means of dielectric barrier discharges.

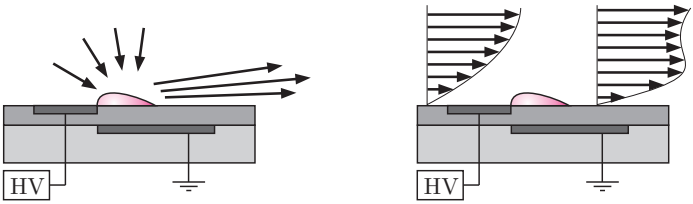

(a) quiescent air (b) boundary layer

Figure 2.7: Sketch of the airflow behavior generated by plasma-actuator operation; (a) wall-jet formation under quiescent air conditions, (b) manipulation of an existing boundary layer.

2.2.2 Fields of Application

Since its introduction by Roth *et al.* [191] the DBD based flow-control concept has been widely investigated for a large number of different applications. Plasma actuators have been proposed for a wide range of flow control situations, although they have yet to reach the real application stage. In recent years, plasma actuators have proven to be an attractive and promising alternative to conventional flow-control devices [36] and therefore enjoy increasing importance for various flow control scenarios in the community. The variety of investigated flow-control applications ranges from velocities of a few meters per second [94] to supersonic conditions [138].

Most research groups are concentrating on the different topics of external flow control, such as transition control (e.g. Grundmann *et al.* [98], Séraudie *et al.* [199]), separation control (e.g. Jolibois *et al.* [109], Patel *et al.* [170], Post and Corke [180]), wake control (e.g. Wilkinson [235], Soldati [208], Kozlov and Thomas [119, 120]). However, recent publications (e.g. Lemire *et al.* [136], Li *et al.* [139], Grundmann *et al.* [95]) have demonstrated the universality of plasma actuators for internal flow control as well.

Moreau [155] has provided an excellent review of the actuators' working principle and ongoing experimental and computational research on this topic, where in particular the specific differences of corona, DBD and sliding discharges are extensively described. Furthermore, Corke *et al.* [43, 45, 46] frequently review ongoing DBD-based flow-control research from a North American point of view.

2.3 Classification of Performance and Efficiency

2.3.1 Performance Characteristics

The basis for a robust quantification of the plasma-actuator performance is the identification of convenient measures appropriate to characterize particular performance states. Roth and Dai [192] introduced a power-flow diagram, which considers reactive power, dielectric heating and plasma maintenance, to yield a phenomenological summary of power losses inevitably accompanying the plasma actuator operation. To meet the requirements of any quantification purpose from such a power-flow, measurable quantities have to be defined as intermediate power stages.

In the present work the power flow is subdivided into four individual stages to characterize the performance steps relevant for flow control by means of plasma actuators.

Input Power Any discharge-based control device requires an energy source, which delivers electrical input power P_{input} to the chosen HV transformer. Many research groups use commercial laboratory power supplies as a voltage source, but (rechargeable) batteries are essential when thinking about flow control of drones or other unmanned aerial vehicles (UAVs) at application level, as demonstrated by Grundmann *et al.* [94].

Actuator Power A major characteristic of plasma-actuator performance

is the electrical actuator power P_A available at the discharge region. This value is a key quantity for any discharge application (see Manley [149] or Kogelschatz [115] for instance) and can be precisely quantified, as will be demonstrated in Chapter 3.

Fluid Mechanic Power Independent of the flow-control application the momentum transfer from the discharge to the air results in a modified airflow. The respective power supplied to the air can be characterized by the fluid mechanic power P_{FM}, which is available for flow control. Depending on the chosen measurement technique some research groups can only specify the resulting thrust F instead of a power value. This distinction is discussed extensively in Chapter 5.

Power Saving The desired result of energy-balance motivated flow-control applications is the achievement of best possible power savings P_S. Possible non-energetic-motivated flow-control applications are an advanced maneuverability of UAVs, for instance. In such cases, flow control success can not directly be measured in terms of power but rather in terms of extent of new flight regimes. The power saving P_S serves as a measure for the success of the flow-control efforts and states the final step of the power flow, which has to be defined individually for the particular flow-control application.

Although a detailed discussion of this quantity goes beyond the scope of the present work, it is listed here for the sake of completeness.

The resulting power-flow diagram according to the above stated power steps is sketched in Figure 2.8. Furthermore the diagram contains the corresponding efficiency chain, which is described in the following paragraph.

2.3.2 Definition of Efficiencies

In addition to the different power values, further important key values are the corresponding efficiencies, which connect the different power stages. According to the power-flow scheme of Figure 2.8, a chain of efficiencies can be defined by pairwise calculating the ratio of two performance values.

The resulting overall performance of plasma-actuator systems depends on various kinds of factors. Among others, these are input parameters (energy source, HV transformer, applied waveform for discharge), the geometrical arrangement (length, width and thickness of electrodes and dielectric), further actuator configurations (floating electrode, electrode design

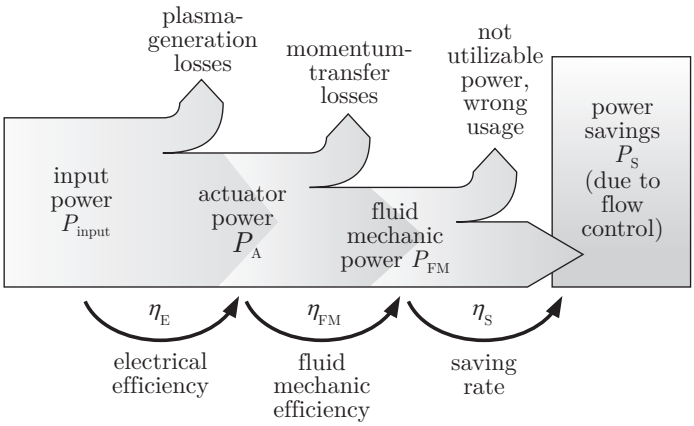

Figure 2.8: Power-flow diagram of plasma-actuator operation.

and quantity) or environmental influences (weather conditions, state variables). This variety of influencing parameters demonstrates the necessity to distinguish between different types of efficiencies to quantify and optimize plasma-actuator operation.

Based on the power characterization of Section 2.3.1, the efficiency chain takes the following three links into account. Note that the term *efficiency* η in the present work is strictly defined as a non-dimensional value in the range $0 \leq \eta \leq 1$. All dimensioned coefficients and those that can exceed the value 1 are indicated by an additional asterisk (η^*) and apostrophe (η'), respectively.

Electrical Efficiency The electrical efficiency is defined by the ratio of the two electric measures P_{input} and P_A according to

$$\eta_{\text{E}} = \frac{P_A}{P_{\text{input}}}. \tag{2.7}$$

η_{E} is specified by the power losses occurring during plasma generation, which is dominated by internal heating of the chosen HV transformer and losses in the dielectric barrier. It will be shown in Section 3.3 that η_{E} is not only affected by the properties of the power supply units but also depends on the properties of the load connected. Therefore, this efficiency can be optimized by appropriate impedance

matching (Singh and Roy [203]) or proper choice of the dielectric material (Roth and Dai [192]).

Fluid Mechanic Efficiency In 1960 Robinson [187] defined the fractional efficiency of electrokinetic conversion in case of the movement of air in the electric wind of the corona discharge as the relation of the kinetic output power to the electrical input power. Based on this report, to determine how efficient the electrical power is transferred to the fluid, the fluid mechanic efficiency is defined as

$$\eta_{\mathrm{FM}} = \frac{P_{\mathrm{FM}}}{P_A}. \tag{2.8a}$$

Similar definitions have already been used accordingly in various reports (e.g. Giepman and Kotsonis [88], Janssen *et al.* [106], Jolibois *et al.* [110], Léger *et al.* [135]). The main contributing losses characterized by η_{FM} arise from thermal radiation, chemical reactions and sound/light emission.

Given that the fluid mechanic power P_{FM} cannot be determined (typically due to a missing velocity information), a convenient and frequently applied replacement is the actuator thrust (e.g. Gregory *et al.* [92], Porter *et al.* [179], Enloe *et al.* [60]). Consequently, as a convenient replacement for the fluid mechanic power P_{FM}, the actuator thrust F is utilized to define a dimensioned measure of the fluid mechanic effectiveness as

$$\eta^*_{\mathrm{FM}} = \frac{F}{P_A}. \tag{2.8b}$$

The distinction between efficiency and effectiveness according to (2.8) has been proposed by Durscher and Roy [57] and Ferry *et al.* [71], for instance, and will be discussed in Chapters 5 and 6 in depth.

Saving Rate The last link of the efficiency chain purely depends on the level of successfully conducted flow control. Although being a non-dimensional number, the saving rate

$$\eta'_{\mathrm{S}} = \frac{P_S}{P_{\mathrm{FM}}} \tag{2.9}$$

is not referred to as an efficiency, since it ideally exceeds the value of one. η'_{S} has a wide range of possible physical interpretations, in which

every flow-control application requires an individual definition of the governing quantity P_S. Byerley [35] and Donald [51], for instance, want to increase the operating efficiency of a turbine component by reducing or eliminating a separation (bubble) and reducing profile losses. Jukes and Choi [113] define η'_S (referred to as 'power saving ratio' in [113]) as the ratio between power savings due to drag reduction and the fluid mechanic power imparted to the flow.

The sensitivity of η'_S in terms of drag reduction is emphasized by the work of Grundmann *et al.* [96–98]. They achieved a considerable transition delay by means of plasma actuators only for a particular electrode arrangement. In subsequent characteristic diagnostics of the actuator's immediate vicinity Kriegseis *et al.* [121, 122] identified adverse/favorable flow patterns to be responsible for the failed/successful transition delay under otherwise constant operating conditions, i.e. power consumption of the applied flow-control device.

The three (efficiency) coefficients (2.7-2.9) yield an overall effectiveness of the DBD plasma actuator as a flow-control device according to

$$\eta'_{FC} \;=\; \eta_E \, \eta_{FM} \, \eta'_S . \tag{2.10}$$

To exceed the break-even point of the energy-balance, $\eta'_{FC} = 1$ is desired for any profitable flow-control device, i.e. plasma-actuator operation saves energy costs.

In contrast to energy-balance motivated flow control, promising applications of plasma actuators as flow-control devices of course are unmanned aerial vehicles, such as drones or missiles. Independent of energy costs one major objective of such flow-control projects is an improved maneuverability, i.e. to facilitate formerly impossible flight regimes.

The major objective of the present work is the identification, implementation and evaluation of plasma-actuator quantification strategies. Such methods to quantify the actuator performance are essential for advanced flow-control research beyond the level of feasibility studies. Therefore, the present work may serve as a common guideline of performance quantification strategies before splitting into the specific branches of flow-control applications. As mentioned above, the two quantities P_S and η'_S extremely depend on the respective flow-control objective and will hence not be further discussed.

3 Electrical Quantification

The electrical performance of plasma actuators is mainly characterized by the electrical power which is consumed to maintain the discharge. In Section 3.2 a powerful and well-established means to quantitatively analyze dielectric barrier discharges is introduced and discussed and scaling laws are derived from the presented results. Only minor attention has been paid so far to the influence of the discharge on the electrical circuit of the discharge device. It will be demonstrated in Section 3.3 that accurate knowledge of the discharge-intensity dependent resonance frequency of this device is essential for optimization purposes such as impedance matching or control-circuit design of active flow-control devices. Emphasis will also be put on a proper capacitance determination of the operative plasma actuator (Section 3.4), in order to allow advanced impedance matching of the entire electrical setup. The significance of impedance matched systems for optimal energetic efficiency was identified by Chen [38] and emphasized by Singh and Roy [203].

To date, at least in terms of optimization and quantification, little attention has been directed to the electrical quantities of the actuator operation, such as operating voltage V, frequency f, consumed electrical power P_A and corresponding capacitance C of the plasma actuator. However, the electrical efficiency η_{E} may in itself be an important parameter. One good example is the application of plasma actuators for in-flight flow control, where weight and power consumption is of utmost importance, as demonstrated by Grundmann *et al.* [94].

3.1 Experimental Procedure

The experimental setup used in this investigation is sketched in Figure 3.1. Three different HV generation systems and three spanwise different plasma actuator lengths L were used, as specified in Table 3.1. This ensures that the conclusions derived from the study are robust and not geometry or apparatus specific. Since the influence of the upper electrode size is negligible, as demonstrated by Möller [154], the dimensions $w_1 = 2.5$ mm, $w_2 = 10.0$ mm and $d = 0.4$ mm (Kapton®, five tape layers) were chosen for upper

and lower electrode and the dielectric thickness respectively. This particular parameter combination has been used in numerous previous studies and has turned out to be very effective in transition delay experiments by Grundmann and Tropea [97] and for subsequent characteristic diagnostics presented by Kriegseis *et al.* [121, 122].

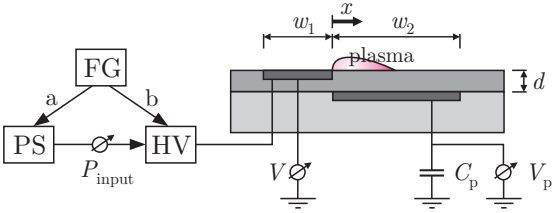

Figure 3.1: Experimental plasma-actuator setup comprising function generator (FG), low voltage power supply (PS), high voltage (HV) transformer and plasma actuator; components are listed in Table 3.1, component-specific wiring is indicated by arrows (a,b).

The measurement setup comprises an oscilloscope (LeCroy WaveJet354, 4CHs, 500kp/Ch, 1GS/s) to record the (AC sine-wave) operating voltage V (Testec HVP-15HF, 1000:1) and the probe voltage V_p (LeCroy PP006A, 10:1) of the charge-probe capacitor $C_p = 22$ nF. The choice of this particular value turned out to be appropriate for the measurements, which will be explained extensively in Section 3.4.4.

For subsequent calculation of the electrical efficiency η_E according to (2.7), the electrical input power

$$P_{\text{input}} = V_{\text{input}} I_{\text{input}}, \tag{3.1}$$

which supplies the high-voltage transformers, is measured using two multimeters (Extech Instruments EX530). The electrical setup and it's corresponding arrangement are included in Figure 3.1.

Table 3.1: HV-generator setups chosen. The codes of column 2 are used to abbreviate experimental details in many of the legends below and to precisely define the experiments throughout the document[1].

Device	Code	Specifications
Function Generator (FG)		ELV MFG 9001M
low voltage	1	Voltcraft PS 3610
Power Supply (PS)	2	Kenwood KRF-V6010
High-Voltage (HV)	I	GBS Elektronik Minipuls 2
transformer	II	Bosch automotive ignition coil
	III	GBS Elektronik Minipuls 1
plasma actuator length	A	$L = 0.15$ m
	B	$L = 0.30$ m
	C	$L = 0.45$ m
wiring	a	FG→PS (for II)
	b	FG→HV (for I and III)

3.2 Power Consumption

3.2.1 Calculation of the Power Consumption

The consumed electrical power P_A as a function of the operating voltage V is an established measure to describe the electrical characteristics of the plasma actuator, as the examples in Figure 3.2 demonstrate. However, the universality of these results is limited, since they are obtained using different operational settings, such as, for instance, different HV transformers, varying actuator lengths and materials, electrical settings such as voltages and frequencies as well as variations of the state variables.

Grundmann and Tropea [98] and Borcia *et al.* [31] explain two common ways of calculating the consumed electrical power of an actuator by determining the operating voltage and either the current I or the charge Q by means of a probe resistor or capacitor, respectively. Furthermore, Grundmann *et al.* [98] conclude that it is more convenient to choose the capacitor

[1]Label-code example: An experimental setup comprising the Voltcraft power supply, the GBS transformer, an actuator of length $L = 0.45$ m, and a direct wiring of the function generator to the transformer is labeled *1ICb* followed by a particular parameter setting, e.g. 10 kV or 14 kHz.

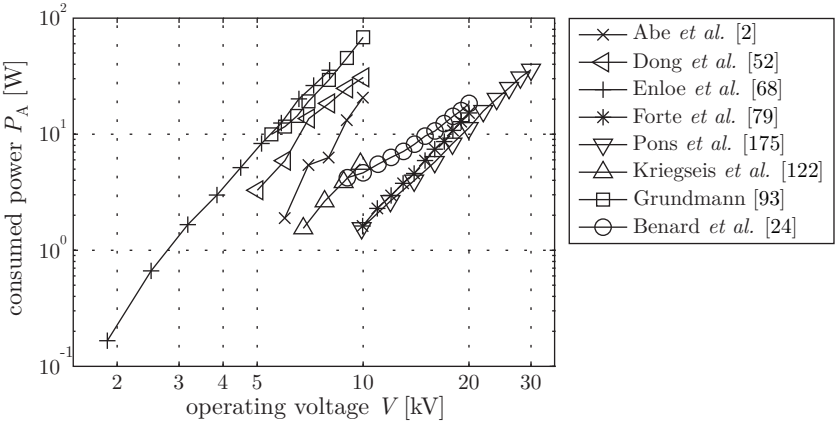

Figure 3.2: Graphical review of published $V - P_A$ relations.

concept, since the capacitor integrates the current passing through the actuator in time and thus captures all occurring micro-discharge pulses with an appropriate probe capacitor (see Section 3.4.4), which leads to a better signal-to-noise ratio compared to the resistor measurements. Independent of the bandwidth of single discharge events the measured probe voltage V_p across the probe capacitor C_p is proportional to the charge crossing the electrodes, i.e.

$$Q(t) = C_\mathrm{p} V_\mathrm{p}(t), \tag{3.2}$$

and the capacitance is simply a proportionality factor (cp. Figure 3.1). The measured operating voltage and charge values are plotted against each other in Q-V cyclograms, which are better known as Lissajous figures. Figure 3.3 shows such figures for two different dielectric barrier discharge types: the volume discharge (VD) including a gas gap, and the surface discharge (SD) as it occurs with DBD plasma actuators. Despite the fact that the signal-to-noise ratio of cyclogram-based measurements is much better than that of a direct measurement of the discharge current, further post-processing of the raw data, including filtering, becomes necessary in order to extract robust information from the cyclogram. Therefore, a least-squares filter based on the description of Savitzky and Golay [198] is chosen to prepare

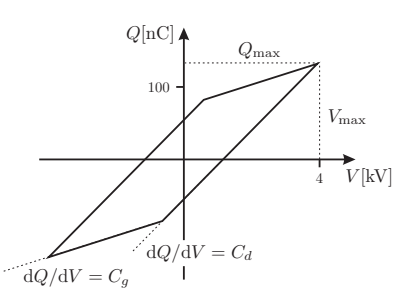

(a) volume discharge (VD); following Wagner *et al.* [229]

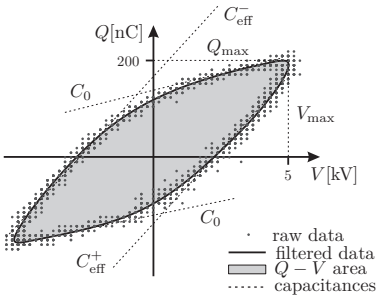

(b) surface discharge (SD)

Figure 3.3: Typical $Q-V$ cyclograms (Lissajous figures) of dielectric barrier discharges (DBD) with typical operating parameters; Characteristic quantities such as $V_{\max}$, $Q_{\max}$ and different capacitances - VD (a): C,C_{d}; SD (b): C_0,C_{eff}.

the raw data for further post-processing, as indicated in Figure 3.3(b).

The energy E_k, which is consumed per discharge cycle k, is defined by the area enclosed by the cyclogram and can be calculated by

$$E_k = \oint_k Q(t)\mathrm{d}V. \tag{3.3}$$

Subsequent multiplication of the energy E_k with the operating frequency f leads to the consumed actuator power

$$P_{A,k} = E_k f. \tag{3.4}$$

To calculate the power consumption P_A based on the measured time traces of $V(t)$ and $V_p(t)$, equations (3.2) - (3.4) are combined. Further averaging over K discharge cycles leads to

$$P_A = Ef = \frac{f}{K}\sum_{k=1}^{K}\oint_k C_{\mathrm{p}} V_{\mathrm{p}}(t)\mathrm{d}V \tag{3.5}$$

as the relevant equation for the quantification of the power consumption of plasma actuators.

Depending on the adjustment of the oscilloscope (500 kp/Ch, 1 GS/s) the measured time traces result in $K \approx 800$ cycles á 625 data points at a given plasma frequency 4kHz $< f <$ 18kHz. The corresponding standard deviations of the calculated power values lie below 3% in all cases ($\sigma_{P_A} <$ 3%).

Regarding the shape of a Lissajous figure, volume discharges (VD) lead to a parallelogram, since the discharge starts and stops with constant geometrical plasma shape, as sketched in Figure 3.3(a). This cyclogram was already discussed by Manley [149] in 1943 and is still an important diagnostic tool for DBD research, as recently demonstrated e.g. by [70, 87, 159, 229]. Unfortunately, volume discharges are seldom used for flow control, since at least one electrode must be located in the flow [171, 192].

Any surface discharge (SD) continuously changes the shape of its discharge volume throughout each cycle and thus changes its discharge capacitance as mentioned by Gibalov and Pietsch [87]. This effect results in an almond-shaped cyclogram, as sketched in Figure 3.3(b), which is well-known from various publications (e.g.[98, 155, 175]).

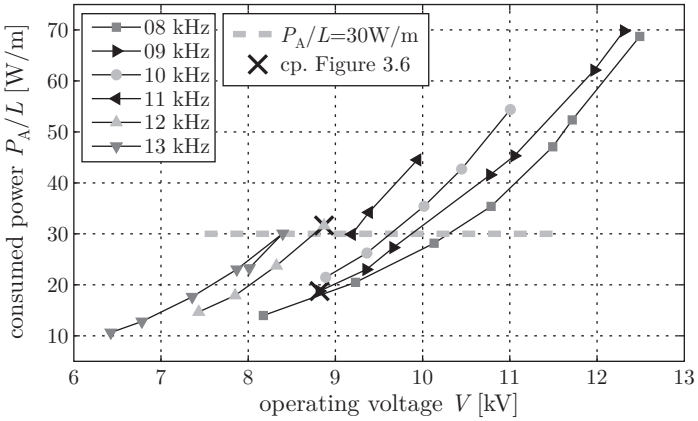

Figure 3.4: Power consumption P_A as function of operating voltage V for several frequencies f.

The results of power consumption calculations according to (3.5) are shown in Figure 3.4 for several operating voltages V and frequencies f, but one and the same actuator geometry (*1ICb*). It is obvious that the required operating voltage for a particular power level P_A increases with

decreasing frequency f, as emphasized by a gray dashed iso-power level in Figure 3.4. This conclusion is in good agreement with Roth and Dai [192], Dong *et al.* [52] or Forte *et al.* [79], for instance, and indicates the considerable influence of the chosen operational settings on the resulting actuator performance. Therefore, Figure 3.4 demonstrates the requirement defining appropriate scaling laws for the prediction of the plasma actuator's power consumption P_A. This will be discussed extensively in the following section taking all parameters in Table 3.1 into account.

3.2.2 Power Law Characterization

To date, the electrical power P_A consumed by plasma actuators is typically characterized as a power-law based function of either frequency f or operating voltage V. Although the exponents of these functions describe in principle the performance of the actuator, they are not comparable among different experiments or configurations. This underlines the need for more straight-forward and universal scaling laws.

A selection of previously published results that describe such $P_A = f(V)$ relations has been shown in Figure 3.2. Some research groups use a quadratic approximation [52, 175] (with and/or without offset) for the consumed power with increasing operating voltage V. Other groups report exponent values ranging between 2 and 3 [109, 192] or approximately 7/2 [68, 69, 144, 167], depending on the geometry of the actuator and the experimental configuration. A comparison of these published values with calculations from the present work confirmed approximately an exponent value of 7/2, which can be derived from Figure 3.5 for several geometrical and operational configurations (cp. Table 3.1). Note that the value 7/2 is derived through empirical fitting and does not suggest a physical explanation here.

Additionally, the relative power per unit actuator length, P_A/L, is plotted in Figure 3.5(b), in contrast to the absolute values of Figure 3.5(a), as published by various research groups (e.g. Grundmann and Tropea [98], Jolibois *et al.* [109] or Little *et al.* [144]). For this relative description, the results obtained for different actuator lengths lie approximately on top of one another when operated at the same frequency. Despite this improvement in terms of universality, there still remain significant differences for changes of the plasma frequency f, since P_A is a function of the frequency as well.

Most research groups (e.g. [1, 17, 52, 79, 175, 177]) describe this power-frequency function as a linear function ($P_A \propto f$). However, independent of

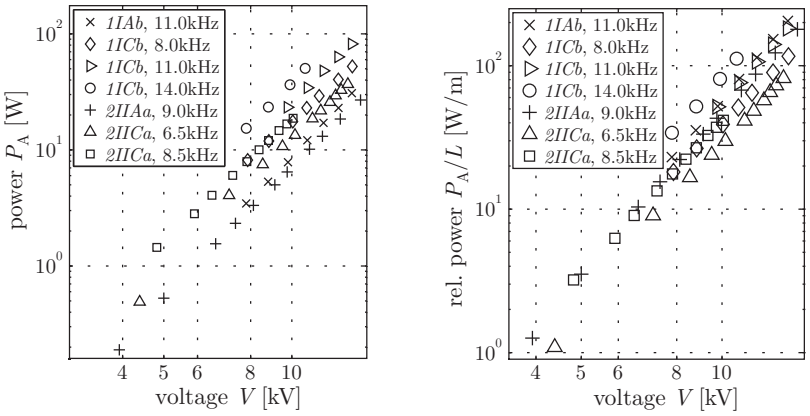

(a) absolute (b) relative

Figure 3.5: Consumed power P_A as function of actuator voltage V.

the operating frequency f this assumption consequently has to result in a constant consumed energy E_k per cycle k to satisfy equation (3.4). If this were true, the maximum slopes in the Lissajous figure would be independent of the operating frequency. For instance, Porter *et al.* [179] explicitly assume that the dissipated energy per cycle $E = P_A/f$ of the operating voltage is constant for fixed operating conditions, not dependent on the operating frequency. Consequently, the enclosed area of the corresponding Lissajous figures achieved at a constant operating voltage would have to be constant over the entire measured frequency range. This assumption, in fact, is an oversimplification as demonstrated exemplarily in Figure 3.6 (cp. crosses in Figure 3.4).

The experiments of the present studies show a non-constant value of the dissipated energy-per-cycle for different operating frequencies, as illustrated in Figure 3.6(a). Therefore, the Lissajous figures corresponding to different operating frequencies at the same operating voltages change their shape (enclosed area) and also change their maximum slopes, which can be clearly identified from Figure 3.6(b). The consequences of these slope changes with changing operating frequencies for the resonance behavior and the characteristic capacitances will be discussed in Sections 3.3 and 3.4 respectively. In contradiction to previous publications, the results of present work show an empirical $P_A = f(f)$ relation according to the power

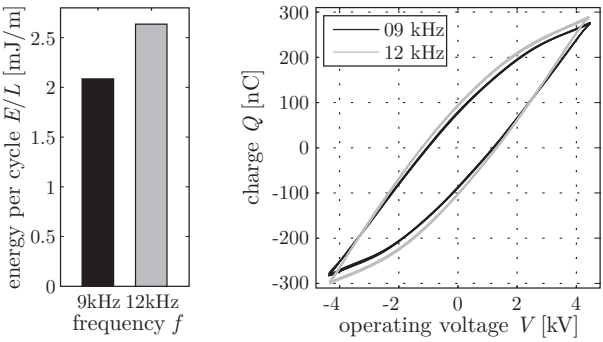

(a) enclosed area (b) Lissajous figures

Figure 3.6: Direct comparison of energy per cycle E for frequencies $f = 9$ kHz and $f = 12$ kHz at fixed operating voltage $V = 8.8$ kV; (a) enclosed area specifying E/L, (b) corresponding Lissajous figures.

of 3/2 instead of a linear relation, as sketched in Figure 3.7. Consequently, according to equation (3.4), the consumed energy E_k per cycle k is indeed affected by the plasma frequency with the power of 1/2.

3.2.3 Scaling Number Derivation

To advance one step further, with the objective of improving the predictability of results for varying operational conditions, the insights of Section 3.2.2 should be combined. Therefore, the two empirical approaches

$$P_A \propto V^{\frac{7}{2}} \tag{3.6}$$

$$P_A \propto f^{\frac{3}{2}} \tag{3.7}$$

yield in the joint functional description

$$P_A L^{-1} f^{-\frac{3}{2}} \propto V^{\frac{7}{2}} \qquad \text{and} \tag{3.8a}$$

$$\frac{P_A/L}{f^{\frac{3}{2}} V^{\frac{7}{2}}} = \Theta_A = \text{const.}\,, \tag{3.8b}$$

which moreover includes the length L of the actuator. A similar model was proposed by Roth *et al.* [193] in order to describe the power losses due

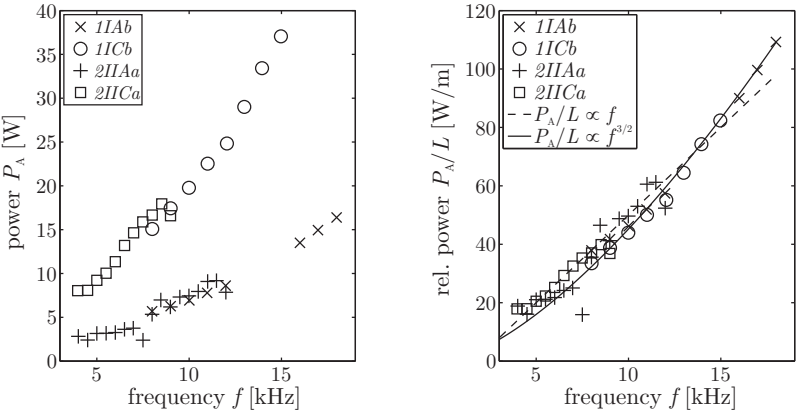

(a) absolute (b) relative

Figure 3.7: Consumed power P_A as function of frequency f ($V = 10$ kV).

to dielectric heating. They identified $V^2 f$ and P_{loss} to be convenient key quantities to comprehensively describe their phenomenon.

The results of equations (3.8) are plotted in Figure 3.8. It is obvious from Figure 3.8(a) that the former discrepancies between the results vanish and all curves collapse better, which demonstrates the robustness and the improved generality of equation (3.8a) as a scaling law for describing the electrical characteristics of DBD plasma actuators. Now only one single experiment is required to calculate Θ_A for a particular configuration of the dielectric material (see Figure 3.8(b)).

However, even though this new scaling law (3.8) seems promising to describe and classify the consumed electrical power of DBD plasma actuators for varying operating conditions, this model does not include any information about the resonance behavior of the electrical plasma-actuator setup or the electrical efficiency η_{E} of its operation.

3.3 Resonance Effects

Generally, any electrical plasma-actuator setup, i.e. high-voltage transformer including connected plasma actuator, has a particular resonance frequency f_{res}. An easy and convenient procedure to characterize this fre-

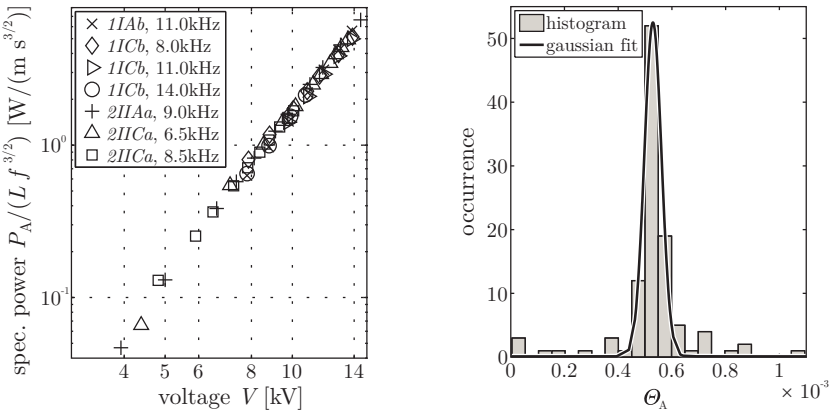

(a) $P_A L^{-1} f^{-\frac{3}{2}}$ according to (3.8a)

(b) Θ_A according to (3.8b)

Figure 3.8: Combined $P-V-f$ description for several operating conditions based on the scaling law (3.8).

quency is to apply a constant input voltage V_{input} to the high-voltage transformer and systematically vary the operating frequency f. The resulting slope of the high-voltage transformer's current drain I_{input} and corresponding input power

$$P_{\text{input}} = V_{\text{input}} I_{\text{input}} \tag{3.9}$$

are shown in Figure 3.9 exemplarily for two different actuator lengths[2]. Since the amplification level of the HV transformer is affected by the resonance effect as well, the resulting high voltage V changes with changing frequencies f at constant input voltages V_{input}. Consequently, the absolute values of the input power P_{input} in this particular investigation do not allow a performance quantification but rather a resonance characterization.

However, this example demonstrates that the size of the load influences the natural resonant frequency f_{res} of the setup. Exact knowledge about this frequency as well as about the parameters that affect its value is of particular importance for any DBD-based flow-control application:

[2]In order to not confuse the reader, it should be emphasized that the separately conducted resonance identification experiments have been conducted with Minipuls1 (cp. Table 3.1). This transformer has its range of resonance at considerably lower frequencies than the Minipuls2. The conclusions drawn from these separate experiments are entirely unaffected by this difference.

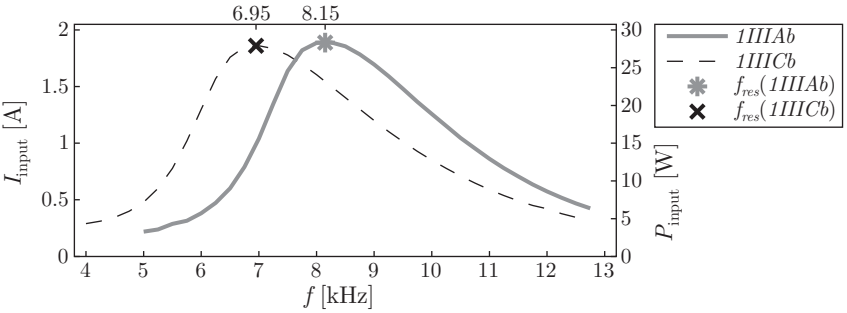

Figure 3.9: Current drain I_{input} and input power P_{input} for two different actuator lengths at constant input voltage $V_{\text{input}} = 15$ V.

The most salient reason to properly identify f_{res} arises from impedance-matching efforts, where the objective is optimization of the electrical plasma-actuator setup. Additionally, it is essential to understand the influence of all involved operation quantities on possible changes of f_{res}, since these quantities span the parameter space for active flow control by means of plasma actuators. Both issues will be discussed in Sections 3.3.1 and 3.3.2.

3.3.1 Resonance - Efficiency Relation

The extracted power-frequency relations, as discussed in Section 3.2.2, require further investigation concerning the composition of the discharge energy E, i.e. the interaction of the physical quantities processed with equation (3.5). For constant operating voltage V there are at least two remaining parameters that can modify the consumed power per cycle E_k determined by the enclosed area of the corresponding Lissajous figure (cp. Figure 3.3(b)): The amplitude of the transferred charge Q and the phase relation $\Delta\phi$ (obtained from $V = 0$ and $V_{\text{p}} = 0$) between abscissa V and ordinate Q.

The value of the transferred charge Q increases only slightly with increasing frequency, as indicated by Figure 3.6(b). In contrast to this the phase relation $\Delta\phi$ shows a steep rise at a specific frequency for every particular parameter combination, as depicted in Figure 3.10(a). This frequency has been identified to be the natural resonance frequency f_{res} of the experimental plasma actuator setup, i.e. the electric circuit comprising the

HV generator and the plasma actuator (see Figure 3.1). Hence, the resonance frequencies f_{res} for the different experiments are marked with dashed vertical lines in Figure 3.10.

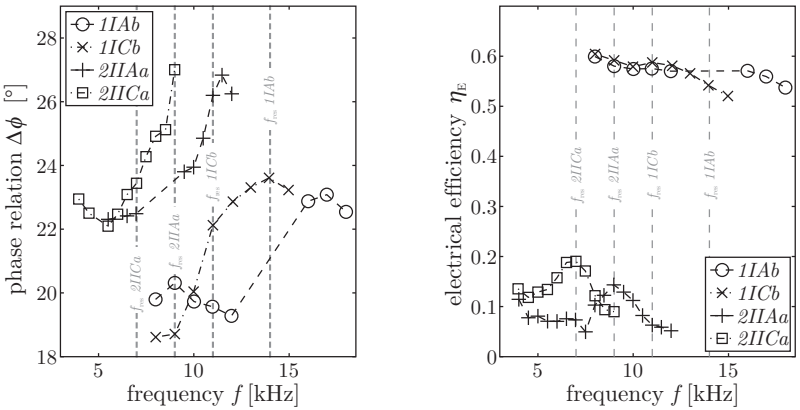

(a) phase relation $\Delta\phi$ (b) efficiency η_{E}

Figure 3.10: Phase relation $\Delta\phi$ between voltage V and charge Q (a) and electrical efficiency η_{E} according to definition (2.7) (b) for various frequencies f; vertical dashed lines indicate resonance frequencies for varying operational setups.

The corresponding curves of the electrical efficiency η_{E} according to definition (2.7) are shown in Figure 3.10(b). A local maximum in the range of the resonance frequency is observed, followed by an efficiency decrease for increasing frequencies[3]. In order to properly discuss this observation it is necessary to examine more carefully the characteristics of the Lissajous figures.

The impact of the phase relation $\Delta\phi$ between the operating voltage V and the transferred charge Q on the size of the enclosed area of the Lissajous figure can be easily demonstrated by means of the two example functions

[3]It should be noted that the HV generation by combining an audio amplifier and an automotive ignition coil is obviously ineffective, but all the more useful to cross-check the validity of the conclusions and their independence of a particular HV generator. The Minipuls series, on the other hand, is designed for a large frequency-range and therefore shows a much weaker resonance peak at a much higher global efficiency level.

$$\varphi_1(t) = sin(\omega t) \tag{3.10a}$$

$$\varphi_2(t) = sin(\omega t + \Delta\phi). \tag{3.10b}$$

The resulting Lissajous figures built using $\varphi_1(t)$ and $\varphi_2(t)$, and their enclosed area A calculated according to equation (3.3) are plotted in Figure 3.11 for phase relations ranging from $0 \leq \Delta\phi \leq 90°$. Furthermore, the phase-relation range as observed for the DBD experiments (see Figure 3.10(a)) is shown as a shaded gray area in Figure 3.11(b).

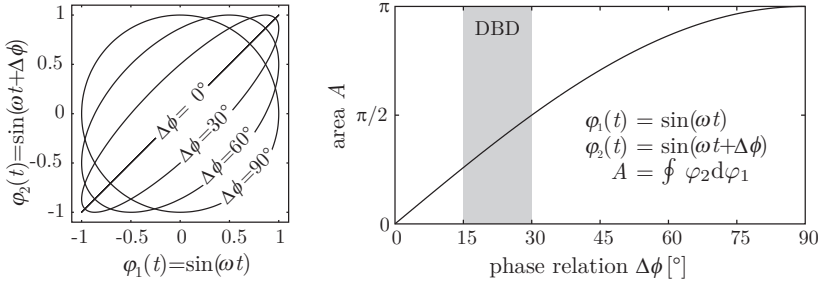

(a) cyclograms

(b) enclosed area

Figure 3.11: Lissajous figures (a) and calculated enclosed area (b) of equations (3.10) as function of phase relation $\Delta\phi$.

The almost linearly increasing value of A in the DBD-relevant range of phase leads to the conclusion that the sharp increase of the enclosed area of the cyclogram corresponds to the observed efficiency rise near the resonance frequency. In terms of power levels, an increase of phase results in either a higher consumed actuator power P_A for constant input power P_{input} or less required input power P_{input} for constant output quantities. Consequently, both cases lead to higher efficiency η_{E} according to definition (2.7), since either the numerator increases or the denominator decreases.

Crossing the resonance frequency f_{res} in Figure 3.10 results in an increasing phase relation $\Delta\phi$ and consequently in a locally increasing efficiency η_{E}. Thereafter, the efficiency continues its decaying trend due to the global decrease for increasing frequencies. Since the actuator power P_A rises with increasing frequencies (see Figure 3.7), which is a counteracting effect to the decreasing efficiency trend, the local efficiency maximum sightly above the resonance frequency should be the desired point of actuator operation.

3.3.2 Resonance - Discharge-Volume Relation

The resonance frequency of any particular AC-HV generator (among inner parameters like core heating of the transformers) mainly depends on the load connected to it. In the present context this load is the plasma actuator. Evidently, the value of this load is proportional to the length of the actuator, as exemplarily demonstrated in Figure 3.9 and confirmed in Figure 3.10 (crosses: short actuators, open symbols: long actuators). Additionally, it is severely affected by changes of operating conditions as well, which is a rather new but all the more important insight.

Coogan [42] reports a remarkable reduction of an excimer lamp's resonance frequency right after its first ignition. This ignition, according to Coogan, entails an increase of the lamp capacitance, which shifts the resonance to lower frequencies. According to Raizer *et al.* [183], the load characteristics change on discharge excitation, due to a considerable increase in capacitance and active conductivity of a gas gap after a plasma has been produced.

Furthermore, Yang *et al.* [237] investigated the influence of operating-parameter changes on the resonance curve of their discharge device. They identified a reduction of the resonance frequency for both increasing size of the load and increasing operating voltages. To gain deeper insight into the influence of plasma-actuator length L and operating conditions on the resonance frequency f_{res} of the DBD circuit, both parameters have to be investigated systematically. Based on these reports it must be concluded that the presence of plasma [42] and its spatial extent [237] considerably contribute to the effective size of the load. This transfer of the insights reported by Coogan [42] and Yang *et al.* [237] provides additional valuable potential for optimization of the electrical plasma-actuator setups.

The decrease of the resonance frequency with increasing voltage due to the increasing volume of the discharge is demonstrated in Figure 3.12 for different actuators. Two important conclusions can be drawn from Figure 3.12 knowing that f_{res} varies with changing operating voltages.

First, for a constant operating frequency f, which has initially been aligned with f_{res}, this effect results in a decreasing efficiency η_E (see Figure 3.10(b)). On the one hand, for an increasing operating voltage the resonance frequency decreases and consequently the operating frequency departs to the right from the local efficiency maximum due to the global decrease effects. On the other hand, by lowering the operating voltage the resonance frequency increases, which causes a phase-relation drop for constant operating frequency and consequently also results in a lower efficiency η_{E}.

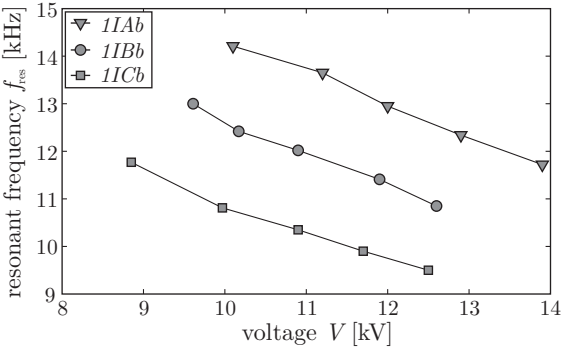

Figure 3.12: Natural resonance frequency f_{res} as a function of actuator voltage V.

Second, it can be concluded from Figure 3.12 that the impedance of any electrical plasma-actuator setup, among other parameters, is significantly affected by the chosen operating voltage. For instance, for constant operating frequency, one moves across the resonance frequency by simply changing the operating voltage as demonstrated in Figure 3.13. This effect not only influences the electrical efficiency η_{E}. When the operating frequency of the plasma actuator itself is a control variable of the setup, crossing the resonance frequency inevitably leads to a sign change of the resulting characteristic control behavior of the control device. This changeover is sketched in Figure 3.13 as well, where the labels A, B and C denote the control behavior above, at and below the resonance frequency f_{res} respectively.

Obviously, the plasma actuator is not only a passive component but consists of a pure passive component part and a discharge dependent part. The passive component part mainly depends on the actuator construction (dimensions, materials), whereas the discharge dependent changes with intensity and spatial extent of the plasma on the dielectric layer. Consequently, it is necessary to understand the effect of a changing discharge intensity and its corresponding capacitance to the overall load of the electrical plasma-actuator setup. This knowledge is of particular importance for any successful impedance matching and advanced design of control algorithms for discharge based flow control.

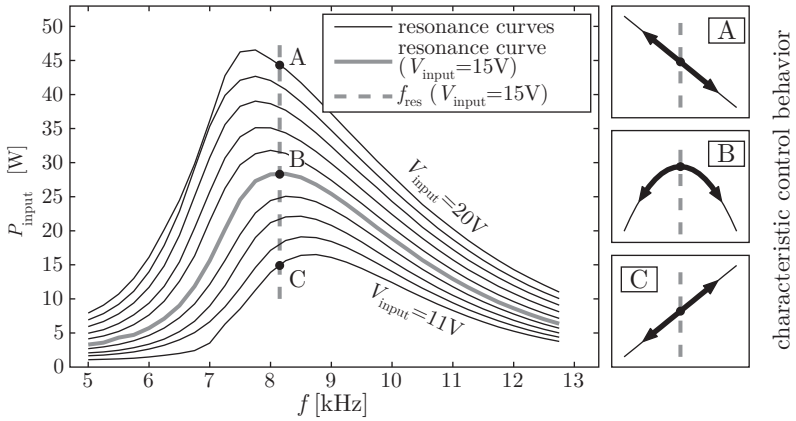

Figure 3.13: Resonance curves of an operative electrical plasma-actuator setup (*1IIIAb*) for various input voltages and respective control characteristics for frequency variations.

3.4 Characteristic Capacitances

In 2002 Chen [38] identified that impedance-matching of the electrical circuit of a plasma-actuator system is a powerful means for optimizing plasma actuator setups. Subsequently, several studies concerning this topic have been undertaken, as reported e.g. by Opaits *et al.* [161, 162], Chen [39], Singh and Roy [203]) or Zito *et al.* [238]. However, from Section 3.3 and especially from Figures 3.12 and 3.13 we see that changes of the operating voltage and corresponding variations of the electrical power consumption strongly influence the resonance behavior of the electrical circuit. This insight is of utmost importance for impedance matching, since any perfectly matched electrical circuit immediately becomes de-tuned with changes of the power level. The impedance of a plasma-actuator setup under operation is highly unsteady and depending on many parameters. Therefore, it is desirable to determine the capacitance of plasma actuators and furthermore to quantify the impact of the operating conditions (operating voltage and frequency) on the resulting plasma-actuator capacitance.

3.4.1 Capacitance Determination

Based on Manley's equations [149] it is possible to derive several capacitances involved in the discharge process. For volume discharge (VD) this has been described e.g. by Falkenstein and Coogan [70] or by Wagner *et al.* [229]. However, a deeper insight into the discharge of both VD and SD can be derived from Lissajous figures by calculating

$$C(t) = \frac{\mathrm{d}Q(t)}{\mathrm{d}V(t)}, \tag{3.11}$$

since the slope of the Q-V cyclogram corresponds to the capacitance $C(t)$ of the actuator at specific phase angles $\phi(t)$ of the operating AC voltage $V(t)$ (see e.g. [87, 229]). For VD the capacitance C can easily be calculated as a serial combination of C_g (gas) and C_d (dielectric)

$$\frac{1}{C} = \frac{1}{C_g} + \frac{1}{C_d} \tag{3.12a}$$

$$\Leftrightarrow \quad C = \frac{C_g C_d}{C_g + C_d}. \tag{3.12b}$$

The former equation (3.12a) was introduced by Manley [149], the latter one (3.12b) was used in [145, 229]. Furthermore, Manley [149] mentioned for VD that the sharpness of the corners of the Lissajous figures denote the abrupt stop of the discharge at the operating voltage maximum (see Figure 3.3). This phenomenological study can be transferred to surface discharge as well, since it is in very good agreement with the present observations, where a sudden discharge current drop can be identified in combined voltage/current plots at the locations of the operating voltage maxima (see e.g. [2, 68, 79, 177]).

Unfortunately, the pure serial description of equation (3.12) is invalid for surface DBD actuators, since their discharge occurs in a stepwise growth [87] of the plasma channels, as described by Gibalov and Pietsch [87]. Enloe *et al.* [68], for instance, demonstrated the effect of transient chordwise growth of the plasma extent of DBD plasma actuators by means of a photomultiplier tube. Nersisyan and Graham [159] modified the pure serial description of equation (3.12) with an additional resistance R_g in parallel to C_g to consider the plasma's conductivity - still for VD purposes. Nevertheless, this model seems to be useful for a SD description as well, as introduced by Van Dyken *et al.* [221] and Enloe *et al.* [68, 69] almost at the same time (2004), later by Pons *et al.* [175]. However, based on the model

of Nersisyan and Graham, other modified plasma actuator model descriptions, which are rooted in capacitance assumptions, have been introduced e.g. by Singh and Roy [203] ($C_p - L_p - R_p - C_d$). An even more complex model has been suggested by Orlov *et al.* [164, 166, 167] and subsequently applied e.g. by Lemire *et al.* [136]. This so-called lumped-element circuit model already includes estimations about the spatial-temporal growth of the plasma. According to Orlov *et al.* [167], this model was calibrated based on the experimentally obtained luminosity data of Enloe *et al.* [67].

The effect of a decreasing resonance frequency with increasing power levels occurs, since the chordwise plasma length and therefore the discharge zone increases, as discussed in Section 3.3. This effective electrode-size enlargement is denoted the virtual electrode length by Enloe *et al.* [68] or the plasma extent by Orlov *et al.* [165]. However, in terms of impedance matching, any changes of the virtual size of the electrode (i.e. plasma extent) can be directly interpreted as a power forced change of the load of the electrical LC-circuit, as denoted by Huang *et al.* [105]. The (adverse) effect of a (mis-)matched DBD system is emphasized e.g. by Singh and Roy [203] in terms of expensively over-rated power supplies. Therefore, a quantitative determination of the effective plasma-actuator capacitance as a function of the operating parameters, as previously discussed in Sections 3.2 and 3.3, is necessary, in order to meet the requirements of an advanced impedance-matching purpose.

3.4.2 Capacitance-Quantification Strategy

Regardless of the chosen DBD setup (VD or SD), equation (3.11) yields the temporal evolution of the capacitance of the plasma actuator, which has been implemented by means of forward differences according to

$$C(t_i) = \left.\frac{\Delta Q}{\Delta V}\right|_{t_i} = \frac{Q(t_{i+1}) - Q(t_i)}{V(t_{i+1}) - V(t_i)}. \tag{3.13}$$

Due to the parallelogram shaped cyclogram of the VD of Figure 3.3(a), the capacitance of the volume discharge $C_{\mathrm{VD}}(t)$ has a square-wave shape. The more complex case of surface discharge (SD) is shown in Figure 3.14[4], where the time trace of the operating voltage is additionally included for orientation purposes. A corresponding Lissajous figure of similar data has already been depicted in Figure 3.3(b).

[4] The vertical peaks occur periodically at $\pm V_{\max}$, since the denominator of the expression $\mathrm{d}Q/\mathrm{d}V = C$ periodically changes its sign while ranging around zero.

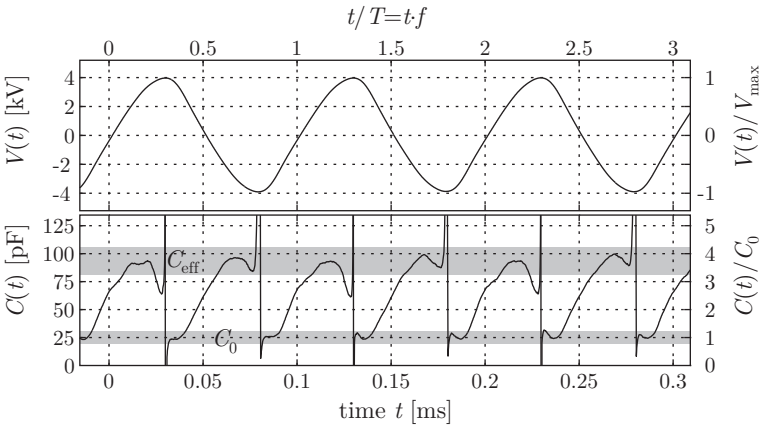

Figure 3.14: Voltage and capacitance time traces of a DBD plasma actuator according to equation (3.11).

The lower gray shaded plateaus of Figure 3.14 correspond to the so-called dark periods (Manley [149]) where no discharge occurs. These dark periods can be identified in luminosity diagrams of the discharge as well, as shown for instance by Enloe *et al.* [68, 69] for the temporal light emission and the spatial-temporal luminosity distribution. The values of these plateaus quantify the electrical pure passive component (cold) capacitance of the plasma actuator, which will be referred to as C_0 in the following. It is important to note that C_0 can be alternatively measured across a disconnected and non-operative plasma actuator using a conventional multimeter, and the result agrees with the method described here.

The upper gray shaded plateaus correspond to the effective capacitance C_{eff}, consisting of a combination of the passive-component C_0 and the contribution of the plasma itself to the capacitance. The ratio $C(t)/C_0$ is given by the right ordinate of Figure 3.14, where the time dependent capacitance of the plasma increases the total capacitance of a plasma actuator during operation by a factor four as compared to the cold capacitance. The initial value of each half-cycle is C_0 at the dark period and increases towards C_{eff} as the plasma domain grows. As V reaches its peak value, the discharge collapses, and the capacitance falls back to C_0. Since C_{eff} comprises the real electrode and the above-mentioned virtual electrode-size enlargement, C_{eff} provides a quantity for defining the virtual capacitance of the operative

plasma actuator. Based on this characterization, it is therefore possible to quantify the magnitude of the load connected to the HV power supply and consequently the load-resonance behavior of the entire system for varying operational settings.

3.4.3 Capacitance-Histogram Analysis

The extraction of robust numerical values from the gray-shaded capacitance ranges in Figure 3.14 is a challenging task. However, a good estimation of C_0 and C_{eff} can be obtained by determining the local maxima in the capacitance-histogram, as demonstrated in Figure 3.15 for the example given in Figure 3.14. The influence of varying operating voltages and frequencies on the resulting histograms, both resulting in varying power-levels, are shown in Figure 3.16.

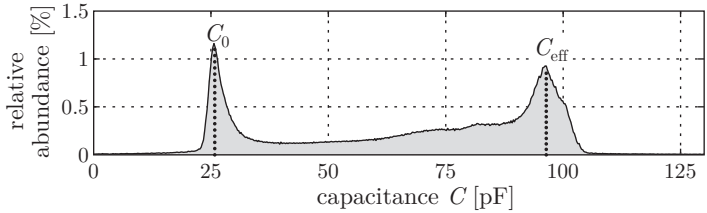

Figure 3.15: Capacitance histogram with characteristic peaks for C_0 and C_{eff} (cp. Figure 3.11).

Such capacitance histograms yield insight into several phenomena: A comparison of the histograms of Figure 3.16 demonstrates the independence of the lower peak C_0 from the discharge. This result confirms the assumption of a pure passive-component character of C_0. Consequently, it can be concluded that the value of C_0 represents the constant cold capacitance of the plasma actuator. Secondly, a linear growth of the effective capacitance C_{eff} can be seen for both increasing operating voltages (Figure 3.16(a)) and increasing frequencies (Figure 3.16(b)), where the impact of the operating voltage is larger than that of the frequency. This obviously occurs due to the increasing power levels with either of the parameters ($P_A \propto V^{\frac{7}{2}}$, $P_A \propto f^{\frac{3}{2}}$), as discussed in Section 3.2.2. The weak impact of the frequency comes as no surprise, since combined analysis of equations (3.4) and (3.7) leads to $E \propto f^{\frac{1}{2}}$. This results in an even weaker influence of

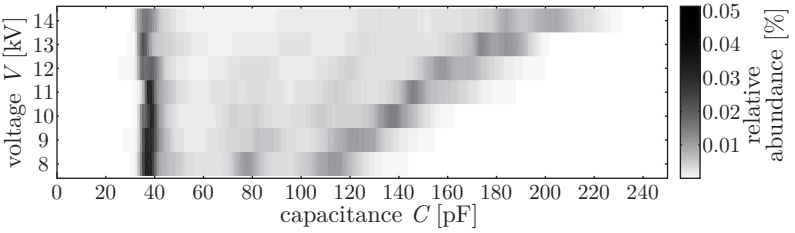

(a) voltage (*1ICb*, 8 kHz)

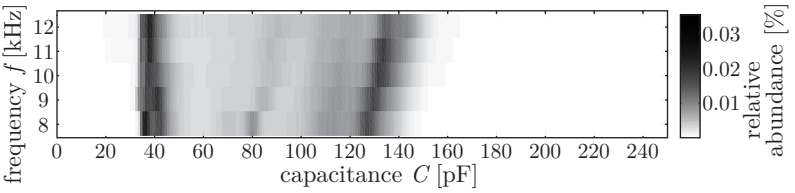

(b) frequency (*1ICb*, 10 kV)

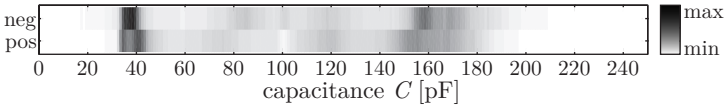

(c) half-cycle (*1ICb*, 12 kV, 8 kHz)

Figure 3.16: Capacitance histogram: Relative occurrence of capacitance values derived from (3.11) for varying operating voltages (a), frequencies (b) and for both half-cycles (c).

the frequency on the slope of the corresponding cyclogram for a constant operating voltage V and cold capacitance C_0 (cp. Section 3.3).

Furthermore, the light gray color in the range between the two peaks corresponds to the transient growth of $C(t)$ for the growing plasma length from C_0 to C_{eff} of a surface DBD within every discharge-cycle. This growth can be recognized from the Lissajous figures as well (cp. Figure 3.3(b)), since the counter-clockwise orientated time trace of this cyclogram and its periodically increasing slopes already suggest the observed transient growth.

The involved mechanisms of the two half-cycles vary and result in two

different discharges, as demonstrated e.g. by Gibalov and Pietsch [87], Enloe *et al.* [61, 64] and Leonov *et al.* [137]. Consequently, it is important to cross-check the resulting effective capacitance values for positive and negative half-cycles C_{eff}^{+} and C_{eff}^{-} respectively (see Figure 3.3(b)). An example of such a distinction of half-cycles is given in Figure 3.16(c). All above-mentioned effects qualitatively look alike for the two half-cycles, even though the peak values and widths differ slightly. This small difference occurs due to the fact that the discharge of the positive half-cycle occurs in the streamer mode, which is much noisier compared to the glow-type discharge that characterizes the negative half-cycle, as described by Orlov *et al.* [168]. The different noise levels can also be identified from current plots $I(t)$, as published e.g. in [32, 79, 148, 172, 178]. Nevertheless, the impact of the discharge type to the resulting effective capacitance is of minor importance, since the peak values for the effective capacitance only differ slightly ($C_{\text{eff}}^{+}/C_{\text{eff}}^{-} \approx 1$).

The peak values of C_0 and C_{eff}, extracted from the histograms, as demonstrated in Figure 3.16, are plotted in Figure 3.17 for the same operational settings as previously discussed in Section 3.2.2 and plotted in Figures 3.5 and 3.7. The results of all configurations consist of two branches. The lower branches highlight the constant pure passive component character of the plasma-actuator's cold capacitance C_0 during the above-mentioned dark periods. The upper branches of Figure 3.17 quantitatively characterize the non-constant effective capacitance C_{eff} during the discharge as a function of the operating voltage (Figure 3.17(a)) and frequency (Figure 3.17(b)). Therefore, both capacitances (C_0 and C_{eff}) should be taken into account for the chosen experimental setup, if advanced impedance matching is desired. Similar diagrams have been published by Francke *et al.* [81] and Tu *et al.* [218] for volume-discharge devices, where the steeper slopes of the parallelograms (cp. Figure 3.3(a)) show an increasing steepness for increasing amount of plasma until the gas gap is fully bridged.

However, for the plasma-actuator surface discharge it can also be recognized from Figure 3.17 that the actuator length L influences the upper branches slightly, since the slopes for the short actuators (crosses) are slightly above those for the long actuators (open symbols). This effect can be explained by the occurrence of 3D effects at the ends of the actuator, which results in an enlarged total discharge area compared to the length of the electrode. With increasing actuator-length this edge effect vanishes and a more ideal 2D situation is realized.

For the plasma actuator materials and dimensions chosen for the present

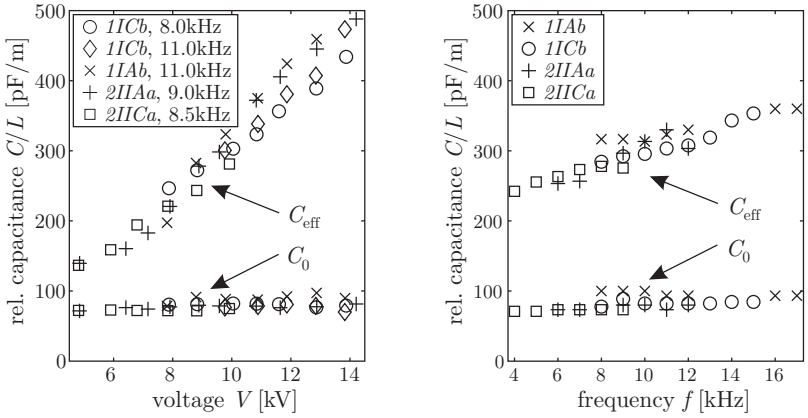

(a) voltage (b) frequency

Figure 3.17: Plasma actuator capacitances C_0 and C_{eff} for varying operational configurations (cp. Figures 3.5 and 3.7).

study, the branches of length-related passive component capacitance C_0/L collapse at a constant value of ≈ 80 pF/m over the entire range of investigated operating conditions. In contradiction to this, the length-related effective capacitance C_{eff}/L more than doubles its value from ≈ 200 pF/m at 7 kV to ≈ 450 pF/m at 14 kV, which is more than five times the cold capacitance value C_0/L (see Figure 3.17(a)). Obviously, for elevated operating power levels C_{eff} can easily exceed C_0 by one order of magnitude.

Taking into account this significant difference, the necessity of carefully matching the electrical setups for individual applications has to be emphasized, which additionally requires knowledge of the operating conditions. The resonance frequency of a plasma-actuator system does not only depend on the actuator length but also considerably on the operating power level. This is of particular importance, if the chosen operating frequency is close to the resonance frequency of the entire system, as emphasized in Section 3.3.

3.4.4 Independency-Check of the Probe Capacitor

The choice of the optimal probe capacitor C_{p} is influenced by the following aspects: The signal-to-noise level of the recorded probe signal decreases

with increasing C_p, since the probe signal itself decreases ($C_\mathrm{p} \propto 1/V_\mathrm{p}$). The presence of the probe capacitor cannot be neglected for small probe capacitances, since it is connected in series with the actuator,

$$\overbrace{\frac{1}{C_\mathrm{t}}}^{\text{total}} = \overbrace{\frac{1}{C_\mathrm{a}}}^{\text{actuator}} + \underbrace{\overbrace{\frac{1}{C_\mathrm{p}}}^{\text{probe}}}_{\substack{\text{negligible for} \\ C_\mathrm{p} \gg C_\mathrm{eff} > C_0}}, \tag{3.14}$$

where (3.14) appears according to (3.12a). The present results were obtained with a probe capacitance of $C_\mathrm{p} = 22$ nF, which is three orders higher than the actuator capacitance C_0 and two orders higher than the effective capacitance of the discharge C_eff. Furthermore, the assumption $C_\mathrm{p} = 22\ \mathrm{nF} \gg C_\mathrm{eff} > C_0$ is verified by comparing the results obtained with different capacitors, as demonstrated in Figures 3.18 and 3.19.

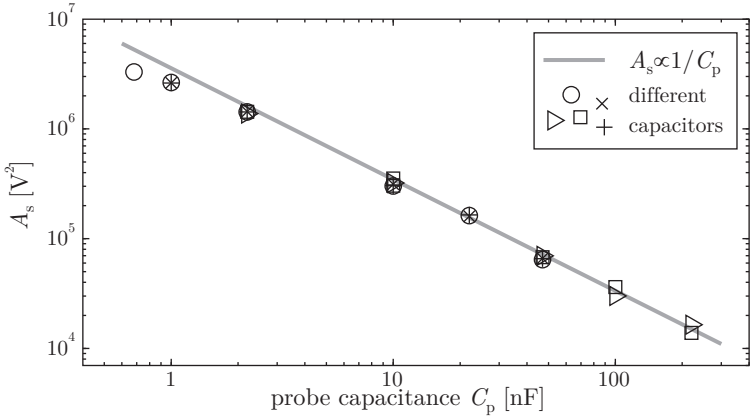

Figure 3.18: Area enclosed by the cyclogram spanned by the probe signals V and V_p according to (3.15).

Several capacitances ($C_\mathrm{p} = 0.68 \ldots 220$ nF) and varying capacitor types (different symbols) were chosen to measure one and the same operating condition of a plasma actuator ($L = 0.45$ m, $f = 8$ kHz, $V = 10$ kV). The

enclosed area determined according to

$$A_\mathrm{s} = \frac{1}{K}\sum_{k=1}^{K}\oint_k V_\mathrm{p}(t)\mathrm{d}V \tag{3.15}$$

from the recorded probe signals V and V_p according to (3.5) is shown in Figure 3.18 for all measured capacitors. Should the chosen probe capacitance does not influence the electrical circuit of the plasma-actuator setup, the resulting calculations, according to (3.15) have to collapse with the $A_\mathrm{s} \propto 1/C_\mathrm{p}$ slope (cp. (3.2)), as also sketched in this diagram. It can be seen that the values are below this line for small probe capacitances and asymptotically align with the $A_\mathrm{s} \propto 1/C_\mathrm{p}$ slope for larger values of C_p.

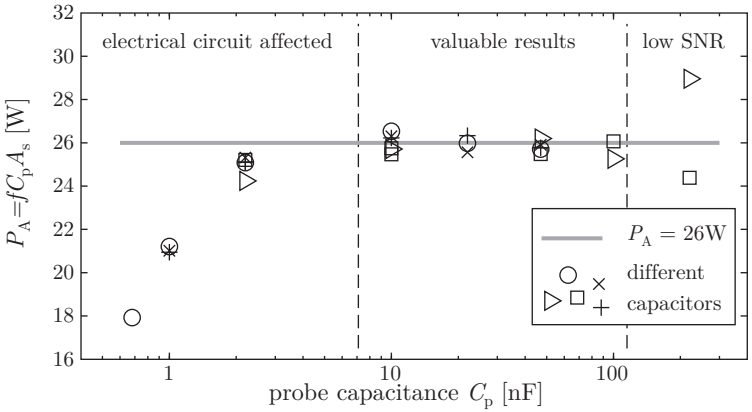

Figure 3.19: Independency check of the chosen probe capacitance C_p on the calculated power consumption P_A according to (3.5).

The results of the power consumption calculations according to (3.5) are shown in Figure 3.19, where the iso-power line (P_A = 26 W) in the diagram corresponds to the $A_\mathrm{s} \propto 1/C_\mathrm{p}$ slope of Figure 3.18. The adverse effect of an underdimensioned probe capacitance on the resulting P_A is clearly demonstrated. Obviously, in the present case of C_0 = 37 pF, the electrical circuit has been considerably affected by probe capacitances of $C_\mathrm{p} < 10$ nF. Furthermore, the poor accuracy of the measured data due to

the aforementioned weak signal-to-noise ratio (SNR) for overdimensioned probe capacitances can be identified in Figure 3.19.

This independency study elucidates the necessity of thoroughly specifying the capacitance C_p of the probe capacitor for accurately measuring the power consumption P_A of plasma-actuators. Evidently, a proper choice of C_p is essential for high quality power consumption measurements of an electrical plasma-actuator setup, since the probe itself might distort the correctness of the obtained data. It is therefore strongly recommended that preliminary investigations to identify an appropriate C_p should be the first step for any electrical performance quantification effort for evaluating plasma-actuator systems.

4 Light Emission Analysis

The sensitivity of the entire electrical plasma-actuator setup with respect to the distribution of the discharge volume has already been indicated in Chapter 3. The close relationship between the electrical power consumed by plasma actuators and the light emission of their discharge is described e.g. by Enloe *et al.* [68, 69]. Based on these correlations, a cause-effect-relation between emitted light and the resulting flow characteristics has already been demonstrated by Kriegseis *et al.* [123].

To gain deeper insight into the electro-optical characteristics of plasma actuators, luminosity investigations of the discharge are introduced in this chapter. The experimental procedure and (post-) processing strategies to extract quantifiable measures are described in Section 4.1. Subsequently, the achieved results and derived insights are discussed in Section 4.2 to confirm the interrelation between effective capacitance of a plasma actuator and the discharge distribution over the dielectric surface.

4.1 Discharge Distribution Measurements

Figure 4.1 shows an example photograph of the discharge of DBD plasma-actuators in air, where the typical lilac color arises from the characteristic colors of the species involved (cp. Brown [34]).

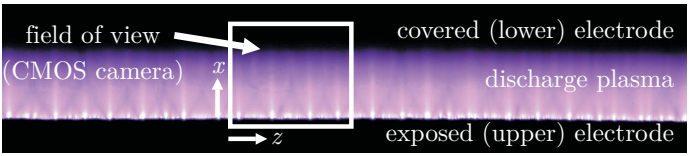

Figure 4.1: Picture of an operating DBD plasma actuator indicating the coordinate system and measurement domain of the light emission analysis.

Pavon *et al.* [172] demonstrated that the light emission of the species i involved in the plasma-actuator discharge is uniformly distributed over the

species-dependent wavelengths λ^i_{DBD}. Therefore, the measurement techniques for recording the emitted light do not necessarily have to resolve information according to wavelength. Consequently, photomultiplier tubes or high-resolution cameras can be used to obtain results with high temporal and/or spatial resolution, without the need to detect special wavelengths. The latter technique is used here, as illustrated in Figure 4.1, where additionally the coordinate system and measurement domain of the light emission analysis are highlighted.

The experimental setup is sketched in Figure 4.2. An overhead mounted CMOS camera (Phantom V12.1, 1280×800 pixels, 24 fps; Nikon 105 mm, AF Micro NIKKOR f/2.8D) was used to record the time-averaged light emission of the discharge during the investigation of the electrical operation parameters (see also Figure 4.1). The electrical measurements were obtained as described in Section 3.1. Since no actuator length related dependencies were to be expected from the light emission experiments, only the longest actuator ($L = 0.45$ m, *1ICb*, cp. Table 3.1) was used for the measurements.

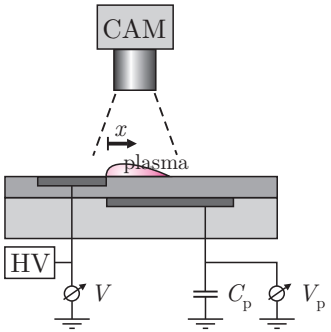

Figure 4.2: Experimental setup for the light emission analysis comprising an overhead camera (CAM) and the electrical setup as introduced in Section 3.1.

The chosen exposure time of $\Delta t = 40$ms for the experiments is two orders of magnitude longer than the discharge period. Therefore, each raw image $j \in J$ corresponds to a time integration of the spatio-temporal luminosity distribution $L(x, z, t)$. Averaging the $J = 100$ images yields the spatial

gray-value distribution

$$\bar{g}(x,z) = \frac{1}{J}\sum_{j=1}^{J} g_j(x,z), \quad \text{where} \tag{4.1a}$$

$$g_j(x,z) \mathrel{\widehat{=}} \int_{\Delta t_j} L(x,z,t)\mathrm{d}t. \tag{4.1b}$$

The discharge structure is optically characterized by Enloe *et al.* [63] and Orlov *et al.* [168] for the two half cycles of the AC cycle (cp. Leonov *et al.* [137]). They distinguish a (diffuse) glow- or Townsend-type discharge for the negative half cycle and a (highly filamentary) streamer type discharge for the positive half cycle. Such a distinction can alternatively be performed based on discharge-current time traces, as reported e.g. by Pons *et al.* [175] and Forte *et al.* [78, 79]. However, it has already been demonstrated in Section 3.4 that this distinction does not affect the large-scale properties of the discharge, i.e. the effective capacitance C_{eff}. The comparison of the standard deviations $\sigma_{\bar{g}}$ of the J light emission distributions and σ_{P_A} of the power consumption, which are both below 5%, furthermore assures that (4.1a) is a convenient and valid simplification of the discharge with respect to its temporal evolution.

According to Becker *et al.* [18], the governing parameters that promote/suppress filamentation of discharges at atmospheric conditions are not yet completely understood. Gherardi *et al.* [85, 86] and Choi *et al.* [40] investigated the transition from glow to streamer discharge at atmospheric conditions for nitrogen and air respectively. The results of such studies are of great importance, since most plasma-actuator flow-control applications operate at ambient conditions, i.e. within the range of the discharge transition. Enloe *et al.* [65] reported a strong effect of oxygen presence on the force production, but only minor effects on the plasma structure itself. Therefore, the filamentary structure of the discharge has to be taken into account and to be discussed for the light emission analysis.

The spanwise averaged light intensity $G(x)$ and corresponding standard deviation σ_G are estimated according to

$$G(x) = \frac{1}{N_z}\sum_{i=1}^{N_z} \bar{g}(x,z_i) \tag{4.2}$$

and

$$\sigma_G = \sqrt{\frac{1}{N_z - 1} \sum_{i=1}^{N_z} \left[\bar{g}(x, z_i) - G(x) \right]^2}. \tag{4.3}$$

The resulting gray value distributions $G(x)$ are shown in Figure 4.3(a) for several power levels. For the most filamentary case at $V = 12.3$ kV gray values $G(x)$ and corresponding standard deviations σ_G are shown in Figure 4.3(b).

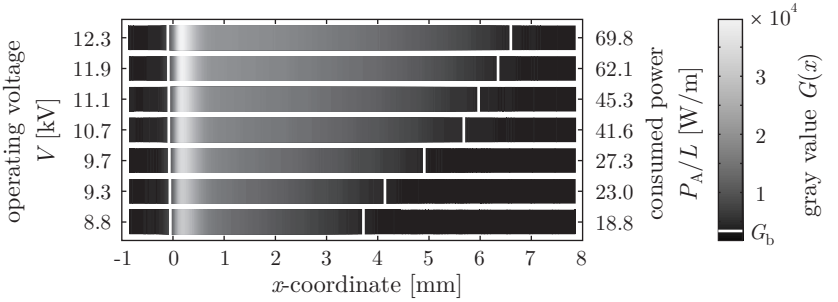

(a) gray value distribution

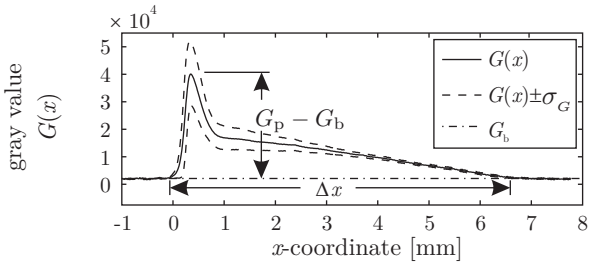

(b) characteristic quantities

Figure 4.3: Gray-value distribution $G(x)$ along the chordwise coordinate x (cp. Figure 4.2); (a) for several operating voltages V and power levels P_A; (b) at $V = 12.3$ kV with corresponding standard deviation σ_G and sketch of quantities Δx and $G_\mathrm{p} - G_\mathrm{b}$.

This diagram additionally contains information on the relative peak in-

tensity

$$\widehat{G} = \frac{G_\mathrm{p} - G_\mathrm{b}}{G_\mathrm{b}} \tag{4.4}$$

and the chordwise plasma (illumination) length

$$\Delta x = x_\mathrm{max}(G(x) > G_\mathrm{b}) - x_\mathrm{min}(G > G_\mathrm{b}). \tag{4.5}$$

G_b and G_p are the gray values of both background and light emission peak. For the sake of completeness it should be noted that in the literature Δx is usually referred to as either plasma length [8, 49, 127, 214] or plasma extent [20, 176, 225].

It is important not to confuse the high standard deviation σ_G of the gray values with a high uncertainty or error. Rather, it concerns the number of filaments that occur along the spanwise coordinate z for the streamer mode [40, 65, 85, 86], which can be recognized in Figure 4.1. Regardless of its origin, σ_G can be neglected at chordwise locations, which are relevant for Δx estimation, as demonstrated in Figure 4.3(b).

4.2 Interrelation of Plasma Length and Effective Capacitance

The resulting plasma lengths Δx according to (4.5) are displayed as a function of the operating voltage V in Figure 4.4(a). Additionally, the effective capacitance C_eff/L during the discharge is also provided in Figure 4.4(b) to allow a direct qualitative comparison between both quantities. At first glance, a seemingly similar increase of both, the plasma length and the capacitance, can be identified for increasing operating voltage V. Furthermore, in accordance with the insights concerning the power consumption P_A as already discussed in Section 3.2 (cp. Figure 3.4), both quantities increase with increasing frequency f.

In order to demonstrate this direct interrelation (cp. Chapter 3), the effective capacitance C_eff is plotted against the plasma length Δx in Figure 4.5. The curves of all measured frequencies $8 \leq f \leq 13$ kHz collapse in this diagram. This demonstrates the close correlation between Δx and C_eff, which is independent of other operating parameters such as V and/or f. Apparently, the plasma domain appears as a virtual enlargement of the exposed electrode, where the chordwise plasma length Δx scales with the effective capacitance C_eff of the plasma actuator and consequently defines the effective size of the load in the electric circuit.

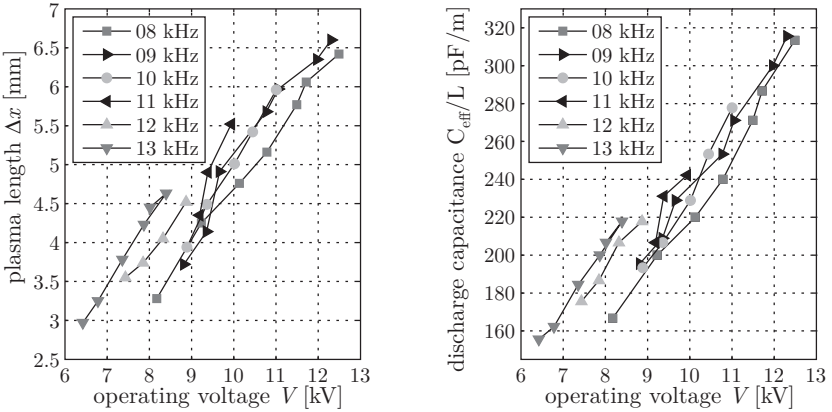

(a) plasma length Δx

(b) capacitance C_{eff}

Figure 4.4: Plasma length Δx (a) and effective plasma-actuator capacitance C_{eff} (b) as a function of operating voltage V for several frequencies f.

Therefore, the determination of the chordwise extension of the plasma along the dielectric layer by means of light emission analysis is a promising measure for plasma actuator performance quantification. Provided that the sensitivity of the camera is high enough, this value can be measured without any calibration, which makes the application of such light emission diagnostics an appropriate and simple procedure. Looking at the Figures 4.4(a), 4.4(b), and 4.5 it appears that robust empirical relationships of the form $C_{\text{eff}} \propto \Delta x \propto V$ can be derived, where the operating voltage V additionally requires information about the plasma frequency f for an unambiguous definition of the actuator-performance level.

Despite the occurrence of streamers and the corresponding high standard deviation σ_G in the exposed electrode's immediate vicinity, the non-dimensional peak intensity $\widehat{G}$ reveals useful information about the discharge intensity. Although careful calibration would be necessary in order to achieve quantitatively comparable results for different experiments, the linearly increasing relation of operating voltage V and peak intensity $\widehat{G}$ is a convenient measure to verify the respective electric measurements, as demonstrated in Figure 4.6.

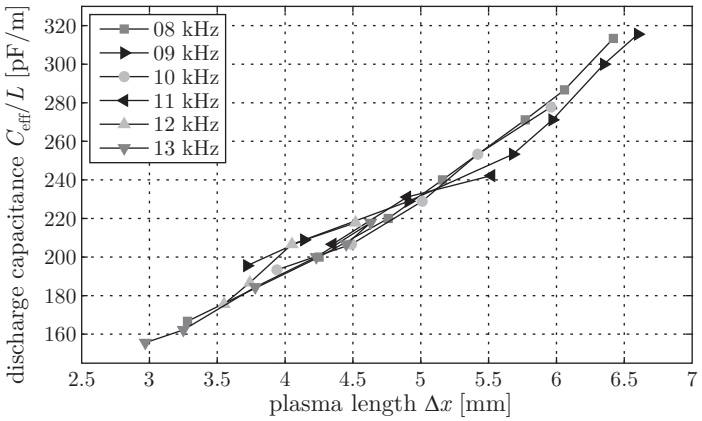

Figure 4.5: Effective actuator capacitance C_{eff} as a function of plasma length Δx for several frequency f.

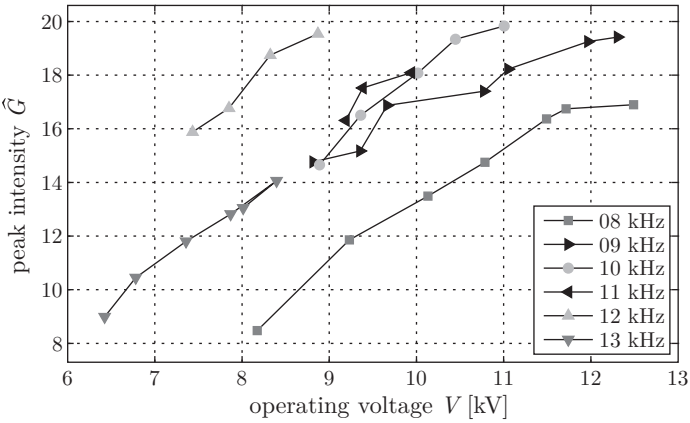

Figure 4.6: Non-dimensional relative peak intensity $\widehat{G}$ as a function of operating voltage V for several frequencies f.

Concluding, the electrical and optical measurement approaches as discussed in Chapters 3 and 4 respectively, represent independent but consistent measures to characterize and quantify the discharge performance of plasma actuators. Based on these discharge specific quantities the application of plasma actuators as flow-control devices will be discussed extensively in Chapters 5 - 7.

5 Momentum Transfer to the Air I: Fluid Mechanic Fundamentals and Explicit Measurements

The main characteristic of plasma-actuator applications as flow-control devices is the common objective to favorably manipulate the properties of an existing airflow by means of momentum transfer from the charged ions to the surrounding air. As mentioned in Chapter 2.1, this momentum transfer is typically termed plasma-actuator body force or volume force. Despite the general knowledge about the momentum transfer characteristic, the magnitude, spatial distribution and temporal evolution of this force cannot easily be predicted, either from first principles or using calibration models.

The next two Chapters 5 and 6 focus on the experimental determination of the plasma-actuator force and a comparison of the pure electrical quantities with the fluid mechanic results. Several experimental approaches have been published for a time-averaged [2, 71, 216] and time-resolved [62, 178] explicit estimation of the plasma-actuator force. Besides these explicit force estimation strategies, it is possible to calculate the force indirectly from velocity measurements. The latter will be referred to as implicit strategies, which can be further divided into integral and differential methods. Integral methods calculate a net value for the actuator force, based on the momentum balance equation. Deeper insight into the spatial distribution of the induced force is provided by differential methods, which are based either on the Navier-Stokes equations [234] or on the vorticity equation [5].

In Section 5.1 a review of the governing fluid mechanic equations is provided as relevant to determine the momentum transfer from the discharge region to the air. Subsequently, time averaged explicit and implicit measurements of the plasma-actuator force (distribution) are introduced and discussed in Section 5.2 and Chapter 6, respectively. In the latter, particular emphasis is placed on the distinction of existing processing strategies and the consequences of different published assumptions on the resulting force and thrust estimations.

5.1 Governing Fluid Mechanic Equations

In this Section the fluid mechanic background is provided as required for the momentum transfer analysis, based on the books of Spurk [210], White [232] and Aris [11], and the governing equations for the force estimation approaches are introduced. To facilitate the subsequent implementation of experimental data, all equations are derived in index notation[1], where Einstein's cartesian summation convention is used (see [11, 210]).

5.1.1 Continuity Equation

The conservation of mass says that the mass m of any bounded piece of fluid has to remain constant with respect to time, i.e.

$$\frac{\mathrm{D}m}{\mathrm{D}t} = 0. \tag{5.1}$$

This mass m is the sum of M mass elements dm, which in continuum theory can be expressed by the spatial integration of the density $\rho(\vec{x}, t)$ over the bounded volume $V(t)$ according to

$$m = \int_M \mathrm{d}m = \iiint_{V(t)} \rho \mathrm{d}V, \tag{5.2}$$

where further application of the material derivative,

$$\frac{\mathrm{D}}{\mathrm{D}t} = \frac{\partial}{\partial t} + u_i \frac{\partial}{\partial x_i}, \tag{5.3}$$

leads to

$$\frac{\mathrm{D}}{\mathrm{D}t} \iiint_{V(t)} \rho \mathrm{d}V = \iiint_{V(t)} \left[\frac{\partial \rho}{\partial t} + \frac{\partial}{\partial x_i}(\rho u_i) \right] \mathrm{d}V = 0. \tag{5.4}$$

The integrand of (5.4) vanishes for infinitesimal size such that the differential form of the continuity equation arises,

$$\frac{\partial \rho}{\partial t} + \frac{\partial}{\partial x_i}(\rho u_i) = 0, \tag{5.5}$$

which can furthermore be rewritten to

$$\frac{\mathrm{D}\rho}{\mathrm{D}t} + \rho \frac{\partial u_i}{\partial x_i} = 0 \tag{5.6}$$

[1] In a few exceptional cases the vector notation is used for clarity.

by means of the material derivative (5.3). Transformation of the left side of (5.2) by means of Reynolds' transport theorem leads to the integral form of the continuity equation

$$\frac{\mathrm{D}}{\mathrm{D}t}\iiint\limits_{V(t)} \rho \mathrm{d}V = \iiint\limits_{V} \frac{\partial \rho}{\partial t}\mathrm{d}V + \iint\limits_{S} \rho u_i n_i \mathrm{d}S = 0, \tag{5.7}$$

where a fixed control volume is considered. The time-derivative term of (5.7) vanishes for steady flow $\partial\rho/\partial t = 0$, such that the remaining expression is

$$\iint\limits_{S} \rho u_i n_i \mathrm{d}S = 0. \tag{5.8}$$

5.1.2 Momentum Balance Equation

The momentum balance as the first axiom of classical mechanics says that in an inertial frame the rate of change of the momentum of a body is balanced by the force applied on this body [210]:

$$\frac{\mathrm{D}I_i}{\mathrm{D}t} = F_i. \tag{5.9}$$

Similar to (5.2) the momentum $I_i = mu_i$ can be expressed by

$$I_i = \iiint\limits_{V(t)} \rho u_i \mathrm{d}V. \tag{5.10}$$

Generally, the sum of forces F_i is divided into volume forces $F_i^{(V)}$ (e.g. gravity) and surface forces $F_i^{(S)}$ (e.g. pressure) according to

$$F_i = \overbrace{\iiint\limits_{V(t)} \rho k_i \mathrm{d}V}^{F_i^{(V)}} + \overbrace{\iint\limits_{S(t)} t_i \mathrm{d}S}^{F_i^{(S)}}. \tag{5.11}$$

Combining (5.10) and (5.11) with (5.9) leads to

$$\frac{\mathrm{D}}{\mathrm{D}t}\iiint\limits_{V(t)} \rho u_i \mathrm{d}V = \iiint\limits_{V(t)} \rho k_i \mathrm{d}V + \iint\limits_{S(t)} t_i \mathrm{d}S. \tag{5.12}$$

Subsequent application of Reynolds' transport theorem on (5.12) results in the integral form of the momentum balance equation

$$\iiint_V \frac{\partial \rho u_i}{\partial t} \mathrm{d}V + \iint_S \rho u_i u_j n_j \mathrm{d}S = \iiint_V \rho k_i \mathrm{d}V + \iint_S t_i \mathrm{d}S, \tag{5.13}$$

which again is reduced to

$$\iint_S \rho u_i u_j n_j \mathrm{d}S = \iiint_V \rho k_i \mathrm{d}V + \iint_S t_i \mathrm{d}S \tag{5.14}$$

for a steady flow ($\partial/\partial t = 0$).

Analogous to (5.5), for an infinitesimal control volume the integration can be omitted in (5.13). Therefore, with further application of Gauss' theorem (5.13) can be transformed to the differential form of the momentum balance

$$\frac{\partial}{\partial t}(\rho u_i) + \frac{\partial}{\partial x_j}(\rho u_i u_j) = \rho k_i + \frac{\partial}{\partial x_j}(\tau_{ji}). \tag{5.15}$$

This equation is known as Cauchy's first law of motion.

5.1.3 Navier-Stokes Equations

Newtonian fluids have a linear relationship between the stress tensor τ_{ij} and the symmetric deformation tensor

$$e_{ij} = \frac{1}{2}\left\{\frac{\partial u_i}{\partial x_j} + \frac{\partial u_j}{\partial x_i}\right\}. \tag{5.16}$$

Hence, these fluids can be defined by the constitutive linear relation of the Cauchy-Poisson law

$$\tau_{ij} = -p\delta_{ij} + \lambda^* e_{kk}\delta_{ij} + 2\eta e_{ij}. \tag{5.17}$$

In (5.17) δ_{ij} is the Kronecker delta, η is the dynamical viscosity and λ^* is the bulk viscosity, which is associated with volume expansion [232].

Combination of the momentum balance (5.15) with the Cauchy-Poisson law (5.17) and the deformation tensor (5.16) leads to the Navier-Stokes equation (NSE)

$$\frac{\mathrm{D}\rho u_i}{\mathrm{D}t} = \rho k_i - \frac{\partial}{\partial x_i}\left\{-p + \lambda^* \frac{\partial u_k}{\partial x_k}\right\} + \frac{\partial}{\partial x_j}\left\{\eta\left[\frac{\partial u_i}{\partial x_j} + \frac{\partial u_j}{\partial x_i}\right]\right\}, \tag{5.18}$$

in which the exchange properties of δ_{ij} have already been applied.

For incompressible flow the material derivative of the density is zero,

$$\frac{\mathrm{D}\rho}{\mathrm{D}t} = 0, \tag{5.19}$$

which, according to (5.6), leads to

$$\frac{\partial u_i}{\partial x_i} = 0. \tag{5.20}$$

Consequently, in consideration of (5.20), for incompressible flows the NSE (5.18) is simplified to

$$\rho\frac{\mathrm{D}u_i}{\mathrm{D}t} = \rho k_i - \frac{\partial p}{\partial x_i} + \eta\frac{\partial^2 u_i}{\partial x_j \partial x_j}. \tag{5.21}$$

Furthermore, by replacing the volume-force term ρk_i by a general volume-force density f_i one obtains

$$\rho\frac{\partial u_i}{\partial t} + \rho u_j\frac{\partial u_i}{\partial x_j} = -\frac{\partial p}{\partial x_i} + \eta\frac{\partial^2 u_i}{\partial x_j \partial x_j} + f_i. \tag{5.22}$$

Based on this general description of a volume force (5.22), an estimation of the plasma-actuator generated source term can be conducted. Assuming steady flow and rearranging (5.22) results in

$$f_i - \frac{\partial p}{\partial x_i} = \rho u_j\frac{\partial u_i}{\partial x_j} - \eta\frac{\partial^2 u_i}{\partial x_j \partial x_j} \tag{5.23}$$

for the estimation of the plasma actuator's body-force distribution (in summation with the pressure gradient).

The validity of assumption (5.19) is demonstrated by Enloe *et al.* [60, 66]. They report maximal density deviations $\Delta\rho$ from the mean density $\bar{\rho}$ in the plasma's immediate vicinity of $\Delta\rho/\bar{\rho} \leq 2\%$.

5.1.4 Vorticity Equation

The vorticity equation derivation begins with (5.22). Taking the curl of the NSE, i.e. applying the operator $\epsilon_{ijk}\frac{\partial}{\partial x_j}$ to (5.22), and use of expression

$$\omega_k = \epsilon_{ijk}\frac{\partial u_i}{\partial x_j} \tag{5.24}$$

for the vorticity ω_k results in

$$\epsilon_{ijk}\frac{\partial f_i}{\partial x_j} = \rho\frac{\partial \omega_k}{\partial t} + \rho u_i\frac{\partial \omega_k}{\partial x_i} - \eta\frac{\partial^2 \omega_k}{\partial x_i \partial x_i}. \tag{5.25}$$

In this formulation of the vorticity equation the assumption of a two-dimensional flow, i.e.

$$\omega_k\frac{\partial u_k}{\partial x_j} = 0, \tag{5.26}$$

has already been made. Furthermore, the time-derivative term in (5.25) vanishes in the case of steady flow, which leaves

$$\epsilon_{ijk}\frac{\partial f_i}{\partial x_j} = \rho u_i\frac{\partial \omega_k}{\partial x_i} - \eta\frac{\partial^2 \omega_k}{\partial x_i \partial x_i} \tag{5.27}$$

for subsequent source term estimations. Note that the formerly present pressure term $\partial p/\partial x_i$ is eliminated in the vorticity equation (5.25) and (5.27).

For the standard case of spanwise orientated (chordwise forcing), unidirectionally implemented plasma actuators as discussed throughout the present work, assumption (5.26) is valid apart from edge effects at the very tips of the devices. However, when implemented in chordwise direction [95, 104] (spanwise forcing) or even more, when the actuator shape is circularly orientated [196, 197] (radial forcing) or shows different curvature [194, 230], then assumption (5.26) is an oversimplification of the flow situation at least in the proximity of the actuator.

5.2 Explicit Measurements

The thrust of the discharge driven wall jet is a convenient measure to quantify the effectiveness of a plasma actuator, as emphasized e.g. by Abe *et al.* [1, 2], Enloe *et al.* [69] or Thomas *et al.* [216]. Experimentation of the temporal evolution of force production is a rather challenging topic, as demonstrated by Enloe *et al.* [62] and Porter *et al.* [177]. Since the push-push vs. push-pull interpretation of the plasma physics has not yet been clarified, ongoing research concentrates on both time-dependent and steady force measurements. Generally, a steady force F can easily and explicitly be measured by means of a weight balance, as described e.g. by Hoskinson *et al.* [101–103] or Gregory *et al.* [92]. This force F should not be understood as the body force F_b produced by the actuator, since it is

actually the body force F_b minus some unknown wall friction force F_f on the surface downstream of the actuator up to the end of the plate carrying the actuator, i.e.

$$\underbrace{\iint_S \rho u_i u_j n_j \mathrm{d}S}_{\text{thrust}} = \underbrace{\iiint_V \rho k_i \mathrm{d}V}_{\text{body force}} + \underbrace{\iint_S t_i \mathrm{d}S}_{\text{friction}} \tag{5.28a}$$

$$F_t = F_b - F_f. \tag{5.28b}$$

This fact is usually neglected in the literature.

Enloe *et al.* [62] distinguished the contribution of the two half-cycles on the plasma force production by means of a torsional pendulum and demonstrated the presence of a self-induced drag counteracting this plasma force. Furthermore, there have been a few attempts made to calculate the friction force from PIV measurements of the wall jet (e.g. Versailles *et al.* [225], Albrecht *et al.* [6]). Due to the very thin wall jet near the electrodes, the relatively high velocities there and the additional uncertainty about the unsteady situation in terms of laminar-turbulent transition, this is a rather challenging task, which will be discussed at length in Section 6. Nevertheless, being aware of the friction force term of (5.28b), a comparison can be made on the basis of the resulting amount of thrust F_t (usable force) released by the body force F_b.

5.2.1 Experimental Procedure

The experimental thrust determination setup comprises three measurement systems, as sketched in Figure 5.1. The plasma actuator is mounted on an acrylic plate, which is connected to a weight balance (KERN PCB 250-3 precision balance, accuracy 1 mg) using a $H_1/H_2 = 3:1$ rocker to amplify the actuator thrust. This particular arrangement allows the simultaneous measurement of the electrical quantities P_A and C_{eff} as explained in Section 3.1, the corresponding plasma length Δx according to Section 4.1 and the resulting thrust F_t by means of the rocker-balance combination.

First, a set of separate experiments on the thrust production F_t of the plasma-actuator was conducted for two different lengths L to verify the independence of the estimated relative thrust F_t/L from the underlying actuator length. In order to match the size of the wind tunnel facilities , the lengths $L_1 = 0.17$ m (cp. Duchmann *et al.* [56]) and $L_2 = 0.44$ m (cp. Grundmann [93]) were used for this preliminary investigation. Thereafter

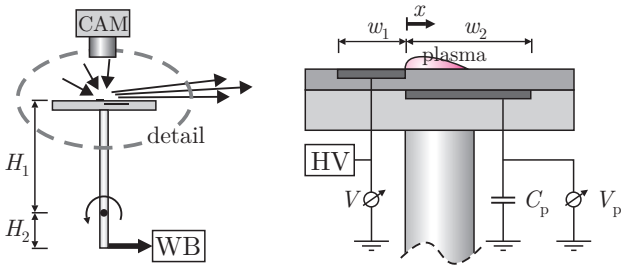

(a) sketch (b) detail

Figure 5.1: Experimental setup: (a) sketch of the test rig comprising overhead camera (CAM), weight balance (WB), rocker (H_1/H_2); (b) detailed view of electrical measurement devices: V actuator voltage, V_p charge-probe voltage, C_p charge-probe capacitor, chordwise plasma distribution.

the power consumption P_A, effective capacitance C_{eff} and plasma length Δx have been measured simultaneously for various operating voltages V and frequencies f, by applying the methods described in Section 3.5 and 4.2. These experiments were performed for an actuator length of $L = 0.45$ m (*1ICb*, see Table 3.1).

5.2.2 Thrust Production Determination

According to the reports of Ferry and Rovey [71], the measured weight-balance signals of operative plasma actuators can be considerably affected during experimentation. This issue has been taken into account by a robust processing strategy, which allows noisy and/or drifting behaviors to be handled: The thrust measurements were conducted by repeatedly operating the actuator, which allowed a multi-step analysis of the resulting weight balance signal $W(t)$. An example of a measured time trace is sketched in Figure 5.2, where additionally all required intermediate quantities are denoted. First, the averaged balance signals $\overline{W}_n$ and corresponding standard deviations σ_{W_n} are calculated for each plateau $n \in N_W$ separately. The ranges of excluded data are identified from the balance-signal derivative $\mathrm{d}W/\mathrm{d}t$, as shaded gray in Figure 5.2.

Subsequently, the averaged thrust F_t produced by the plasma actuator

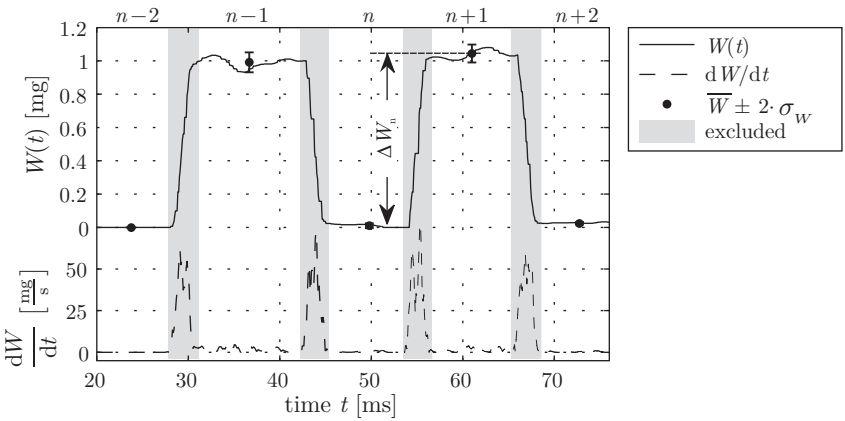

Figure 5.2: Weight-balance signal $W(t)$ and required quantities for estimating the plasma actuator thrust F_t.

can be estimated according to

$$F_t = \frac{H_2}{H_1} \frac{g}{N_W - 1} \sum_{n=1}^{N_W - 1} \Delta W_n, \tag{5.29a}$$

where

$$\Delta W_n = \left| \overline{W}_{n+1} - \overline{W}_n \right|. \tag{5.29b}$$

In contradiction to the previously published reports of non-constant balance signals by Ferry and Rovey [71], neither σ_W nor $\sigma_{\Delta W_n}$ showed significant values for the presented experiments. Therefore, the introduced (post-) processing approach is an appropriate and robust measure for estimating the wall-jet thrust F_t, which corresponds to the usable difference between plasma-actuator body force F_b and the adverse effect of friction F_f.

An example of balance-based plasma-actuator thrust results is shown in Figure 5.3. For lower voltages V, an increasing slope for the thrust F_t is observed, which develops into a linear relation at higher voltages. This result is in good agreement with reports of Van Dyken *et al.* [221] or Thomas *et al.* [216]. Furthermore, two different actuator lengths $L_1 =$

0.17m and $L_2 = 0.44$m were used in order to ensure that the influence of friction at the pivot bearings can be neglected, as demonstrated in Figure 5.3(b).

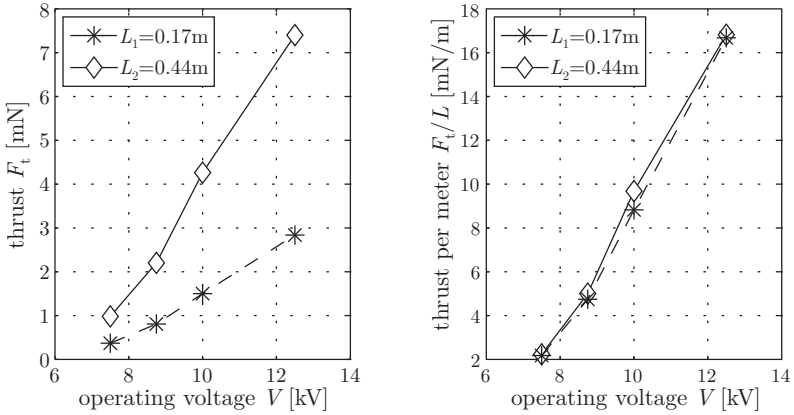

(a) absolute thrust

(b) relative thrust

Figure 5.3: Plasma-actuator thrust F_t for two actuator lengths L ($L_1 = 0.17$ m and $L_2 = 0.44$ m) at $f = 10$ kHz and various operating voltages V; (a) absolute thrust F_t, (b) relative thrust per meter length F_t/L.

5.2.3 Characteristics of Thrust Production and its Effectiveness

For the simultaneously conducted experiments the operating frequency was varied systematically in the range $f = 8 - 13$ kHz. However, only the longest actuator setup ($L = 0.45$ m, *1ICb* see Table 3.1) was used in order to obtain the best possible signal-to-noise ratio (SNR) for the balance measurements. A subsequent calculation of universally valid relative values has been carried out, since the experimental setup works accurately enough, as demonstrated in Figure 5.3(b). The results are shown in Figure 5.4.

Here the resulting thrust per length F_t/L is presented as a function of several discharge specific quantities. For instance, Figure 5.4(a) shows the actuator thrust as a function of the operating voltage V. In good agreement with the results of Thomas *et al.* [216], the observed thrust rises with the

frequency. This result comes as no surprise, since it has been demonstrated in Chapter 3 that both operating voltage V and frequency f significantly affect the resulting performance of plasma actuators. Consequently, in order to quantify any DBD actuator scenario, either both variables have to be presented together or the more precise correlations, as introduced and discussed in Sections 3.2, 3.4 and 4.2, should be chosen.

A thrust-power diagram is plotted in Figure 5.4(b), as already shown by Van Dyken *et al.* [221] or Gregory *et al.* [92], for instance. Note the positive slopes of the resulting curves, which are slightly decreasing at higher values of P_A/L. This shape of the thrust-power diagram already suggests the beginning of the repeatedly reported wall-jet saturation of at $U_{\max} \approx 8$ m/s (see e.g. Boeuf *et al.* [28] or Moreau *et al.* [157]), where the electrical power consumption P_A has to be strongly increased for further wall-jet acceleration and consequently further thrust augmentation. Illustrative examples are given by Van Dyken *et al.* [221] and Forte *et al.* [79], for instance.

This effect is more clearly demonstrated in Figure 5.5, where the fluid mechanic effectiveness[2] η^*_{FM} according to definition (2.8b) is presented. A similar dimensioned coefficient has already been suggested by different authors. Ferry and Rovey [71] introduce the so-called *actuator effectiveness*. Other authors (e.g. Gregory *et al.* [92], Hoskinson *et al.* [101, 102] and Porter *et al.* [179]) in contrast, refer to it as the *force (production) efficiency* or simply keep the term *thrust* (Enloe *et al.* [69]).

[2] Recall the discrepancy between the term *efficiency* and a dimensioned coefficient according to definition (2.8b) and the corresponding explanation in Section 2.3.

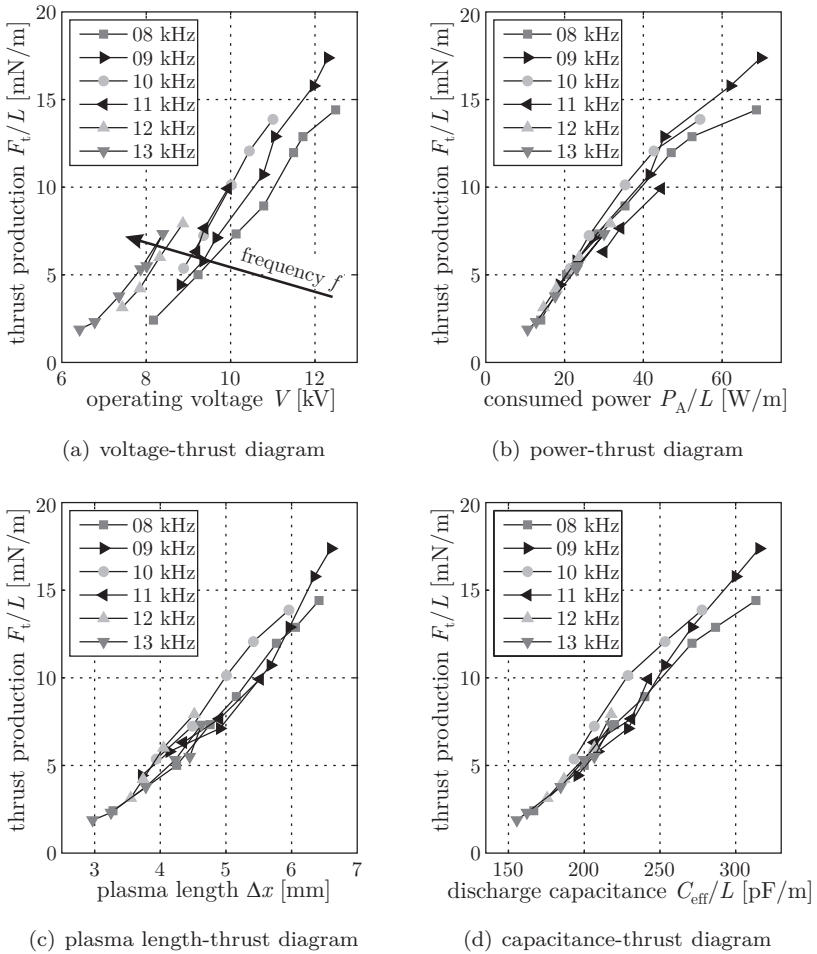

(a) voltage-thrust diagram

(b) power-thrust diagram

(c) plasma length-thrust diagram

(d) capacitance-thrust diagram

Figure 5.4: Plasma-actuator thrust F_t/L as a function of discharge specific variables for several frequencies f: (a) operating voltage V; (b) consumed power P_A/L; (c) plasma length Δx; (d) effective discharge capacitance C_{eff}/L.

The resulting curves of the $\eta^*_{\mathrm{FM}} - P_A$ diagram (Figure 5.5(a)) confirm the above mentioned assumption of a beginning wall-jet saturation: For the particular actuator dimensions and materials chosen for the present work, the most effective momentum transfer takes place at $P_A/L \approx 40$ W/m for the entire measured voltage-frequency combinations (Figure 5.5(b)).

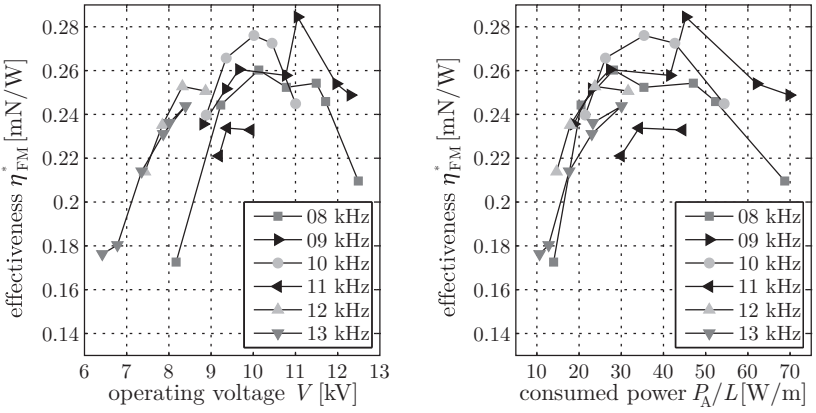

(a) $\eta^*_{\mathrm{FM}} - V$ diagram (b) $\eta^*_{\mathrm{FM}} - P_A$ diagram

Figure 5.5: Fluid mechanic effectiveness η^*_{FM} as a function of operating voltage V (a) and consumed power P_A (b) for several frequencies f.

In addition to the conventional interrelationships, based on the above processing strategies, Figures 5.4(c) and 5.4(d) show the actuator thrust F_t/L as a function of the novel evaluation measures, i.e. plasma length Δx and discharge capacitance C_{eff}. A comparison of Figures 5.4(a) and 5.4(c) indicates that the slopes are identical for the different experiments. In addition to that, the resulting plots in the $\Delta x - F_t/L$ diagram of Figure 5.4(c) collapse for the entire measured frequency range $f = 8 - 13$kHz. This result demonstrates the improved robustness of the plasma-length based description of the actuator thrust, since the complex presentation of combined voltage-frequency parameter information is no longer necessary. A similar comparison can be performed with Figures 5.4(b) and 5.4(d). The slopes of these two diagrams look similar, as well. Therefore, it is possible to easily switch between the two representations depending on the purpose of the measurement. Figure 5.4(b) is favorable to document and discuss

results of precisely adjusted power levels, whereas Figure 5.4(d) should be preferred for adjusting the impedance of the actuator system. Since both representations can be derived from one and the same measurement, it is strongly recommended to calculate both, the consumed power P_A and the effective discharge capacitance C_{eff}.

In conclusion, these experiments provide a deeper insight into the plasma actuator performance characterization. Measurement of the electrical and optical discharge-specific quantities of an operative plasma actuator is simple and easy to implement but all the more promising to characterize and quantify the actuator performance. In particular, power consumption P_A, effective capacitance C_{eff} and plasma length Δx have proven to be appropriate measures to describe the the resulting thrust production of plasma actuators without the formerly required detailed knowledge of operating voltage and frequency. Based on the simultaneously obtained data valuable new correlations are identified.

These interactions allow to draw the conclusion that a combined analysis of power consumption P_A, effective discharge capacitance C_{eff} and corresponding plasma length Δx provides a universal and robust means to characterize, quantify and predict the DBD based thrust production for flow-control applications. Finally, this data provides an excellent benchmark for implicit estimations of thrust and body-force production based on experimentally determined velocity information.

6 Momentum Transfer to the Air II: Implicit Measurements and Comparison

The direct determination of the momentum induced in the flow by the presence of an operative plasma actuator has been introduced and discussed in Section 5.2 alongside with explicit weight-balance based thrust measurements. Generally, a common and widely used alternative to explicitly measuring the momentum imparted to the flow is the experimental determination of the resulting velocity distribution, where the forces acting on the flow are subsequently implicitly estimated based on fluid mechanic balance equations. In most cases, where only surface forces $\vec{t}$ contribute to the momentum transfer and no source term $\vec{k}$ is present inside the observed fluid volume, the so-called Control Volume Analysis allows a reliable calculation of the forces acting on the flow (see e.g. Dabiri [48], Rival *et al.* [185, 186] or van Oudheusden *et al.* [222, 223]).

As discussed before and already considered in Section 5.1, the plasma-actuator force contributes an additional source term to the governing equations. Accurate estimation of this additional source term based on velocity measurements is a rather challenging task. A comparison of recent publications on the topic of implicit plasma-actuator force determination approaches demonstrates that there still remains uncertainty concerning a reliable distinction of valid assumptions and oversimplifications.

Hence, a comparative analysis of various existing implicit force estimation strategies [6, 17, 103, 118, 225, 234] is performed in this Chapter, in particular clarifying the effects of different assumptions and simplifications on the calculated results. The underlying data base of velocity distributions for this evaluation is generated by means of Particle Image Velocimetry (PIV) experiments in proximity of an operative plasma actuator, which allow the direct comparison of integral and differential methods based on identical measurements.

6.1 Experimental Procedure

To investigate the flow behavior and especially the momentum transfer to the flow, PIV measurements have been conducted in close proximity to the discharge region of the actuator. Different operating voltages $V = 8 - 12$ kV ($f = 11$ kHz) were applied to investigate the influence of the electrical power level on the resulting force and thrust production.

6.1.1 Experimental Setup

The experimental setup is sketched in Figure 6.1. It comprises two separate systems for simultaneous measurements of electrical characteristics of the DBD actuator and the resulting flow-field in proximity of the discharge domain. The electrical measurements were carried out as described extensively in Chapter 3 to record and calculate operating voltage V and power consumption P_A of the actuator. The plasma actuator is flush-mounted on a black acrylic plate to prevent reflections. For orientation purposes the wall-jet direction as well as the origins and directions of x- and y-coordinates are also included in Figure 6.1.

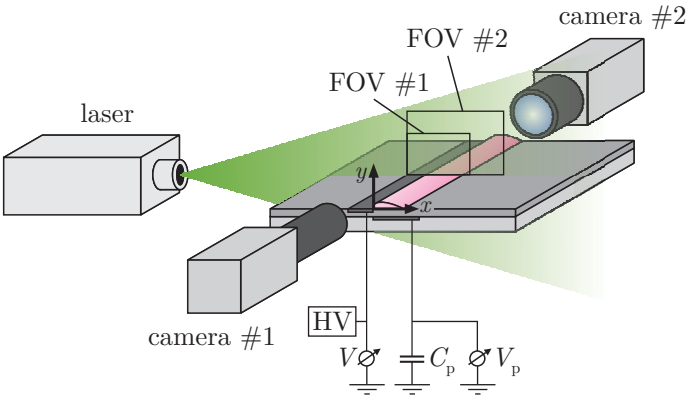

Figure 6.1: Sketch of the experimental PIV setup.

A commercial high-speed PIV system[1] comprising a Litron Nd:YLF ($\lambda = 527$ nm) dual-cavity laser and two Phantom V12 high-resolution cameras (12 bit, maximum resolution 1280×800 pixels) was utilized, which was operated in single-frame mode at a repetition rate of 10k frames per second (fps) and a pulse duration of 150 ns. This high repetition rate with $\Delta t = 100\,\mu$s required the reduction of the spatial resolution down to 800×600 pixels. A maximum number of $N = 10k$ images per run per camera was recorded, exploiting the available buffer capacity of 8 GB. The cameras were mounted facing one another perpendicular to the laser-light sheet as sketched in Figure 6.1. This arrangement allowed the simultaneous observation of two different fields of view (FOV). This choice provided the highest possible spatial resolution (81.3 pix/mm) in the plasma's immediate vicinity, suitable for force calculations (FOV #1). In addition, the spatial distribution of the resulting wall-jet downstream of the discharge domain can be characterized for identical experimental realizations with FOV #2, which has approximately half the spatial resolution (42.2 pix/mm) but spans twice the physical domain compared to FOV #1. A reversely mounted[2] 120 mm SKR SYMMAR lens and a 105 mm Nikon Nikkor lens were fitted to span the observation dimensions 10×7 mm^2 (FOV #1) and 19×14 mm^2 (FOV #2) respectively.

The smallest actuator length ($L = 0.15$ m, *1IAb* see Table 3.1) was used for the experiments to allow optical access from both sides with the given focal lengths of the lenses. The test section was enclosed in a closed plexiglass containment (450×325×345 mm^3) with quartz-glass windows to assure best possible quality of optical accesses for laser-light sheet and cameras. Di-Ethyl-Hexyl-Sebacat (DEHS) aerosol (mean diameter 0.9 μm) is used to seed the containment. A detailed list of components and settings is given in Table 6.1.

The issue of electrophoretic forces acting on the seeding particles has been studied by Kim *et al.* [114], for instance. Based on a direct experimental comparison of the seeding particle-density distribution in the presence and absence of DBD they report a negligible influence of seeding particle charging on the resulting velocity measurements. This conclusion is confirmed by theoretical estimations of Wilke [234]. Furthermore, a comparative study

[1] It was found in preliminary PIV studies [154, 234] that the highest possible frame rate (10k fps) is essential for adequate data accuracy in terms of second and third derivatives of experimentally obtained velocity data as used in the Navier-Stokes and vorticity equations (see Section 5.1).

[2] This particular setting was chosen to reduce the observed domain beyond the lens' lower magnification limit of 1:1.

Table 6.1: Components of the implemented PIV setup: Chosen product, properties and corresponding settings.

component	product	settings/properties
test section	perspex containment	dimensions (length/width/height): 450 mm/325 mm/345 mm
laser	Litron Lasers Model LDY303-PIV	laser medium: Nd:YLF 527 nm, 70 W pulse duration: 150 ns
cameras	2×Phantom V12	800×600 pixels, 10000 fps
lens #1 (FOV #1)	Schneider-Kreuznach SKR SYMMAR 120/5.6-0.33X (reverse mode!)	focal length: f=120 mm field of view: 10×7 mm resolution: 81.3 pix/mm
lens #2 (FOV #2)	Nikon Nikkor 105 mm f/2.8 AF-Micro	focal length: f=105 mm field of view: 19×14 mm resolution: 42.2 pix/mm
seeding	DEHS	mean diameter 0.9 μm
Software	Dynamic Studio (Dantec Dynamics)	Versions 2.1 and 2.3

of Boucinha *et al.* [32] leads to the conclusion that the accuracy of the determined airflow velocity is mainly depends on the accuracy of the entire measurement setup, whereas the impact of a particular chosen tracer substance is of minor importance. Following these reports, the issue of seeding charging is presumed to be negligible in this work.

Although the major objective of the PIV investigations was a force (distribution) quantification and the spatial resolution of FOV #1 fulfilled the corresponding requirements to the setup, the availability of a second camera (FOV #2) was found to be extremely beneficial for future work. Based on the calculated DBD source terms from FOV #1 (see Section 6.3.2), these additional velocity data from FOV #2, comprising a fully developed wall jet, are available for validation of future[3] numerical simulations including the DBD source term as determined in the present work from FOV #1.

[3] At the date of publication of the present work, such efforts are already underway at TU Darmstadt.

6.1.2 PIV Data Processing

The velocity distributions were calculated from the raw data using commercial software (Dynamic Studio). The maximum accuracy of PIV algorithms is in the range of 0.1 pixel (see e.g. Nobach and Bodenschatz [160]), which results in a (theoretical) velocity accuracy of the order 10^{-2}m/s for the present parameter settings. To achieve the best possible accuracy, first the raw images were cut to the range of interest (ROI) and the signal-to-noise ratio (SNR) was improved by subtracting the image mean. Subsequently, the $N-1$ flow fields $U_i(x,y)$ were calculated with a multi-grid cross-correlation algorithm ('adaptive correlation'). Rectangular interrogation areas (IAs) with a final/initial size of 64×16 / 512×128 pixels and 32×16 / 256×128 pixels and 75% overlap were chosen for FOV #1 and FOV #2 respectively, to fulfil the requirements of calculating a wall jet's velocity profile, i.e. strong wall-normal velocity gradients ($\partial u_i/\partial y \gg \partial u_i/\partial x$) and high wall-parallel velocities ($u \gg v$). Furthermore, window deformation and a Gaussian window function ($k = 2$) were applied for the velocity-distribution calculations. Outliers ($< 5\%$) were eliminated using a neighborhood validation (3×3).

The time averaged velocity distribution $u_i(x,y)$ and corresponding standard deviation σ_{u_i} were subsequently calculated according to

$$u_i(x,y) = \frac{1}{N-1}\sum_{n=1}^{N-1} U_i(x,y,\Delta t_n) \tag{6.1}$$

and

$$\sigma_{u_i} = \sqrt{\frac{1}{N-2}\sum_{n=1}^{N-1}\Big[U_i(x,y,\Delta t_n) - u_i(x,y)\Big]^2}. \tag{6.2}$$

To assure statistical significance of the averaged data, four characteristic flowfield locations are chosen to estimate the convergence of the time averaged data in terms of relative standard deviations of the velocity σ_u/u for increasing number of records N taken into account. These locations are in particular (A) the zone above the discharge domain, where a suction towards the DBD occurs at low velocities, (B) the shear layer between wall jet and quiescent air directly above (C) the location of the fastest measured wall-jet velocity and (D) the fully developed wall-jet profile. The relative standard deviation σ_u/u for locations A-D as a function of the number of records N is shown in Figure 6.2. Similar convergence diagrams of particle-based velocimetry have been published e.g. by Benard and Moreau [23]

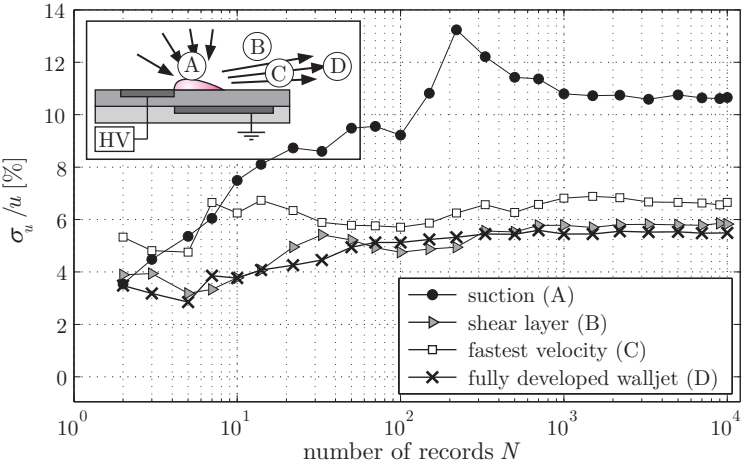

Figure 6.2: Statistical significance of the PIV data at characteristic locations: Sketch of sample locations and convergence diagram of relative standard deviations σ_u/u (average of 3×3 data points); A-C: FOV #1, D: FOV #2; operating voltage $V = 12$ kV.

(time-resolved PIV), Greenblatt *et al.* [91] (LDA) or Widmann *et al.* [233] (phased-locked PIV). From Figure 6.2 it can be concluded that statistical significance was ensured by recording $N = 10k$ images per measured operating voltage V. Note the high ratio of $\sigma_u/u(> 10\%)$ for convergence at location (A), where the AC character of the discharge is perceptible.

For more details about PIV and the corresponding data (post) processing, the reader is referred to Adrian [3, 4], Raffel *et al.* [181], Tropea *et al.* [217] and Westerweel [231].

6.1.3 Electrical Results

The main discharge specific quantities of the plasma actuator (power consumption P_A and actuator capacitances C_0, C_{eff}) are determined as described in Chapter 3 and are plotted in Figure 6.3 for the measured parameter range of the PIV experiments. To demonstrate the reproducibility of actuator construction and electrical experimentation, results of the electrical experiments as described in Chapter 3 for identical operating conditions are added to the diagrams (cp. Figures 3.5(a) and 3.17(a), *1IAb*, 11 kHz).

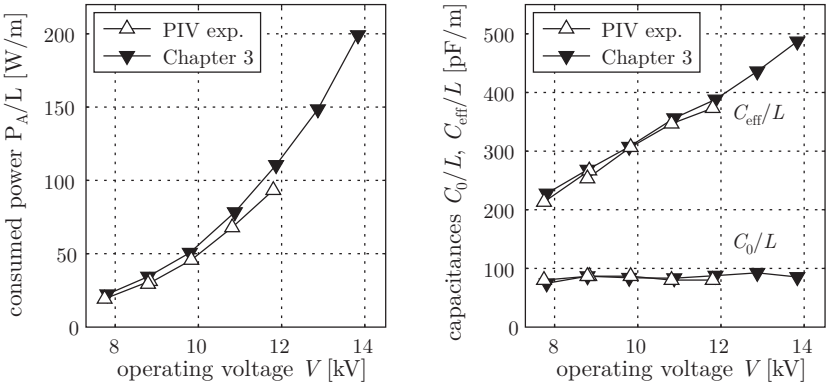

(a) $P_A - V$ diagram (b) $C - V$ diagram

Figure 6.3: Electrical plasma-actuator performance for the measured parameter range of the PIV experiments; (a) power consumption P_A, (b) Capacitances: Cold capacitance C_0 and effective discharge capacitance C_{eff}.

6.2 Wall-Jet Characteristics

Example results of the velocity distribution from the strongest actuation ($V = 12$ kV) are shown in Figure 6.4 for both FOVs. Additionally, the chosen control volume (CV) for the subsequent force estimation procedure is denoted in Figures 6.4(a) and FOV #1 is indicated in 6.4(b), both sketched with white dashed lines. The chordwise extension of the CV (8.3 mm) is chosen based on the results presented in Chapter 4, where a plasma length of $\Delta x \approx 6.5$ mm was measured for $V = 12$ kV (cp. Figure 4.4(a)).

The basis of the implicit force estimation approaches is the characterization of the resulting airflow with best possible accuracy. The quality of these velocity profiles is decisive for the accuracy of any results from subsequent calculations. Figure 6.5 shows the velocity profiles of the entire measured operating conditions for both FOVs, where the location $x = 6$ mm is chosen as a matching interface. Qualitatively, the spatial resolutions of both FOVs lead to the same profiles, but the limited resolution of FOV #2 can be noticed especially for the fastest (thinnest) wall jets in Figure 6.5(b), where only one single velocity data point is available between wall ($y = 0$) and velocity maximum $u_{\max}$.

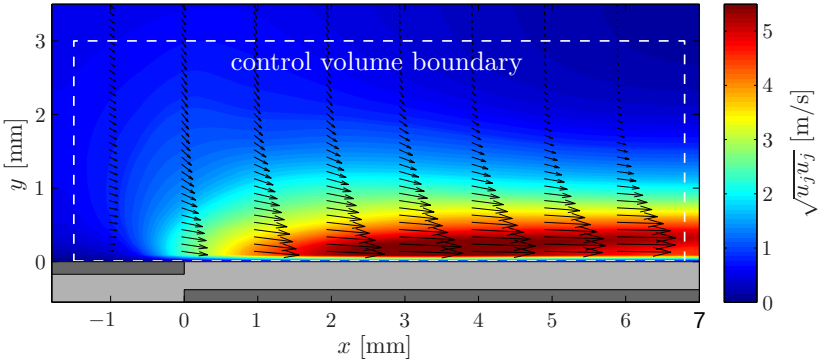

(a) FOV #1 and implemented CV

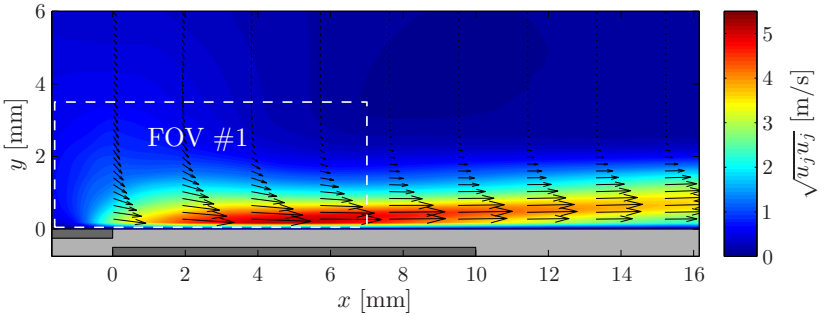

(b) FOV #2 (FOV #1 indicated)

Figure 6.4: Velocity distribution of the resulting wall jet ($V = 12$ kV, $f = 11$ kHz) for both FOVs; contour levels: velocity magnitude $\sqrt{u_j u_j}$, vectors: extract of velocity profiles; white dashed lines indicate implemented control volume (a) and FOV #1 (b).

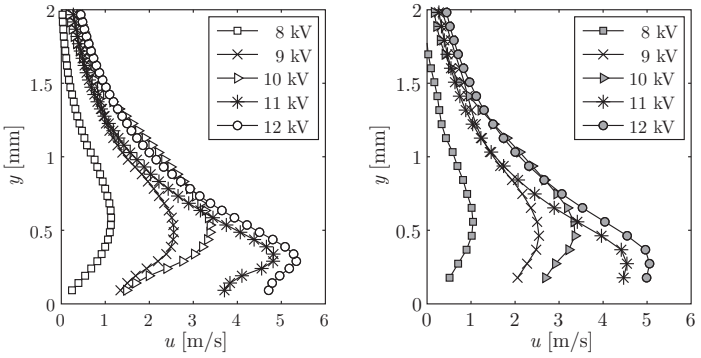

(a) FOV #1 (b) FOV #2

Figure 6.5: Wall jet velocity profiles $u(x=6\text{ mm}, y)$ for all measured operating voltages $V = 8 - 12$ kV.

Generally, the velocity profile of a wall jet is characterized by its thickness δ and the characteristic maximum velocity $u_{\max}$ (Glauert [89]). An accurate estimation of δ from experimental data is very challenging. Therefore, the wall normal distance of 50% jet velocity serves as a more robust spatial measure to scale the profile, i.e.

$$\delta_{1/2} = y\left(\frac{u_{\max}}{2}\right). \tag{6.3}$$

Based on the data of Figure 6.5, Figure 6.6 shows example wall-jet profiles, normalized by

$$u^* = \frac{u}{u_{\max}} \quad \text{and} \quad y^* = \frac{y}{\delta_{1/2}}. \tag{6.4}$$

Furthermore, the data of $x = 16$ mm (FOV #2) are included in the diagram. Similar non-dimensional wall jet profiles have been published for plasma-actuator wall jets by Jukes *et al.* [112] or Thomas *et al.* [216], for instance. Jukes *et al.* [112] additionally presented the theoretical profiles for laminar and turbulent wall jets according to Glauert [89], where $y^*(u_{\max})\big|_{\text{lam.}} \approx 0.5$ and $y^*(u_{\max})\big|_{\text{turb.}} \approx 0.25$. With these data it can be concluded from Figure 6.6 that the plasma-actuator generates a laminar wall jet. For a more detailed insight into the characteristics and optimization of discharge based wall jets, the reader is referred to Balcon *et al.*

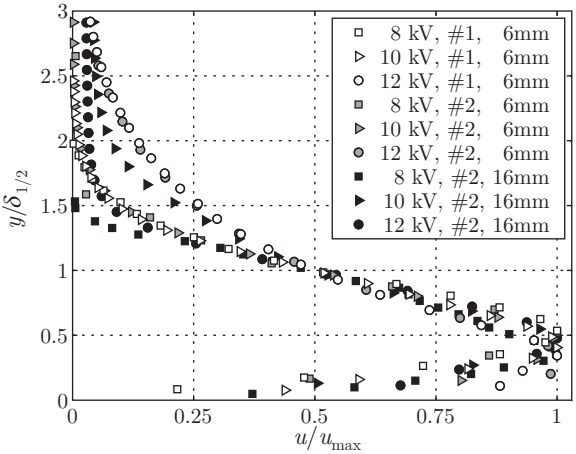

Figure 6.6: Non-dimensional velocity profiles of the wall jet;
$u(x=6\text{mm}, y)$: both FOVs, $u(x=16\text{mm}, y)$: FOV #2;
operating voltages: $V = 8, 10, 12$ kV.

[14], Forte *et al.* [78, 79], Jolibois *et al.* [108–110], Jukes *et al.* [112] and Thomas *et al.* [216].

6.3 Force Estimation Approaches

At first, as an overview over existing strategies of plasma-actuator force estimation, all integral [17, 103, 118, 225] and differential [6, 234] methods are briefly introduced. In Figure 6.7 the control volumes (CV) are sketched, which are required for both integral and differential approaches. The dimensions of the chosen CV are $x_{min} = -1.5$ mm, $x_{max} = 6.8$ mm, and $y_{min} = 0$ (wall boundary) and $y_{max} = 4$ mm. For all approaches the flow is assumed to be two-dimensional, steady, of constant viscosity and incompressible (cp. Section 5.1).

6.3.1 Integral Methods

All implemented integral methods originate from the momentum balance equation (5.14) applied in x-direction (free index $i \mathrel{\hat{=}} x$), where the first

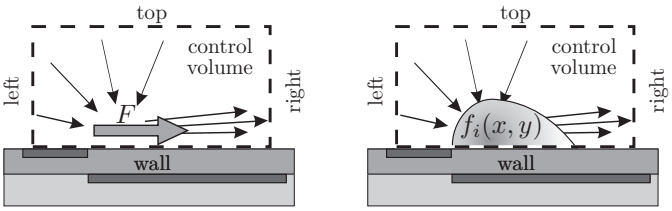

(a) integral force value F (b) force distribution $f(x, y)$

Figure 6.7: Sketch of the implemented control volume and chosen boundary nomenclature as used for the force estimation: Velocity distribution is sketched with black arrows, force is shaded gray.

right-hand-side term of the general volume force k_i is substituted by the unknown plasma force $F_i := F$. In order not to confuse the reader while introducing and comparing the approaches, it is refrained from distinguishing between the body force F_b and the resulting thrust F_t in this Section. Based on the respective assumptions and simplifications, all approaches have originally been suggested to characterize the plasma actuator performance, which will be simply denoted as F here. Further interpretations and conclusions drawn from the different results will clarify this issue retroactively in Section 6.4.

Assuming steady, incompressible 2D flow and assuming no contributions of the t_i-integral on any of the outer control volume surfaces, (5.14) reduces to

$$\frac{F}{L} = \rho \int_{\text{right}} u^2 \, \mathrm{d}y - \rho \int_{\text{left}} u^2 \, \mathrm{d}y + \rho \int_{\text{top}} uv \, \mathrm{d}x + \int_{\text{wall}} \tau_w \, \mathrm{d}x, \tag{6.5}$$

with F as the only unknown. However, depending on the available measurement equipment (e.g. PIV, LDA[4], CTA[5], Pitot probe) further simplifications may be required in such that certain right-hand-side terms of (6.5) are neglected. Depending on the degree of simplification the integral methods can be subdivided into four different cases, which are briefly described in the following and are listed below in Table 6.2.

Case 1: Versailles *et al.* [225] process their PIV-data taking all terms of (6.5) into account. Based on the no-slip wall condition they calculate

[4]Laser Doppler Anemometry
[5]Constant Temperature Anemometry

the wall-shear stress by means of the first data point above the wall according to

$$\tau_w = \mu \left. \frac{\Delta u}{\Delta y} \right|_{1.\mathrm{IA}}, \tag{6.6}$$

where the first row of interrogation areas is used for the determination. Insertion of (6.6) into (6.5) leads to

$$\frac{F}{L} = \rho \int_{\mathrm{right}} u^2 \, \mathrm{d}y - \rho \int_{\mathrm{left}} u^2 \, \mathrm{d}y + \rho \int_{\mathrm{top}} uv \, \mathrm{d}x + \mu \int_{\mathrm{wall}} \left. \frac{\Delta u}{\Delta y} \right|_{1.\mathrm{IA}} \mathrm{d}x. \tag{6.7}$$

for the force term estimation.

Case 2: In contrast to Case 1, Durscher and Roy [58] and Kotsonis *et al.* [117, 118] only calculate the momentum flux crossing the control-volume boundaries of their PIV domain according to

$$\frac{F}{L} = \rho \int_{\mathrm{right}} u^2 \, \mathrm{d}y - \rho \int_{\mathrm{left}} u^2 \, \mathrm{d}y + \rho \int_{\mathrm{top}} uv \, \mathrm{d}x. \tag{6.8}$$

Thus the force calculated by this method directly corresponds to the left side of (5.28), where the actuator thrust is characterized.

Case 3: Hoskinson *et al.* [102, 103] estimate the actuator force based on Pitot-tube measurements. In addition to neglecting the wall-shear stress they further assume the flux over the left and top CV-boundaries to be negligible (quiescent air), which reduces the right side of (6.5) to the first term:

$$\frac{F}{L} = \rho \int_{\mathrm{right}} u^2 \, \mathrm{d}y. \tag{6.9}$$

Similar approaches are reported by Greenblatt *et al.* [91] ('time-mean jet momentum'), Little *et al.* [144] ('time-mean momentum addition') or Mestiri *et al.* [151] ('tangential force'), where the integration domain of the latter only takes the half width of the jet into account[6]. It is important to mention at this point that Hoskinson *et*

[6] In particular, Mestiri *et al.* [151] perform the integration of (6.9) only between the wall $y = 0$ and the maximum jet velocity $y = y(u_{\max})$, but they do not provide further explanations for this reduction of their domain.

al. [102, 103] in retrospect draw the conclusion from one additional test that neglecting the inflow boundary is the coarsest simplification of (6.5).

Case 4: Baughn *et al.* [17] conclude from boundary-layer experiments that the velocity profile at the left boundary is almost unaffected by the presence of the plasma-actuator force. Therefore, they only measure the velocities at the right boundary and calculate the top boundary based on the continuity equation. They furthermore demonstrate the importance of the friction term by comparing the resulting boundary-layer profile of experiments with and without plasma-actuator operation. Since the present work only considers quiescent air measurements, the approach of Baughn *et al.* [17] is modified accordingly without changing the original idea:

$$\frac{F}{L} = \rho \int_{\text{right}} u^2 \,\mathrm{d}y + \rho \int_{\text{top}} uv \,\mathrm{d}x + \mu \int_{\text{wall}} \left. \frac{\Delta u}{\Delta y} \right|_{\text{1.IA}} \mathrm{d}x. \tag{6.10}$$

A summary of the chosen methods and corresponding simplifications is given in Table 6.2.

Table 6.2: List of implemented integral approaches based on (6.5) including respective simplifications; ✓ ≙ taken into account, × ≙ neglected.

case	$\frac{F}{L} = \rho \int_{\text{right}} u^2 \,\mathrm{d}y - \rho \int_{\text{left}} u^2 \,\mathrm{d}y + \rho \int_{\text{top}} uv \,\mathrm{d}x + \int_{\text{wall}} \tau_w \mathrm{d}x$				equation
1	✓	✓	✓	✓	(6.7)
2	✓	✓	✓	×	(6.8)
3	✓	×	×	×	(6.9)
4	✓	×	✓	✓	(6.10)

The influence of the dimensions of the chosen control volume to the results of each right-hand-side term of (6.5) is demonstrated in Figure 6.8 for the velocity distribution of the strongest wall jet ($V = 12$ kV). The sum of all terms, which corresponds to the calculated force F/L, is also shown in the diagram. The x-location of the right boundary ($x_{\max}$) is varied systematically starting at $x_{\max} = x_{\min} = -1.5$ mm up to the final position $x_{\max} = 6.8$ mm. For the initial position $x_{\max} = x_{\min}$ the terms of the top

and wall boundary are zero and the left and right boundaries only differ in sign by definition.

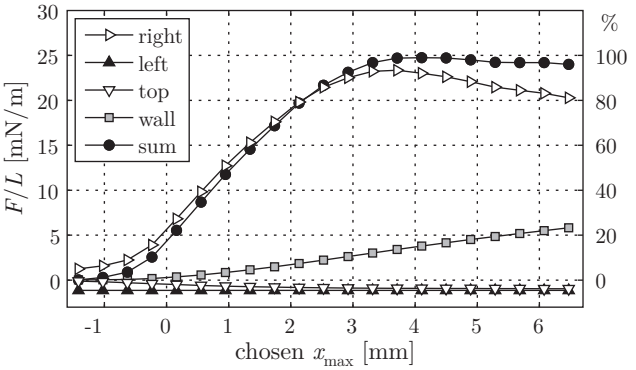

Figure 6.8: Contribution of each right-hand side term of (6.5) to the calculated force F/L as a function of the chordwise control-volume size, i.e. chosen x_{max}; $x_{min} = -1.5$ mm = constant, operating voltage $V = 12$ kV.

The individual contributions of the different terms of (6.5) can easily be quantified by the right ordinate in Figure 6.8. As expected, the major part of the force is generated by the wall jet, which leaves the CV across the right boundary. The second dominant influence on the calculated force obviously is the effect of wall friction. The top and left boundaries have only minor influence on the results. Furthermore, the almost constant values of the force at both ends of the corresponding curve confirm that the chosen final CV size contains the entire plasma-actuator force.

6.3.2 Differential Methods

Insight into the spatial distribution of the induced body force requires differential force estimation methods, which are based either on the Navier-Stokes equations (Case 5)

$$f_x - \frac{\partial p}{\partial x} = \rho\left(u\frac{\partial u}{\partial x} + v\frac{\partial u}{\partial y}\right) - \eta\left(\frac{\partial^2 u}{\partial x^2} + \frac{\partial^2 u}{\partial y^2}\right), \qquad (6.11a)$$

$$f_y - \frac{\partial p}{\partial y} = \rho\left(u\frac{\partial v}{\partial x} + v\frac{\partial v}{\partial y}\right) - \eta\left(\frac{\partial^2 v}{\partial x^2} + \frac{\partial^2 v}{\partial y^2}\right) \qquad (6.11b)$$

or on the vorticity equation (Case 6)

$$\frac{1}{\rho}\left(\frac{\partial f_x}{\partial y}-\frac{\partial f_y}{\partial x}\right)=u\frac{\partial \omega}{\partial x}+v\frac{\partial \omega}{\partial y}-\frac{\eta}{\rho}\left(\frac{\partial^2 \omega}{\partial x^2}+\frac{\partial^2 \omega}{\partial y^2}\right). \tag{6.12}$$

For the sake of clarity, the equations (6.11) and (6.12) are repeated here based on (5.23) and (5.27), respectively, where the general indices i, j have already been exchanged by x, y, following Einstein's summation convention (see [11, 210]). The vorticity ω_k of the two dimensional x, y-problem contributes only in the third dimension z. Therefore, this remaining vorticity component ω_z is expressed without index throughout this chapter, i.e. $\omega_k \xrightarrow{\text{2D}} \omega_z := \omega$.

Case 5: Since the system (6.11) consists of only two equations for the three unknowns force densities f_x, f_y and the pressure distribution p, further assumptions have to be made. Wilke [234] assumed (and retroactively verified) that the force term f_i is of at least one order of magnitude larger than the pressure gradients over the entire control volume, i.e.

$$|f_i| \gg \left|\frac{\partial p}{\partial x_i}\right|. \tag{6.13}$$

Consequently, the pressure gradients are neglected

$$\frac{\partial p}{\partial x_i} := 0 \tag{6.14}$$

and the two remaining unknowns f_i of system (6.11) can be calculated according to

$$f_x(x,y) = \rho\left(u\frac{\partial u}{\partial x}+v\frac{\partial u}{\partial y}\right)-\eta\left(\frac{\partial^2 u}{\partial x^2}+\frac{\partial^2 u}{\partial y^2}\right), \tag{6.15a}$$

$$f_y(x,y) = \rho\left(u\frac{\partial v}{\partial x}+v\frac{\partial v}{\partial y}\right)-\eta\left(\frac{\partial^2 v}{\partial x^2}+\frac{\partial^2 v}{\partial y^2}\right). \tag{6.15b}$$

Case 6: In order to deal with the problem of unknown pressure-gradients $\partial p/\partial x_i$ Albrecht *et al.* [6] successfully demonstrated a vorticity-equation based estimation of volume forces according to (6.12), where the pressure gradients are eliminated. Since two unknowns f_x and f_y still appear in (6.12), it is further assumed that the curl of the force is strongly dominated by $\partial f_x/\partial y$, i.e.

$$\frac{\partial f_x}{\partial y} \gg \frac{\partial f_y}{\partial x}. \tag{6.16}$$

Following (6.16) the chordwise gradient $\partial f_y/\partial x$ is neglected,

$$\frac{\partial f_y}{\partial x} := 0, \tag{6.17}$$

and the force gradient $\partial f_x/\partial y$ can be calculated according to

$$\frac{1}{\rho}\frac{\partial f_x}{\partial y} = u\frac{\partial \omega}{\partial x} + v\frac{\partial \omega}{\partial y} - \frac{\eta}{\rho}\left(\frac{\partial^2 \omega}{\partial x^2} + \frac{\partial^2 \omega}{\partial y^2}\right). \tag{6.18}$$

Subsequent numerical integration leads to

$$f_x(x,y) = -\rho \int_{\infty}^{0} \left[u\frac{\partial \omega}{\partial x} + v\frac{\partial \omega}{\partial y} - \frac{\eta}{\rho}\left(\frac{\partial^2 \omega}{\partial x^2} + \frac{\partial^2 \omega}{\partial y^2}\right)\right] \mathrm{d}y. \tag{6.19}$$

The plasma-actuator force is unknown at the wall ($y = 0$) and assumed to be zero at the top CV boundary. Since the cumulative trapezoidal numerical integration as used for the calculations needs an initial value, the integration limits are exchanged in (6.19) and the sign is changed following Albrecht *et al.* [6].

Assumption (6.16) is examined carefully and in more detail in Section 6.5, based on the results of Case 5, from which both force components f_i are available.

6.4 Comparison of the Integral Forces (Cases 1-6)

6.4.1 Integration of Cases 5 and 6

In order to compare the differential approaches with the integral approaches (Cases 1-4), the force distributions $f_x(x,y)$ of the differential Cases 5 and 6 are integrated over the entire control volume (CV) according to

$$\frac{F}{L} = \iint_{A_{\mathrm{CV}}} f \mathrm{d}A_{\mathrm{CV}} = \int_{y_{\min}}^{y_{\max}} \int_{x_{\min}}^{x_{\max}} f_x(x,y)\, \mathrm{d}x\mathrm{d}y. \tag{6.20}$$

An extensive discussion of the spatial distribution of the force $f_i(x,y)$ will follow in Section 6.5.

6.4.2 Comparison of the Approaches

All calculated results of the actuator force F are plotted in Figure 6.9. Note that the colored lines denote the PIV-based results, whereas the gray shaded lines belong to explicitly measured thrust values by means of the weight balance experiments (see Section 5.2). This combined representation allows a direct comparison of implicitly and explicitly achieved results. The discussion of the results follows the order of the legend entries in Figure 6.9.

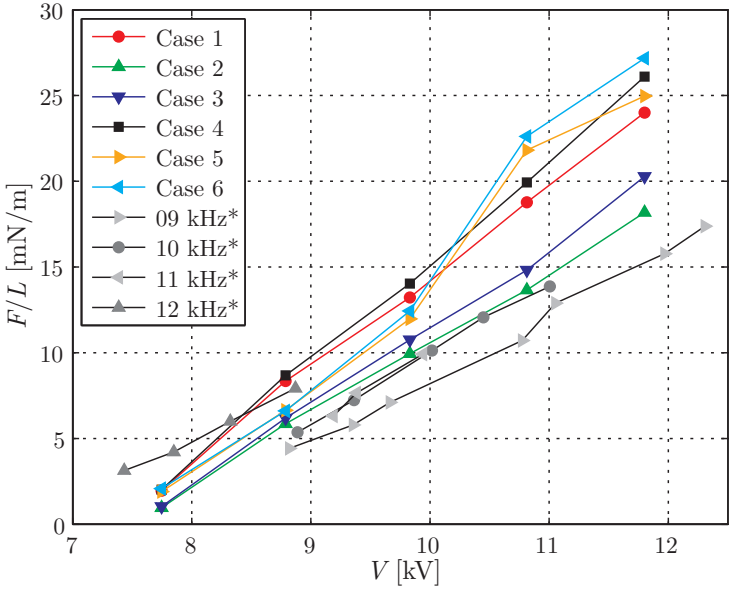

Figure 6.9: Plasma-actuator force F/L as a function of operating voltage V; implemented Cases 1-6 of the present study appear colored (f=11 kHz), balance based data appear gray (*explicit weight balance based measurements, cp. Section 5.2).

Case 1 (–●–) includes all four boundaries for the calculation of the force. Comparison with Case 2 (–▲–, neglected wall boundary) clearly shows the importance of the wall-shear stress τ_w for the result, since a 30% drop of the calculated force is observed. This difference occurs due to the self-induced drag as indicated in Figure 6.8 and explicitly reported by Enloe *et al.* [62].

Consequently, the estimated force is too weak when neglecting the friction and Case 2 only results in the net thrust of the created wall jet. Case 3 (–▼–) only takes the right boundary into account. Since the top and left boundaries add negative values to the results, this case results in a larger force compared to Case 2. In Case 4 (–■–) only the negative left boundary is neglected from the balance, resulting in larger values when compared with Case 1, which considers all terms.

The curves of the two differential Cases 5 (–►–) and 6 (–◄–) are less smooth in comparison to the integral approaches. In particular, the determined forces of the 11 kV-experiment show unexpectedly high values for both differential approaches. The increased uncertainty apparently occurs, because up to second (Case 5) and even third order (Case 6) derivatives of PIV data are included in the calculation of the force distribution $f_i(x, y)$ and a subsequent spatial integration according to (6.20) is implemented to obtain the integral force. Nevertheless, at first glance, both differential methods show good agreement with one another, which strengthens the validity of the two different assumptions (6.13) and (6.16). A deeper insight into these assumptions is provided in Section 6.5. As expected, both differential Cases (5 and 6) fluctuate around the values of Case 1, since the latter calculates the force F as an integral source term according to Figure 6.7(a).

Furthermore, Figure 6.9 includes the comparison with the weight balance based data as introduced in Section 5.2, which explicitly measures the resulting thrust of the actuator forced wall jet according to (5.28b). Therefore, it comes as no surprise that Case 2 matches these data best, since this Case mimics the thrust measurements by neglecting the wall shear stress term (cp. Table 6.2).

6.5 Force-Distribution Analysis

This Section addresses the spatial force distributions $f_i(x, y)$ as determined according to Cases 5 and 6 and the contribution of each term to the respective result.

6.5.1 Case 5 (Navier-Stokes Equation)

Beginning with the Navier-Stokes equation based Case 5, the contours of the force distributions $f_x(x, y)$ and $f_y(x, y)$ according to (6.15) are shown in Figure 6.10 for the operating voltage of $V = 12$ kV, exemplarily. Furthermore, a 10% isoline ($\max[f_x]/10$) is plotted to denote the momentum-transfer domain. This threshold turned out to be a convenient indicator for the boundary of the force domain, since on the one hand the force magnitude is reduced by one order. On the other hand the signal-to-noise ratio for this threshold still allows separation of the force from background noise.

The direct comparison of different orders of magnitude in the color codings of Figures 6.10(a) and 6.10(b) clearly shows that the momentum transfer from the discharge to the surrounding air is predominated through the x-component of the force $f_x(x, y)$. In accordance with detailed numerical simulations (see e.g. Boeuf *et al.* [26–28] or Unfer *et al.* [219, 220]), the maximum values of the force density can be observed close to the upper electrode's trailing edge ($x = 0$) slightly downstream in the range of $x = 1 - 2$ mm. Farther downstream, at larger x values, the force decreases. Note the layer of negative force values farther downstream directly above the wall boundary, which at first glance appears unexpected. To clarify this issue, the contributions of the convective and diffusive terms of (6.15a) are presented separately in Figure 6.11(a,b) and 6.11(c,d), where the above introduced 10% isoline is again included for orientation purposes.

Obviously, the major contribution to the calculated force $f_x(x, y)$ is produced by the convective terms $\rho u_j(\partial u/\partial x_j)$, as shown in Figures 6.11(a) and 6.11(b). Due to the strong convective acceleration $\partial u/\partial x$ the convective term in x-direction constitutes the high force amplitudes in the left part of the force domain. The wall normal term additionally augments the the force domain further downstream. The diffusive terms $\eta(\partial^2 u/\partial x_j \partial x_j)$ contribute only to a minor extent to the resulting force distribution. The wall normal diffusive term, $\eta(\partial^2 u/\partial y^2)$, denotes the ridge of the wall jet, where the negative changing rate of the slope of the wall-jet profile is maximal at maximal velocities. The term of chordwise diffusion $\eta(\partial^2 u/\partial x^2)$ is negligible (order of ± 10 N/m^3). Obviously, at some extent downstream

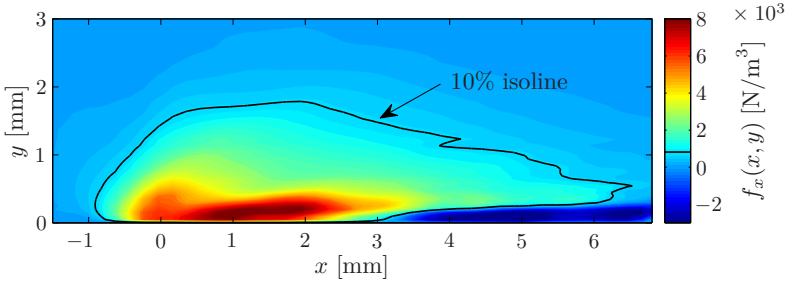

(a) x-component $f_x(x, y)$

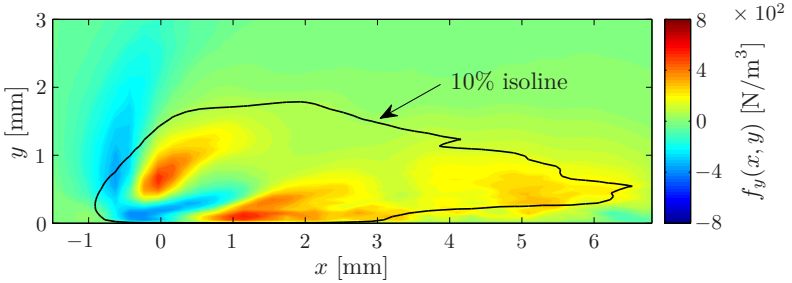

(b) y-component $f_y(x, y)$

Figure 6.10: Force distributions $f_x(x, y)$ (a) and $f_y(x, y)$ (b) determined according to Case 5 (6.15); the 10% isoline ($\max[f_x]/10$) indicates the momentum transfer domain; note the different orders of magnitude; $V = 12$ kV, $f = 11$ kHz.

the attenuated actuator force $f_x(x, y)$ is dominated by shear forces of the wall jet's boundary layer, thus leading to a deceleration of the flow within that shear layer. Consequently, as the sign of $\partial u/\partial x$ changes from plus to minus, the shear introduces negative values for the 'source term', which has been addressed in some recent publications.

Font *et al.* [74], for instance, conclude that 'a large part of the force imparted by the actuator on the air (70-90%) is almost immediately lost to the drag of the air with the adjacent wall surface'. Enloe *et al.* [62] specify this performance drop, as they introduce the term 'self-induced drag' based on the proportionality of the surface drag to the wall-normal velocity gradient $\partial u/\partial y$ (cp. (6.6)). Following these reports, the counteraction of the drag scales with the imparted momentum to the air, since an increased wall-jet

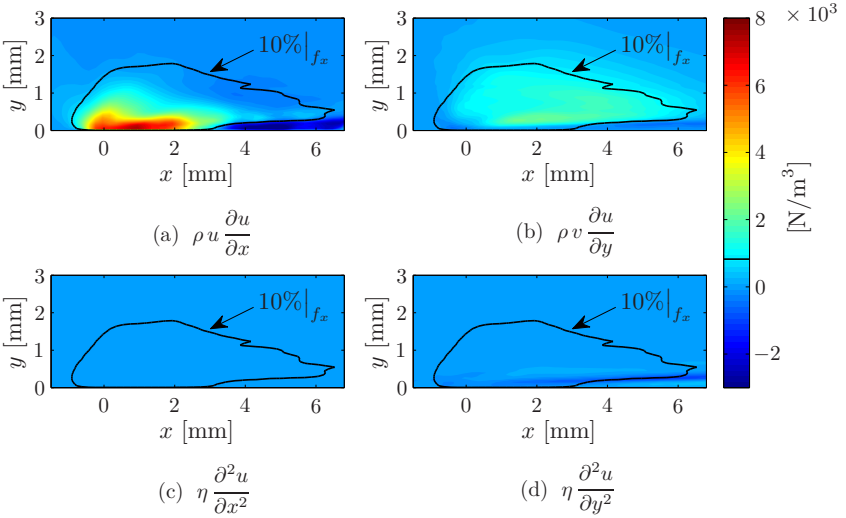

Figure 6.11: Contribution of the right-hand-side terms of (6.15a) to the resulting x-component of the source term $f_x(x, y)$; (a,b) convective terms, (c,d) diffusive terms; color coding and 10% isoline identical with Figure 6.10; $V = 12$ kV, $f = 11$ kHz.

velocity introduces an increased velocity gradient $\partial u/\partial y$. However, this issue clearly demonstrates the limitations of inverse approaches to calculate the applied source term from the resulting velocity field, where a careful distinction between cause and effect is only possible based on thorough interpretation of the results.

Although ranging one order of magnitude below the x-component of the source term $f_x(x, y)$, the y-component $f_y(x, y)$ (see Figure 6.10) is splitted into its terms as shown in Figure 6.12. Note the changed resolution of the color coding, where the upper and lower limits represent plus and minus 10% of the maximum x-forces as indicated in the diagrams with an isoline. Similar to $f_x(x, y)$ the y-component of the force $f_y(x, y)$ is predominated by the contribution of the convective terms $\rho u_j(\partial v/\partial x_j)$. Generally, the suction towards the wall leads to negative values of v. Consequently, an acceleration towards the wall leads to negative gradients $\partial v/\partial y$. After multiplication with the negative velocity component v results in positive values for $\rho v(\partial v/\partial y)$, which occupies the entire 10% domain in Figure 6.12(b).

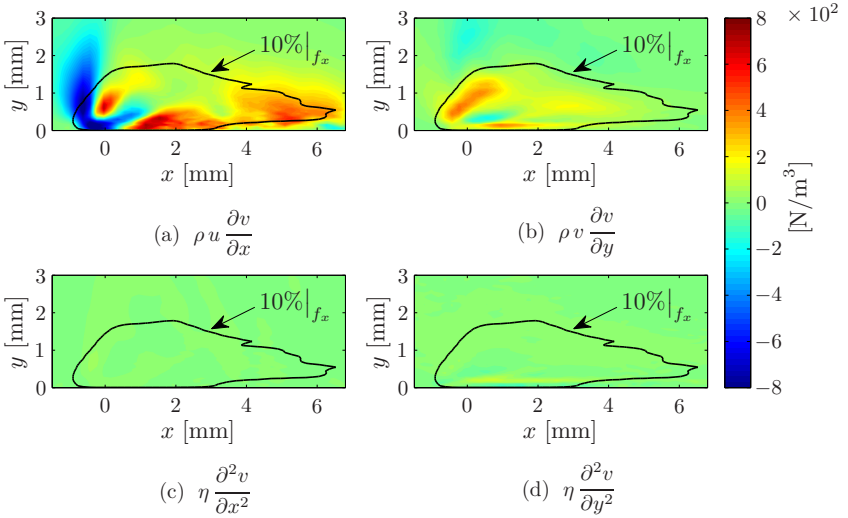

Figure 6.12: Contribution of the right-hand-side terms of (6.15b) to the resulting x-component of the source term $f_y(x, y)$; (a,b) convective terms, (c,d) diffusive terms; color coding and 10% isoline identical with Figure 6.10; $V = 12$ kV, $f = 11$ kHz.

The sign change of the chordwise convective term in Figure 6.12(a) above the upper electrodes trailing edge ($x = 0$) indicates the maximal (chordwise) suction strength towards the wall, i.e. $\partial v/\partial x \approx 0$. The contributions of the diffuse terms $\eta(\partial^2 v/\partial x_j \partial x_j)$ to the force distribution $f_y(x, y)$ are one more order of magnitude smaller than the convective terms, lying two orders of magnitude below $f_x(x, y)$.

6.5.2 Case 6 (Vorticity Equation)

6.5.2.1 Evaluation of Assumption (6.16)

To provide an assessment basis for the validity of assumption (6.16) of Case 6, i.e.

$$\frac{\partial f_x}{\partial y} \gg \frac{\partial f_y}{\partial x}, \quad \text{(identical with (6.16))} \tag{6.21}$$

both terms are determined from the force distributions $f_i(x, y)$ of Case 5. The resulting force gradients $\partial f_x/\partial y$ and $\partial f_y/\partial x$ are shown in Figures 6.13(a) and 6.13(b), respectively. Following the depiction of Figure 6.10 the color coding of the two components varies by one order of magnitude, which already supports assumption (6.21).

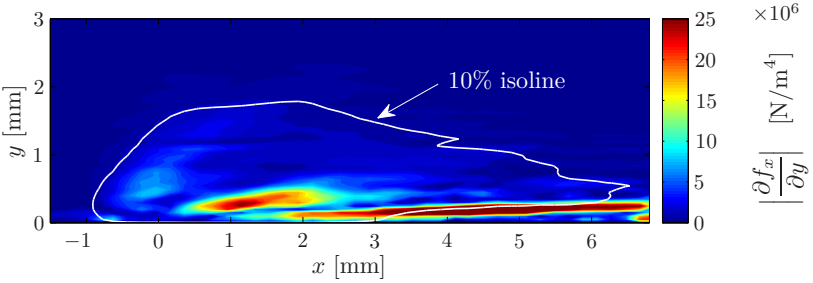

(a) $\partial f_x/\partial y$

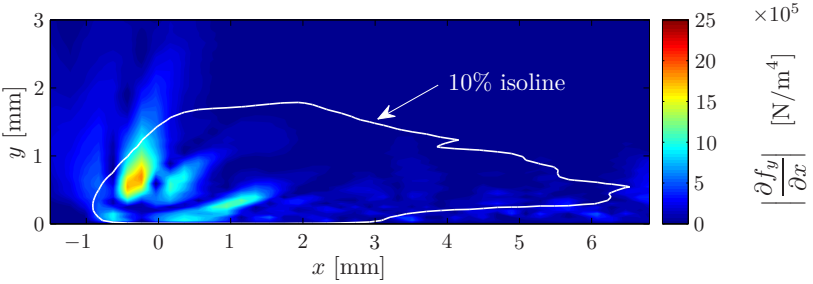

(b) $\partial f_y/\partial x$

Figure 6.13: Spatial distribution of the force gradients calculated from the results of Case 5; the 10% isoline ($\max[f_x]/10$) indicates the momentum transfer domain; note the different orders of magnitude; $V = 12$ kV, $f = 11$ kHz.

This is elucidated in a more quantitative manner in Figure 6.14, where the ratio of the absolute values ofboth gradients are shown according to

$$\left|\frac{\partial f_y}{\partial x}\right| \Big/ \left|\frac{\partial f_x}{\partial y}\right|. \tag{6.22}$$

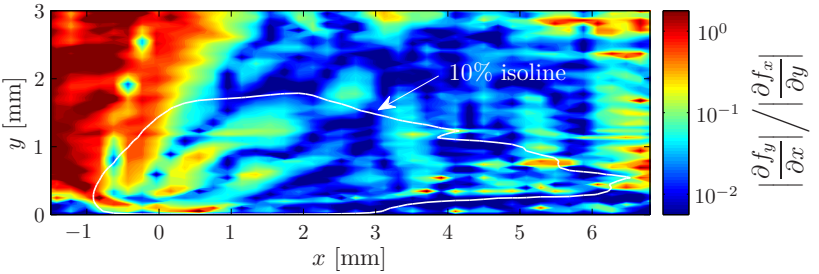

Figure 6.14: Ratio of the force gradients $\partial f_y/\partial x$ and $\partial f_x/\partial y$; the 10% isoline ($\max[f_x]/10$) indicates the momentum transfer domain; note the logarithmic color coding; $V = 12$ kV, $f = 11$ kHz.

The logarithmic color coding of Figure 6.14 visualizes the order of magnitude of the ratio (6.22). Above the upper electrode in the range of negative x values, numerator and denominator of (6.22) are of the same order of magnitude, entailing that assumption (6.21) is invalid in this region. A comparison with Figure 6.13 leads to the conclusion that this region is mainly constituted by the ratio of small values. Moreover, the 10% isoline used in the previous Figures is included in the diagram and demarcates the relevant domain for the validity of assumption (6.21). Apparently, the main part of the invalid region is excluded from the force domain, which confirms the validity of assumption (6.21) with sufficient (spatial) accuracy.

6.5.2.2 Force Distribution (Case 6)

For the vorticity equation based Case 6, the contour of the force distribution $f_x(x, y)$ according to (6.19) is shown in Figure 6.15 for the operating voltage of $V = 12$ kV, similar to Figure 6.10(a). Again, a 10% isoline of the force ($\max[f_x]/10$) indicates the relevant force domain. From a preliminary qualitative comparison of Figures 6.15 and 6.10(a) it can be seen that the maximum values, the gross distribution and the overall size of the produced

force are comparable, although differing slightly with respect to the space and force intensity.

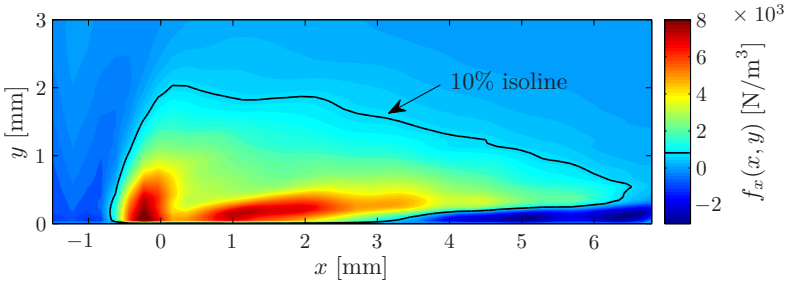

Figure 6.15: Force distribution $f_x(x, y)$ determined according to Case 6 (6.19); the 10% isoline ($\max[f_x]/10$) indicates the momentum transfer domain; $V = 12$ kV, $f = 11$ kHz.

The resulting distribution is further differentiated by directly comparing the distribution of each underlying term as used for the determination. Therefore, the contribution of the right-hand-side terms of (6.19) to the resulting source term $f_x(x, y)$ are shown in Figure 6.16. The convective (a,b) and diffusive (c,d) terms of the vorticity equation are integrated separately for the diagrams to allow best possible comparison with Figure 6.11. All four diagrams of Figure 6.16 reveal identical characteristics similar to Figure 6.11. The contributions of the convective terms predominate those of the diffusive terms. Especially the x-component of the convection, $\rho\, u\, (\partial\omega/\partial x)$, shows identical patterns of acceleration and deceleration above the dielectric surface.

In conclusion, the main characteristics of the expected source term distribution $f_x(x, y)$ are determined with both differential approaches, thus being available for numerical simulations of DBD-based flow control applications. Furthermore, Case 5 on the one hand additionally provides information of the wall-normal momentum transfer $f_y(x, y)$, which is lost by definition in Case 6. On the other hand the influences of the unknown pressure gradients $\partial p/\partial x_i$ remain to be clarified in Case 5. Wilke [234] retroactively verified the validity of assumption (6.14) with a numerical simulation of his results in a quiescent air environment.

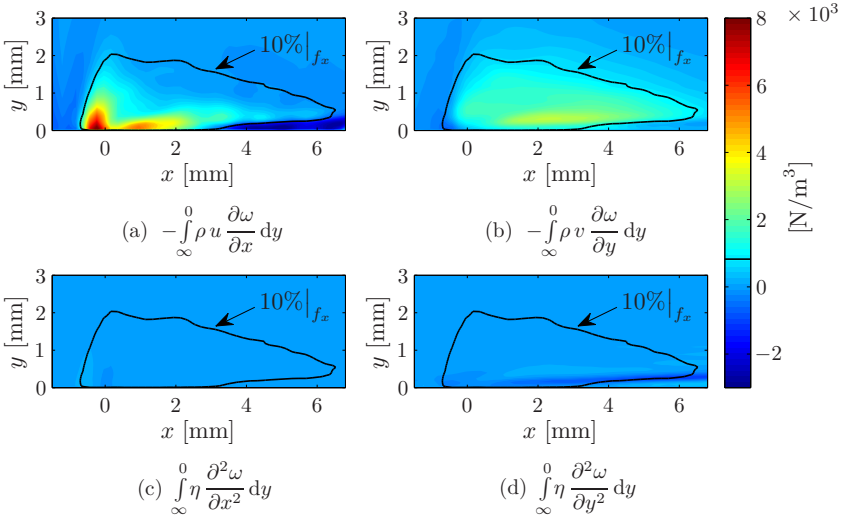

Figure 6.16: Contribution of the right-hand-side terms of (6.19) to the resulting source term $f_x(x, y)$; (a,b) convective terms, (c,d) diffusive terms; color coding and 10% isoline identical with Figure 6.15; $V = 12$ kV, $f = 11$ kHz.

6.5.3 Correlation of Force Domain and Plasma Length

In Sections 6.5.1 - 6.5.2 the 10% isolines of the determined force distributions have already been introduced to demarcate the momentum transfer domain within the recorded velocity distributions. The spatial (chordwise) extent of this domain is furthermore a valuable measure in terms of a characteristic momentum transfer length scale, which can easily be extracted from the characteristic domains.

For all measured operating voltages V the 10% isolines are summarized in Figure 6.17. The chordwise extent of the momentum transfer domain can be compared with the chordwise plasma length Δx, described in Chapter 4. It is therefore denoted Δx_F, as sketched in Figure 6.17(a) for the 12 kV experiment, where the index $_F$ is added to assure the distinction of force-determination based and light-emission based (no index) derivation of the similar quantity.

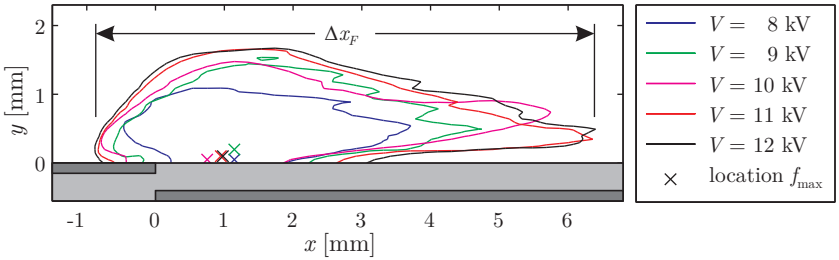

(a) Case 5; Navier-Stokes-equation based approach

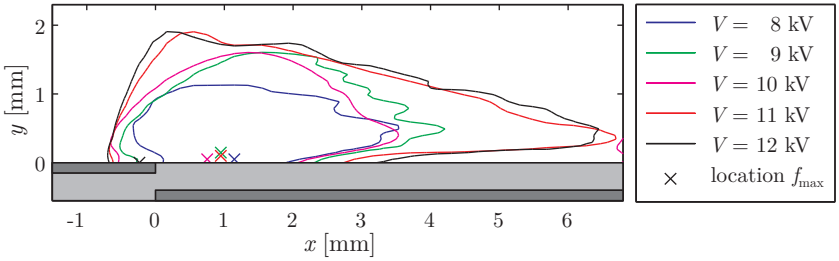

(b) Case 6; vorticity-equation based approach

Figure 6.17: 10% isolines of the force distribution $f_x(x, y)$ for all operating voltages V (f=11 kHz); (a) Case 5, (b) Case 6.

Obviously, the size of the volume force domain grows with increasing operating voltage V, whereas the location of the experiments' maximum force intensity (marked with crosses of the respective color) varies only slightly. In accordance with the results of Section 6.4, the isoline of the 11 kV experiment shows an unexpectedly large domain. The values of Δx_F are shown in Figure 6.18 as a function of the operating voltage. The resulting plasma length Δx of the discharge luminosity obtained by gray-value analysis (Chapter 4) is also included in the diagram (cp. Figure 4.4(a)). The aforementioned sensitivity of the PIV-based calculations is clearly recognizable. In particular, it can be concluded from the spatial extent of the isolines that the vorticity equation based approach (Case 6) is less favorable than the application of the Navier-Stokes equation (Case 5). The latter uses up to second derivatives of PIV data, whereas the former uses up to third derivatives and subsequent numerical integration.

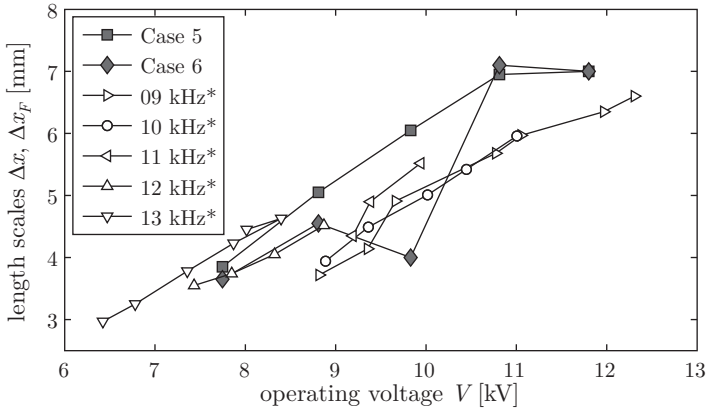

Figure 6.18: Plasma length Δx as function of operating voltage V; dark markers: estimated momentum transfer length Δx_F based on the 10% isolines of Figure 6.17; white markers: Measured plasma length Δx based on light emission analysis (*: cp. Figure 4.4(a)).

Nevertheless, the similar characteristics of the plasma length Δx and the length of the momentum transfer domain Δx_F can be clearly identified from Figure 6.18, which extends the results of Enloe *et al.* [68, 69]. It can therefore be drawn as an inverse conclusion that the plasma length Δx indeed serves as a measure for the penetration length of the momentum transfer.

This is an important insight, since only one experiment is required to gather spatial information about the momentum transfer domain - either from PIV experiments or even easier via light intensity analysis - from which the required length scale can be extracted. Based on the known plasma length-discharge capacitance correlation, as demonstrated in Figure 4.5, the extracted length scale can be subsequently utilized to transform a force-capacitance interrelation ($F - C_{\text{eff}}$), for instance simply recorded with oscilloscope and weight balance as demonstrated in Chapter 5, into a force-penetration length interrelation ($F - \Delta x_F$).

6.6 Evaluation of Fluid Mechanic Efficiency and Effectiveness

To evaluate the above introduced Cases 1-6 in terms of fluid mechanic efficiency and effectiveness according to (2.8a) and (2.8b) respectively, further processing of the determined forces is required.

Multiplication of Cauchy's first law of motion (5.15) with a characteristic velocity gives the mechanical energy equation, which in combination with the first law of thermodynamics defines the conservation equation of energy [210]. In the present context, therefore, all implemented force-estimation approaches have to be multiplied with the local velocity scale. The force distributions $f_i(x, y)$ can be directly processed to obtain the fluid mechanic power

$$\frac{P_{\mathrm{FM}}}{L} = \iint\limits_{A_{\mathrm{CV}}} f_i u_i \mathrm{d}A_{\mathrm{CV}} = \int\limits_{y_{\min}}^{y_{\max}} \int\limits_{x_{\min}}^{x_{\max}} f_i(x,y) u_i(x,y)\ \mathrm{d}x\mathrm{d}y \tag{6.23}$$

for the Cases 5 and 6, similar to the force distribution integration (6.20), as recently suggested by Giepman and Kotsonis [88]. The integral approaches have to be recalculated based on (6.5) multiplied with the (local) velocities according to

$$\frac{P_{\mathrm{FM}}}{L} = \rho \int\limits_{\mathrm{right}} u^3\ \mathrm{d}y - \rho \int\limits_{\mathrm{left}} u^3\ \mathrm{d}y + \rho \int\limits_{\mathrm{top}} u^2 v\ \mathrm{d}x. \tag{6.24}$$

The wall-stress integral has already been excluded from (6.24), since the term $\tau_w u$ vanishes due to the no-slip condition and the corresponding multiplication with zero. Consequently, regarding the integral approaches, only Cases 2 and 3 are taken into account for the following discussion. Case 3 only considers the first right-hand-side term of (6.24), which directly corresponds to the reported power-estimation approaches of Jolibois and Moreau [110], Léger *et al.* [135] and Pons *et al.* [175].

The fluid mechanic power P_{FM}, as calculated according to (6.23) and (6.24), is shown in Figure 6.19 as a function of operating voltage V and power consumption P_A. The integral and differential approaches are indicated by triangles and squares, respectively. Similar to the force determination (see Figure 6.9), the results obtained from the 11 kV experiment, post-processed according to the differential approaches, show unexpectedly high values. Therefore, dashed lines are added into all diagrams of this

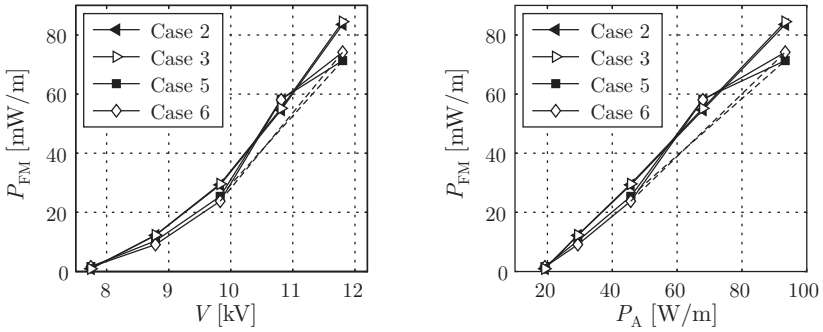

(a) $P_{\mathrm{FM}} - V$ diagram

(b) $P_{\mathrm{FM}} - P_A$ diagram

Figure 6.19: Fluid mechanic power P_{FM} of the plasma-actuator as a function of operating voltage V (a) and power consumption P_A (b) for the parameter range of the PIV experiments.

section, which directly connect the results of the 10 kV and the 12 kV experiments of the differential cases; hence indicating the expected slopes of the respective diagrams.

The slope of the $P_{\mathrm{FM}} - V$ diagram of Figure 6.19(a) shows very good agreement with the $P_A - V$ diagram of Figure 6.3(a). Additionally, power data P_{FM} and P_A are plotted against one another in Figure 6.19(b). At first glance the $P_{\mathrm{FM}} - P_A$ diagram shows a constant slope, which would correspond to a constant fluid mechanic efficiency η_{FM} according to (2.8a). As demonstrated in Figure 6.20, this in fact is not the case when the $P_{\mathrm{FM}} - P_A$ curve has a horizontal offset.

It can clearly be recognized that the fluid mechanic efficiency η_{FM} increases with increasing operating voltage V and corresponding power consumption P_A, even though with decreasing slopes. Especially Figure 6.20(b) shows a significantly decreasing slope of the efficiency towards a maximum in the range of $\eta_{\mathrm{FM}} \approx 0.1\%$ above a consumed power of $P_A \approx 100$ W/m. This result is in very good agreement with the reports of Jolibois and Moreau [110] for similar actuator setup, where the maximum efficiency ($< 0.1\%$) for sine-wave actuation is achieved at $P_A \approx 100$ W/m and a slight efficiency reduction is identified for $P_A > 100$ W/m.

The fluid mechanic effectiveness η^*_{FM} according to (2.8b) is shown in Figure 6.21 as a function of operating voltage V and power consumption

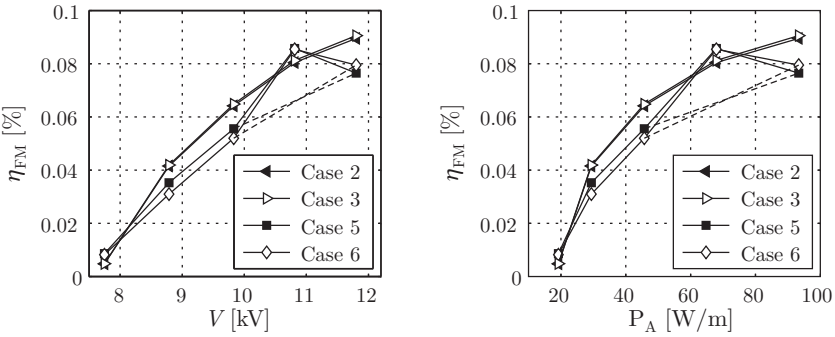

(a) $\eta_{\mathrm{FM}} - V$ diagram

(b) $\eta_{\mathrm{FM}} - P_A$ diagram

Figure 6.20: Fluid mechanic efficiency η_{FM} of the plasma-actuator as a function of operating voltage V (a) and power consumption P_A (b) for the parameter range of the PIV experiments.

P_A, following the results of the weight-balance based thrust measurements (see Section 5.2), where no velocity information was measured.

In accordance with the results shown in Figure 5.5 the effectiveness increases strongly for low power consumption $P_A \leq 45$ W/m. At higher operating levels ($P_A \geq 45$ W/m) the calculated effectiveness remains almost constant. Calculated from identical raw data, Figures 6.20 and 6.21 furthermore allow a direct and quantitative comparison of the two performance-characterization methods, i.e. explicit thrust measurements and implicit determination of thrust and fluid mechanic power from experimentally obtained velocity information. Obviously, the optimal operating conditions in terms of optimal efficiency and optimal effectiveness might differ significantly. This is an essential insight for any plasma-actuator performance-optimization effort, since it sheds light on the issue of limited comparability among the researcher groups, as recently emphasized by Little *et al.* [144].

Note the changed order of curves: In Figures 6.19 and 6.20 the integral approaches (triangles) show higher values as compared to the differential ones (squares), whereas the differential cases show the higher values in Figure 6.21. This effect is clarified in Figure 6.22, in which the results of efficiency and effectiveness are plotted against one another. From both integral Cases 2 and 3 higher efficiency η_{FM} is calculated per effectiveness η^*_{FM} than from the differential Cases 5 and 6 (see Figure 6.22(a)). The underly-

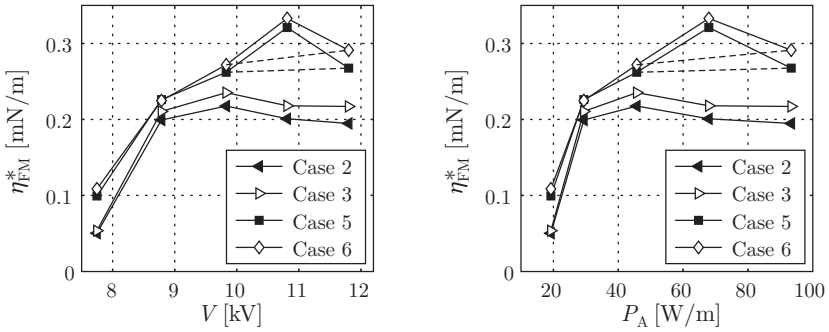

(a) $\eta^*_{\mathrm{FM}} - V$ diagram

(b) $\eta^*_{\mathrm{FM}} - P_A$ diagram

Figure 6.21: Fluid mechanic effectiveness η^*_{FM} of the plasma-actuator as a function of operating voltage V (a) and power consumption P_A (b) for the parameter range of the PIV experiments.

ing numerators F and P_A for the calculation of η^*_{FM} and η_{FM} are opposed in Figure 6.22(b). Obviously, from identical velocity data, the differential approaches determine less fluid mechanic power per determined thrust than the integral approaches do, what is apparently due to the missing shear layer in (6.24).

Finally, the concluding remark can be be derived from the above comparative discussion of coefficients, that an identification of the optimal operating point in terms of energy optimization is insufficient without clear explanations concerning the chosen quantification strategy. The example given above clearly demonstrates contradictory optimization strategies at medium power levels (say $P_A \approx 70$ W/m). Obviously, the fluid mechanic effectiveness η^*_{FM} as an evaluation basis leads to conflicting optimization efforts (reduction of the power level) as compared to an optimization based on the fluid mechanic efficiency η_{FM}. The latter coefficient in this example suggests an increase of the power level. Furthermore, a robust quantification necessarily requires a clear statement concerning the chosen determination strategy of either coefficient, i.e. based on integral or differential approaches. Therefore, it is strongly recommended to include a transparent disclosure of the underlying implemented (post-)processing procedure in publications addressing plasma-actuator optimization, insuring best possible comparability of the reports from different plasma-actuator research

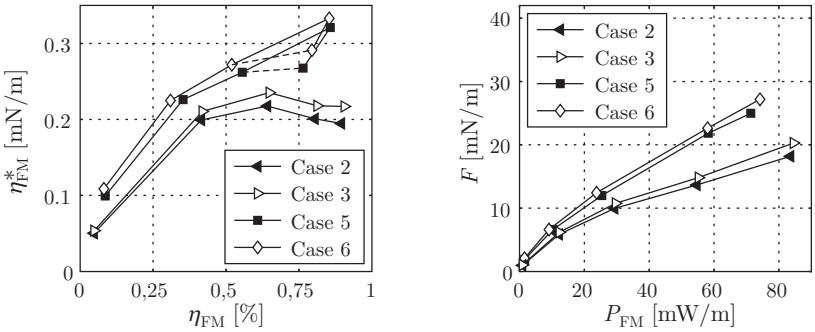

(a) $\eta^*_{\mathrm{FM}} - \eta_{\mathrm{FM}}$ diagram

(b) $F - P_{\mathrm{FM}}$ diagram

Figure 6.22: Comparison of fluid mechanic quantities: Relation of (a) fluid mechanic effectiveness η^*_{FM} and efficiency η_{FM}, (b) thrust F and fluid mechanic power P_{FM}.

groups.

7 Influence of the Airflow Conditions

Generally speaking, the airflow in context with dielectric barrier discharges is a well-established quantity. Many industrial applications of dielectric barrier discharge (ozone generation, surface treatment or pollution control) are configured such that a gas flows through the discharge domain, as comprehensively reported by Kogelschatz [115]. The observed processes are commonly characterized by the airflow rate through the precipitation or depollution reactors in combination with electrical and/or chemical quantities (see e.g. Mizuno [152, 153]). Dramane *et al.* [53], for instance, report a significant influence of the flow rate through axial and planar reactors on the transferred charge Q and the corresponding power consumption P_A. Furthermore, Jolibois *et al.* [111] present chemical measurements of discharge assisted species generation based on a so-called energy density, defined as the ratio of consumed power and the flow rate through the reactor.

Despite this broad experience with airflow-discharge interaction, reports about discharge based aerodynamic flow control commonly still neglect this interaction (cp. Section 2.2.2). The discharge intensity; hence the DBD plasma-actuator performance, is affected by numerous parameters. On the one hand, the impact of ambient conditions on the flow induced by plasma actuators has been documented extensively in many recent publications. It has been demonstrated that humidity [9, 21, 163], temperature [163, 225], ambient pressure [2, 19, 92, 213, 225, 236] and gas-species [2, 60, 76, 213], have either adverse or favorable effects on the plasma actuator's discharge intensity. On the other hand, it is commonly assumed in the flow-control community that the actuator discharge manipulates the flow but not vice-versa.

To date, only few studies have investigated the aerodynamic influence of the airflow velocity on the actuator performance. Labergue *et al.* [132, 133] report a strong variation of the discharge with changing free-stream velocities $U_\infty \leq 35$ m/s. The adverse effect of high-speed airflow (Mach number $M \leq 1.1$) on DBD patterns has been reported by Pavon *et al.* [172, 173]. Enloe *et al.* [62] recommend that the interaction of the neutral fluid with the actuator has to be taken into account, since the momentum of both quantities range in the same order of magnitude.

In this Chapter the influence of the airflow on the plasma actuator performance is characterized and quantified. Experiments were performed with velocities ranging from quiescent air ($U_\infty = 0$) up to cruise flight conditions ($M \approx 0.85$). The low and moderate velocities are relevant for take-off and approach scenarios of many aerodynamic lifting surfaces [174] and are essential for the control of unmanned aerial vehicles or internal flows. In Section 7.1 the implemented experimental procedure and parameter space is introduced, including a brief introduction of the different chosen wind tunnels. The results of various airflow impact experiments are discussed in Section 7.2. As a second degree of freedom the influence of pressure is simultaneously investigated alongside the free-stream velocity in Section 7.3. Finally, a novel online monitoring and controlling strategy is introduced in Section 7.4, demonstrating the possibility to counteract transient and fluctuating changes of the airflow conditions.

7.1 Experimental Procedure

7.1.1 Setup and Wind Tunnel Facilities

To investigate the airflow influence on the plasma-actuator performance, plasma actuators were operated in various wind tunnel experiments. The actuator performance was determined by means of simultaneous electrical and optical measurement as explained in Sections 3.1 and 4.1, where different cameras were used according to their availability. For all experiments a Nikon lens (Nikon 105 mm, AF Micro NIKKOR f/2.8D) was mounted on the cameras and the cameras were mounted outside the wind tunnels. To investigate the desired parameter range of free-stream velocities U_∞, Mach numbers M and static pressures p, three different wind tunnels were utilized for the experimentation:

NWK2 at TU Darmstadt Low-speed experiments (Exp1 - Exp4) were conducted in the Eiffel-type wind tunnel facility (NWK2) at the Technische Universität Darmstadt. This wind tunnel features a test section of 450 mm × 450 mm and is capable of producing flow speeds up to 68 m/s. Figure 7.1 gives a schematic overview of the setup.

The plasma actuator was placed on a flat plate with elliptical leading edge, which was mounted in the center of the tunnel. Using this technique the influence of the tunnel walls was eliminated and a defined boundary-layer thickness could be set according to the downstream

position of the plasma actuator. For this study the actuator was placed 400 mm downstream of the leading edge to simulate conditions as encountered during active wave cancelation (AWC) experiments of Grundmann and Tropea [96, 98]. The luminosity measurements were

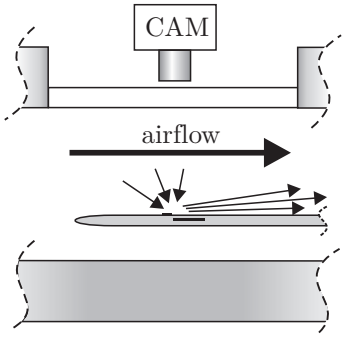

Figure 7.1: Test section of the NWK2 wind tunnel; the plasma actuator is mounted on a flat plate inside the test section.

carried out using a CCD camera (PCO SensiCam, 1376 × 1040 pixels, 12 bit, 1 fps) recording the actuator's light emission through an optical access in the ceiling of the tunnel.

TVM at TU Darmstadt High-speed experiments (Exp5 - Exp7) were conducted in the blowdown wind tunnel (TVM) of the Technische Universität Darmstadt. This wind tunnel is designed to operate at Mach numbers in the range of $0.4 < M < 4$. The dimensions of the test section are 150×150 mm^2.

In order to obtain a top-view of the plasma, the plasma actuator was mounted on the opposing window of the test section, as shown in Figure 7.2. Two different CMOS cameras were used for the experiments in the TVM. For experiment 5 a Vosskühler camera (Vosskühler1000, 1024 × 1024 pixels, 8 bit, 5 fps), for experiments 6 and 7 a Phantom camera (Phantom V12.1, 512×512 pixels, 12 bit, 24 fps) was used to record the spatio-temporal light emission of the discharge during the power consumption analysis of the operating actuator. Furthermore, the dielectric thickness of the actuator for experiment 5 was set to $d = 0.8$ mm, in order to match the dimensions chosen for the

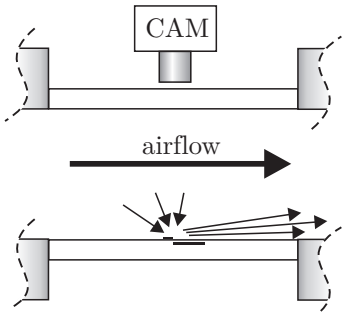

Figure 7.2: Test section of the TVM wind tunnel; the plasma actuator is mounted on the opposite window of the test section.

separation control experiments of Barckmann *et al.* [15].

HoWK at TU Dresden Low and moderate speed experiments at different pressure levels (Exp8, Exp9) were conducted in the Göttinger-type vacuum wind tunnel facility (HoWK) at the Technische Universität Dresden. The main purpose of the HoWK is the realization of density dependent calibration of hot-wire probes, as reported by Frey [82]. The nozzle of the open test section (diameter $d_N = 100$ mm) enters a vacuum chamber, where operating velocities up to $U_\infty = 100$ m/s can be achieved. This chamber can be evacuated down to re-entry conditions [82].

To eliminate the influence of the forming boundary layer, the actuator was mounted at the very tip of an acrylic plate with sharp leading edge as shown in Figure 7.3. The light emission experiments were conducted by means of a Photron camera (Photron FASTCAM MC2, 512 × 512 pixels, 8 bit, 50 fps). Additionally, for each parameter setting unscaled snapshots were taken by a Canon Camcorder (Legria HF200, HD, 1920 × 1080 pixels) to obtain qualitative color pictures of the plasma domain.

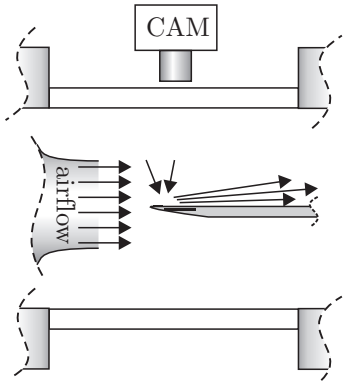

Figure 7.3: Test section of the HoWK wind tunnel; the plasma actuator is mounted at the very tip of a flat plate inside the test section.

7.1.2 Parameter Space

First, the purpose of all conducted wind-tunnel experiments are briefly introduced here to provide an overview of the parameter space. The complete list of conducted experiments is summarized in Table 7.2 on page 114 at the end of this Section.

For the first experiments (Exp1, Exp2) in the NWK2 the flow speed was increased up to 55 m/s by increments of 10 m/s (respectively 5 m/s), while operating voltage and frequency were held constant. Two different power levels were investigated. In good agreement with the reports of Labergue *et al.* [132, 133] a clear detrimental impact of the flow speed on the actuator's performance is visible. Based on this result, the influence of the performance drop to the scaling number Θ_A, as introduced in Chapter 3, had to be identified in an additional set of experiments in the NWK2. Therefore, a comparative study was carried out in quiescent air (Exp3) and at a constant flow speed of 50 m/s (Exp4), during which the electrical parameters of the actuator (operating voltage, operating frequency) have been varied systematically.

The airflow influence at higher Mach numbers has been investigated in the wind tunnel TVM. In a first experiment (Exp5) the blowdown tunnel was operated such that $M = 0.42$ at a constant static pressure $p = 1$ bar

was assured. This particular parameter setting was chosen to match the parameters of separation control experiments of Barckmann *et al.* [15]. In a second set of experiments (Exp6, Exp7) the wind tunnel was operated at constant valve position, thus generating a blowdown from initially $M = 0.85$ down to quiescent air at changing pressure levels ($p = 0.9 - 1.4$ bar). The airflow influence on the plasma-actuator performance was characterized with a novel online diagnosis approach. This diagnosis tool operates either in an online monitoring mode (Exp6) or in an online controlling mode (Exp7), where the latter automatically counteracts performance changes in-situ.

A systematic study of the combined airflow influence and pressure effects on the plasma-actuator performance was carried out by a set of experiments (Exp8, Exp9), which were conducted in the vacuum tunnel HoWK at Technische Universität Dresden. Similar to the NWK2 experiments the flow speed was increased up to 100 m/s for Exp8 (Exp9) by increments of 20 m/s (respectively 50 m/s), while operating voltage and frequency were held constant. This procedure was repeated, where the initial pressure level inside the wind tunnel of $p = 1$ bar was reduced by increments of 0.1 bar (respectively 0.05 and 0.2 bar) down to the final pressure level of $p = 0.1$ bar.

7.1.3 (Post-) Processing Strategy

Figure 7.4 shows the electrical results of Exp5 under quiescent-air conditions and at a Mach number of $M = 0.42$. At first glance, the Lissajous figure shrinks in the vertical direction but remains constant in the horizontal direction at high-speed conditions, as shown in Figure 7.4(a). Within the measurement accuracy the operating voltage V (abscissa) remains unaffected by variation of the airflow conditions, whereas the amount of transformed charge $Q = C_p V_p$ was reduced significantly. Consequently, the enclosed area of the cyclogram is smaller at high-speed conditions, which leads to a reduced power consumption P_A according to (3.5). Furthermore, the parallelism of the flatter capacitance tangents to the cyclograms demonstrates the independence of the cold capacitance C_0 from any flow conditions. This result is not surprising, since C_0 is the pure passive component of the plasma actuator functioning as a passive load in an electrical circuit (cp. Section 3.4).

In contrast, the effective discharge capacitance C_{eff} is reduced with power consumption, as qualitatively indicated by the weaker C_{eff}-slopes in Figure 7.4(a). The histogram based analysis of the capacitance time traces $C(t)$

for $M = 0$ and $M = 0.42$ are shown in Figure 7.4(b). Clearly visible,

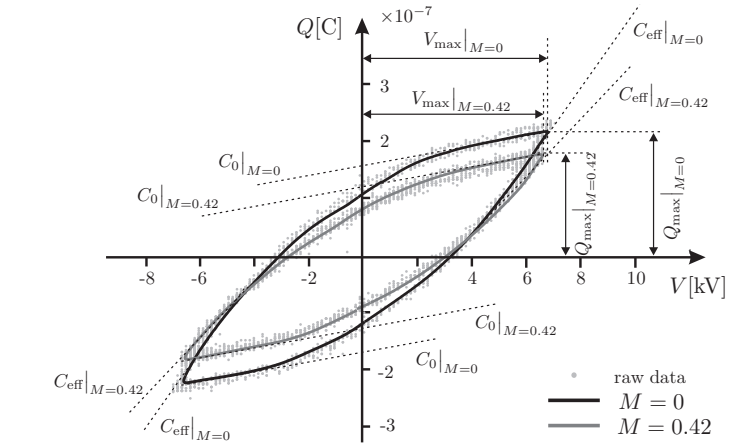

(a) Lissajous figures

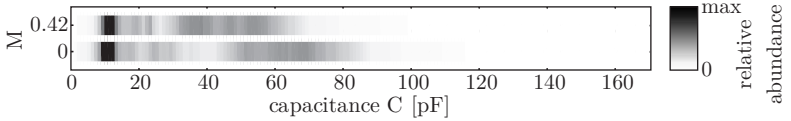

(b) capacitance histograms

Figure 7.4: Lissajous-figures and characteristic discharge quantities under quiescent air conditions and at $M = 0.42$ (Exp5) characterizing the airflow influence on the electrical discharge performance.

the effective discharge capacitance is reduced by 30%, whereas C_0 remains constant.

The Mach-number time trace $M(t)$ of Exp5 and the resulting gray value distribution of the luminosity analysis are shown in Figure 7.5, where the gray values $G(x,t)$ are plotted as a function of chord and time $G(x,t)$. The distance between the two magenta lines emphasize the strongly reduced plasma length Δx for the duration of the wind-tunnel operation. Moreover, the maximum gray value G_{peak} diminishes, which according to (4.4) weakens the peak luminosity $\widehat{G}$ for high flow velocities.

To characterize the airflow influence on the different experiments by a

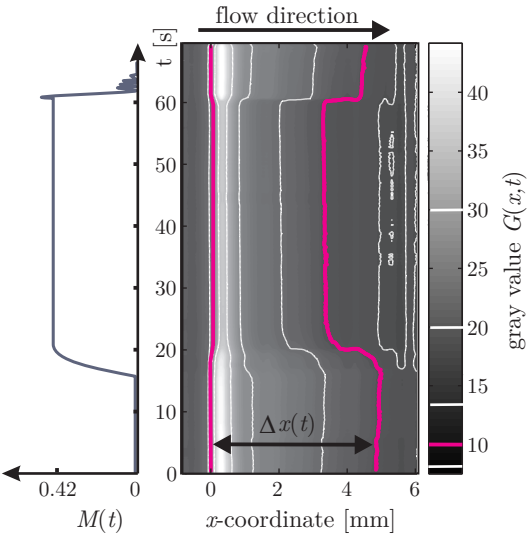

Figure 7.5: Spatio-temporal gray value distribution $G(x,t)$ of the plasma luminosity (Exp5); the wind tunnel is turned on at $t \approx 16$ s, the high-speed condition of $M = 0.42$ is fully developed at $t \approx 20$ s, at $t \approx 60$ s the wind tunnel is turned off.

key number, the relative performance

$$\Pi_\phi = \frac{\phi(M)}{\phi\big|_{M=0}} \tag{7.1}$$

and the relative performance drop

$$\Psi_\phi = 1 - \Pi_\phi = 1 - \frac{\phi(M)}{\phi\big|_{M=0}} \tag{7.2}$$

are defined. In definitions (7.1) and (7.2) ϕ appears as a general variable, which has to be exchanged by the respective quantities, i.e operating voltage V, power consumption P_A, characteristic capacitances C_0 and C_{eff}, plasma length Δx, or peak luminosity $\widehat{G}$. Both numbers Π_ϕ and Ψ_ϕ quantify performance changes due to airflow influence normalized with the quiescent-air reference value $\phi\big|_{M=0}$.

Table 7.1: Performance specific quantities under quiescent air conditions $M = 0$ and at $M = 0.42$ (Exp5).

M	V[kV]	P_A[W]	C_0[pF]	C_{eff}[pF]	Δx[mm]	$\widehat{G}$
0	13.4	18.2	9.4	61.2	5.1	3.1
0.42	12.9	12.9	9.6	39.8	3.4	2.0
Π_ϕ [%]	96.3	70.9	102.1	65.0	66.7	64.5
Ψ_ϕ [%]	3.7	29.1	-2.1	35.0	33.3	35.5

From the example results of Exp5, as listed in Table 7.1, it can be concluded that the changes of operating voltage and cold capacitance are negligible, since the deviations of Ψ_V and Ψ_{C_0} lie within the measurement accuracy. Much more salient is the performance drop of the discharge specific quantities, which exceeds 30% reduction of the electrical (Ψ_{P_A},$\Psi_{C_{\text{eff}}}$) and optical ($\Psi_{\widehat{G}}$,$\Psi_{\Delta x}$) quantities.

Table 7.2: List of conducted experiments: Chosen wind tunnel, operating conditions of actuator setup, preset airflow conditions, geometric actuator dimensions.

wind tunnel	Exp.-Nr.	operating voltage V [kV]	frequency f [kHz]	free-stream velocity U_∞ [m/s]	Mach number M	pressure p [bar]	actuator length L [mm]	electrode width [mm] w_1	w_2	dielectric thickness d [mm]
NWK2	Exp.1	8	14	0 - 55	0 - 0.16	1	0.4	2.5	10	0.4
	Exp.2	12	10	0 - 55	0 - 0.16	1	0.4	2.5	10	0.4
	Exp.3	9.8 - 12.7	8.2 - 13.4	0	0	1	0.4	2.5	10	0.4
	Exp.4	9.8 - 12.7	8.2 - 13.4	50	0.145	1	0.4	2.5	10	0.4
TVM	Exp.5*	13	8		0 - 0.42	1	0.11	2.5	10	0.8
	Exp.6	10	12		0 - 0.84	0.9 - 1.4	0.11	2.5	10	0.4
	Exp.7	10	12		0 - 0.84	0.9 - 1.4	0.11	2.5	10	0.4
HoWK	Exp.8	8.3	9	0 - 100	0 - 0.29	0.1 - 1.0	0.07	2.5	60	0.4
	Exp.9	8.3	9	0 - 100	0 - 0.29	0.1 - 1.0	0.07	2.5	60	0.4

*A preliminary version of the results of this experiment has been published alongside the separation control experiments of Barckmann *et al.* [15]. A more extensive discussion has been presented by Kriegseis *et al.* [125].

7.2 Impact of Airflow Velocity

7.2.1 Power-Consumption - Velocity Relation

For Exp1 and Exp2 the dependence of the resulting power consumption P_A on different Mach numbers M is shown in Figure 7.6. Even though the power level of Exp2 (Figure 7.6(b)) is roughly four times the power level of Exp1 (Figure 7.6(a)), the performance decreases for both experiments with increasing free-stream velocities.

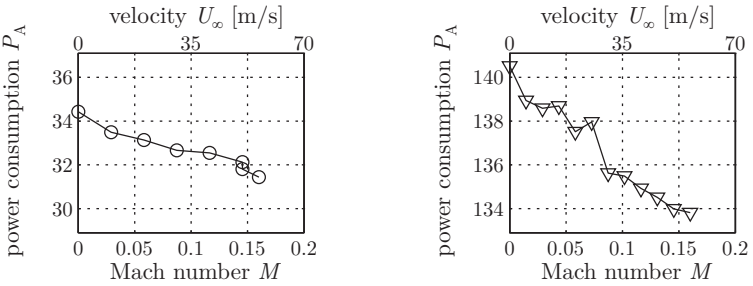

(a) Exp1 ($V = 8$ kV, $f = 14$ kHz)

(b) Exp2 ($V = 12$ kV, $f = 10$ kHz)

Figure 7.6: Power consumption of the plasma actuator as function of airflow speed; (a) Exp1, (b) Exp2.

A detailed comparison of the actuator performance under quiescent air conditions and at a free-stream velocity of $U_\infty = 50$m/s is given by the combined analysis of Exp3 and Exp4 as shown in Figure 7.7. Both experiments show the expected power-law behavior $P_A \propto V^{\frac{7}{2}}$ and $P_A \propto f^{\frac{3}{2}}$, which has been discussed in Section 3.2.2.

Furthermore, a performance drop is identified for the entire measured parameter range of Exp4 (- - -) when compared with Exp3 (——). At first glance, this proportional offset suggests that the decreasing plasma-actuator performance for increasing airflow speeds is independent of the chosen electrical operating parameters, i.e. plasma frequency f or operating voltage V. It will be demonstrated below that this independence is a simplification for advanced performance drop quantification.

However, in order to characterize this *proportional offset*, the scaling number Θ_A according to (3.8b) was calculated for Exp3 and Exp4. The results are shown in Figure 7.8, following the representation in Figure 3.8(b).

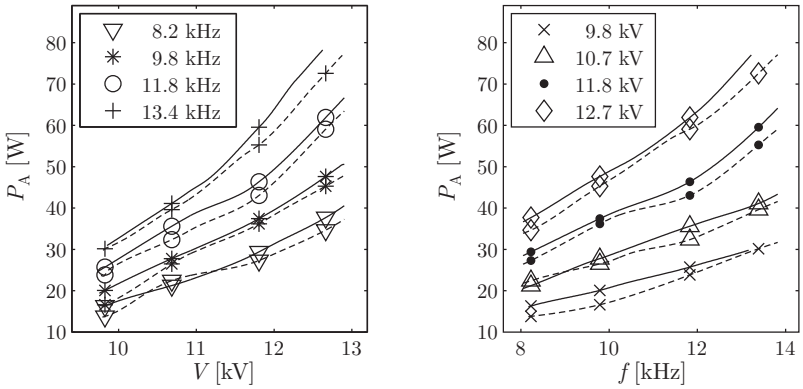

(a) $P_A - V$ diagram (b) $P_A - f$ diagram

Figure 7.7: Power consumption P_A as a function of operating voltage V (a) and frequency f(b); Exp3: $U_\infty = 0$ solid lines (——); Exp4: $U_\infty = 50$ m/s dashed lines (- - -).

Based on the Gaussian fits to the Θ_A histograms, a quantification of the offset is possible according to

$$\Pi_{\Theta_A} = \frac{\Theta_A\big|_{U_\infty=50\mathrm{m/s}}}{\Theta_A\big|_{U_\infty=0\mathrm{m/s}}} = \frac{5.13 \times 10^{-4}}{5.46 \times 10^{-4}} = 0.939. \tag{7.3}$$

The result of (7.3) demonstrates that the average plasma-actuator performance is already reduced by $\Psi_{\Theta_A} = 6\%$ for the Mach number $M = 0.15$. Note that the relative performance and its drop are identical for Θ_A and P_A according to definition (3.8b), i.e.

$$\Pi_{\Theta_A} = \Pi_{P_A} \quad \text{and} \tag{7.4a}$$
$$\Psi_{\Theta_A} = \Psi_{P_A}. \tag{7.4b}$$

To a first approximation the performance drop estimation based on Ψ_{Θ_A} is a convenient measure to estimate the airflow influence on the discharge in relation to the quiescent air performance of the plasma actuator. In the next section further influence of the chosen operating voltage V on the performance drop Ψ will be demonstrated.

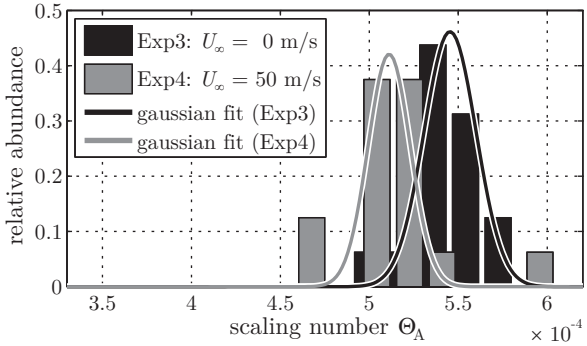

Figure 7.8: Scaling number Θ_A for free-stream velocities $U_\infty = 0$ (■ Exp3) and $U_\infty = 50$ m/s (■ Exp4).

7.2.2 Scaling Number Derivation

To gain a deeper insight into the airflow influence and the corresponding drop of quantities, the results of the relative performance Π_{P_A} are shown in Figure 7.9(a) for Exp1 and Exp2. Despite the stronger absolute power drop of Exp2 in comparison to Exp1 (cp. Figure 7.6), the decrease of the relative performance Π_{P_A} is obviously weaker for the higher applied voltages (Exp1: $V = 8$ kV, Exp2: $V = 12$ kV). The resulting curve of Exp1 demonstrates that a plasma-actuator performance drop of $\Psi_{P_A} \approx 10\%$ can occur for Mach numbers $M < 0.2$. This result becomes important, when thinking about plasma assisted stall control of UAVs, for instance, since the plasma-actuator control authority will be significantly affected by such a performance drop.

Additionally, the relative performance of Exp4 for operating voltages ranging from $9.8 - 12.7$ kV are included in the diagram, where the crosses represent the voltage-wise average of the results. The performance Π_{P_A} obviously depends on the operating voltage at a given Mach number $M = 0.145$. The experiments with higher operating voltages show a stronger resistance against airflow influences as indicated by the arrow in the diagram. This insight indicates limitations of the validity of the velocity U_∞ and corresponding Mach number M as the underlying quantities on the abscissa of performance diagrams, as introduced in Figure 7.9(a).

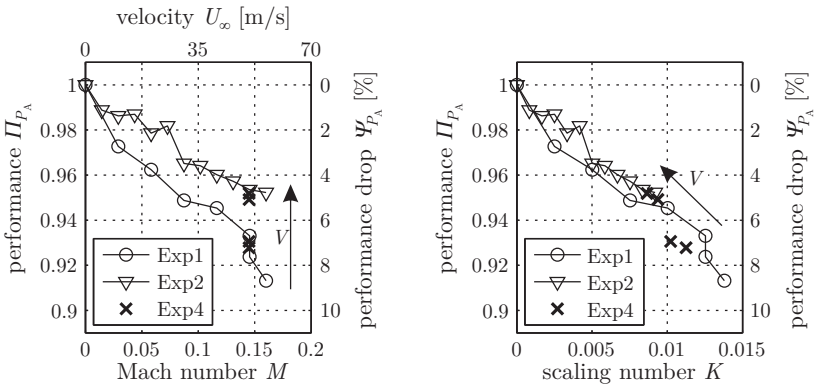

(a) $\Pi, \Psi - M, U_\infty$ diagram

(b) $\Pi, \Psi - K$ diagram

Figure 7.9: Airflow influence on the relative plasma-actuator performance Π_{P_A} and corresponding drop Ψ_{P_A} (Exp1, Exp2, Exp4); (a) as a function of free-stream velocity U_∞ and Mach number M; (b) as function of the scaling number $K = U_\infty / v_d$.

The Mach number, defined as

$$M = \frac{U_\infty}{a_\infty}, \tag{7.5}$$

compares the ratio of two characteristic external airflow quantities, i.e. the free-stream velocity U_∞ and the sonic speed a_∞.

Because of the obvious occurrence of an operating voltage dependent performance drop, it would be favorable, if M could be replaced by a modified reference number, which compensates this dependency. If this alternative reference number is denoted by K, it would be desirable to obtain constant values of $\Pi_{P_A}(K)$ and $\Psi_{P_A}(K)$ for identical K-data but differing operating voltages V.

This can be achieved by a reference number definition, where the numerator remains U_∞ as in the definition of M, but the denominator is replaced by the drift velocity $v_d = \mu E$, introduced by (2.5), of the momentum imparting ions. In this manner a discharge specific internal velocity measure of the momentum transfer procedure is established.

The resulting scaling number for the airflow influence on the plasma-actuator discharge appears as

$$K = \frac{U_\infty}{v_d}, \tag{7.6}$$

$$\text{where} \quad K \mathrel{\hat{=}} \frac{\text{external velocity}\ ^1}{\text{internal velocity}}.$$

Within the range of electric field strengths E of up to 10^7 V/m, which are relevant for operative plasma actuators, the ion mobility μ_i (defined by (2.6)) varies by only about $\pm 10\%$ and is almost the same for positive and negative ions. Therefore, an average of $\mu_i \approx 2 \times 10^{-4}$ m^2/Vs of published data [12, 16, 47, 158, 195] is chosen as constant ion mobility value for the drift velocity in (7.6).

The application of (7.6) serves as a reference value of the electric field strength E for the determination of the drift velocity. For this purpose,

$$E_0 = \frac{V}{d} \tag{7.7}$$

is used following the approaches of phenomenological plasma-actuator models (e.g. [107, 201]).

Both the operating voltage V and the dielectric thickness d are available for any conducted experiment or numerical simulation, whereas an accurate determination of the whole electric field distribution $E(x, y)$ is rather challenging for the geometry of plasma actuators. However, $E(x, y)$ scales linearly with the applied operating voltage V. For this reason E_0 according to (7.7) can be used as convenient characteristic of the operating conditions, although it overestimates the field strength of the total distribution. This overestimation appears as a constant factor for the entire range of K, and therefore, the characteristics of K are unaffected by this simplification.

The resulting curves of relative performance Π_{P_A} and corresponding performance drop Ψ_{P_A}, as a function of this novel scaling number K, are plotted in Figure 7.9(b), opposing the conventional representation of Figure 7.9(a). The former operating voltage dependent discrepancies between the experimental results of the performance drop vanish and the data fall on top of one another. Similar to Figure 7.9(a), the arrow indicates the voltage-wise orientation of the crosses representing the results of Exp4.

[1] It should be noted that alternatively the EHD number $N_{\mathrm{EHD}} = I \,/\, (w_2\, \rho\, \mu\, U_\infty^2)$ is used as a nondimensional number, when the ratio between momentum transfer and airflow inertia is the desired measure (see e.g. Moreau *et al.* [156] or Soldati and Banerjee [209]).

However, this arrow also denotes the characteristic behavior of the data along the resulting universal curve. The direct comparison of Exp1 (V = 8 kV) and Exp2 (V = 12 kV) clearly shows that the higher operating voltage not only leads to an improved performance drop resistance, but also to lower values of the scaling number K, since V appears linearly in the denominator of (7.6). Consequently, the operating voltage V corresponds to a compression parameter along the universal $\Pi - K$ curve, as indicated by the arrow of Exp4.

To verify the universality of K as characterizing scaling number for the performance drop at even higher Mach numbers, the resulting values of Π_{P_A} of Exp5 and Exp6 are plotted in Figure 7.10 together with the data already shown in Figure 7.9. The result of Exp5 exhibits a significantly steeper performance drop as compared to Exp6, although operated at a higher voltage (Exp5: $V = 13$ kV, Exp6: $V = 10$ kV, see Table 7.2[2]). The higher voltage in the case of Exp5 is compensated by a thicker dielectric (Exp5: $d = 0.8$ mm, Exp6: $d = 0.4$ mm), thus causing an even lower electric field strength.

Similar to the representation of the low-speed experiments in Figure 7.9(b), the operating voltage and/or dielectric thickness dependent discrepancies between the experimental results of the performance drop vanish and both curves collapse in Figure 7.10(b). The data of the low-speed experiments are repeated in Figure 7.10 to demonstrate the identical slope of the $\Pi - K$ curve for the entire velocity range.

Two conclusions can be drawn from the results of Figure 7.10: First, it is demonstrated that the performance drop Ψ can easily exceed 30% even at Mach numbers below 0.5, depending on the operating conditions of the plasma-actuator setup. This serious reduction of the plasma-actuator performance and corresponding control authority emphasizes that the calibration of any discharge based flow-control system (experimental or numerical!) is of limited validity without being aware of the base flow situation, since the error of the estimated plasma-actuator performance increases significantly with increasing deviation from the calibrated reference flow speed. A calibration conducted in quiescent air and used in numerical simulations results in body force source terms, which are too large or weaker than the expected control authority in the flow-control experiment.

[2]Exp6 is conducted as a blowdown experiment with varying pressure / Mach number combinations. The value shown in Figure 7.10 represents the performance drop for the characteristic time t_2, where solely the adverse velocity influence is identified under ambient pressure conditions. See Section 7.4 for more details.

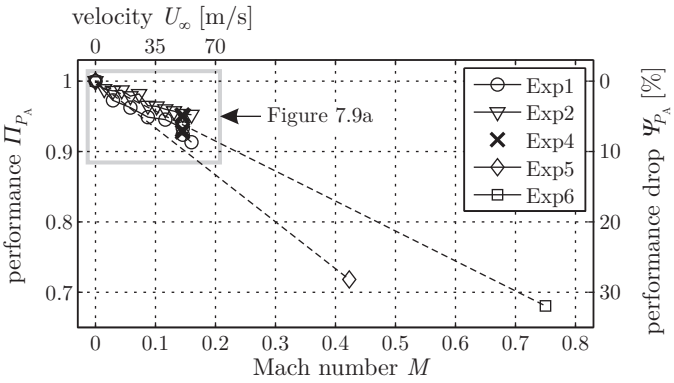

(a) $\Pi, \Psi - M, U_\infty$ diagram

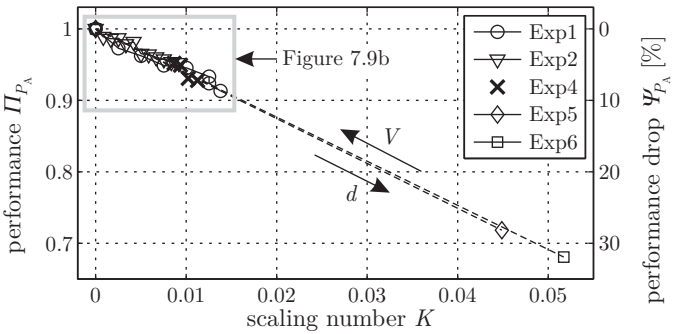

(b) $\Pi, \Psi - K$ diagram

Figure 7.10: High-speed influence on the relative plasma-actuator performance Π_{P_A} and corresponding drop Ψ_{P_A} (Exp1, Exp2, Exp4, Exp5, Exp6); (a) as a function of free-stream velocity U_∞ and Mach number M; (b) as a function of the scaling number $K = U_\infty / v_d$.

Consequently, even though it is common practice to neglect any effect of the flow on the plasma actuator, the present results demonstrate the invalidity of this assumption. Second, the limited comparability of the Mach number based performance drop analysis is resolved with the scaling number K. Representing the ratio of external and internal velocity, K characterizes the performance influence of the entire measured parameter combinations of airflow speed and electrical operating conditions on one and the same curve. The two counteracting parameters V and d appear as compression and stretching parameters for the performance drop characterization along the curve, as indicated by respective arrows in Figure 7.10(b). Therefore, this novel scaling number K is a promising basis for an improved and more universal comparison of airflow-discharge interactions.

7.2.3 Luminosity Analysis

The electrical results of Sections 7.2.1 and 7.2.2 have been cross-checked by means of the luminosity analysis, as introduced in Chapter 4. Exemplarily, the recorded gray values $G(x)$ of the discharge-light emission of Exp1 and Exp5 are shown in Figure 7.11. The corresponding gray-value isolines, as used to calculate the resulting plasma length Δx according to (4.5), are highlighted in the diagrams. Further black isolines are included in the diagrams in order to improve the readability of the gray value distribution.

Even though the reduction of the plasma length Δx is very small at Mach number $M < 0.15$, the performance drop can be identified from the local gray value maxima. Apparently, the decreasing electrical performance P_A correlates with a decreasing peak intensity $\widehat{G}$ for increasing airflow velocities.

Similar to the power-consumption quantification, as discussed in Section 7.2.1, Figure 7.12 shows a detailed comparison of the actuator's discharge peak intensity $\widehat{G}$ under quiescent air conditions (Exp3) and at a free-stream velocity of $U_\infty = 50\text{m/s}$ (Exp4), according to the representation in Figure 7.7. The aforementioned offset between the results of Exp3 and Exp4 can be identified from Figure 7.12 as well, which confirms the hypothesis that electrical performance P_A and peak intensity $\widehat{G}$ are correlating with one another.

As mentioned in Section 4.2, an achievement of quantitatively comparable results based on the peak intensity $\widehat{G}$ would require a careful calibration of the light emission measurement setup. Consequently, a quantitative comparison of $\Pi_{\widehat{G}}$ for all experiments is not immediately possible, since the gray value data presented in this Chapter was recorded with different equipment,

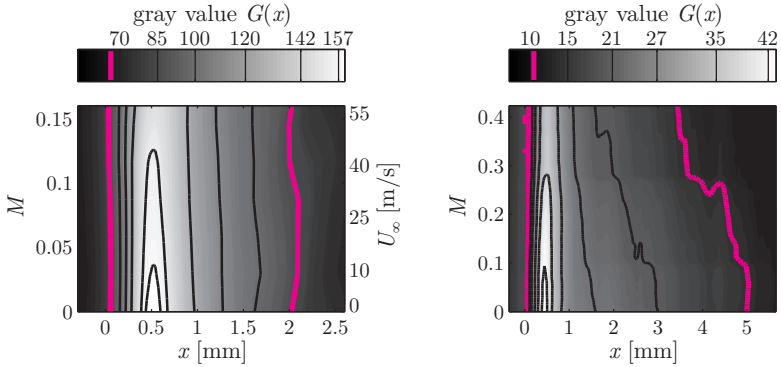

(a) Exp1: $M = 0 - 0.16$ (b) Exp5: $M = 0 - 0.42$

Figure 7.11: Gray value distribution $G(x)$ of emitted discharge light as a function of free-stream velocity U_∞ and corresponding Mach number M for Exp1 ($V = 8$ kV, $d = 0.4$ mm) and Exp5 ($V = 12$ kV, $d = 0.8$ mm); the distance between the two magenta lines corresponds the plasma length Δx.

without the required calibration. The advanced post-processing strategies presented here were developed after the measurement campaigns were completed. Nevertheless, from the comparison of Figures 7.12 and 7.7 it can be concluded that the performance drop of plasma actuators under airflow impact occurs due to the reduced discharge intensity of the operative plasma actuator.

7.3 Simultaneous Investigation of Pressure and Airflow

The close interrelation between breakdown voltage and ambient pressure is well known from the Paschen curves, as shown in Figure 2.4. Above the Stoletow point the breakdown voltage decreases with decreasing ambient pressure for a given geometry (see Section 2.1.2). Consequently, the discharge intensity changes for changing ambient pressure p at constant operating voltages V.

Abe *et al.* [1, 2] and Benard *et al.* [19, 20], for instance, report a significant increase of power consumption P_A and plasma length Δx for decreas-

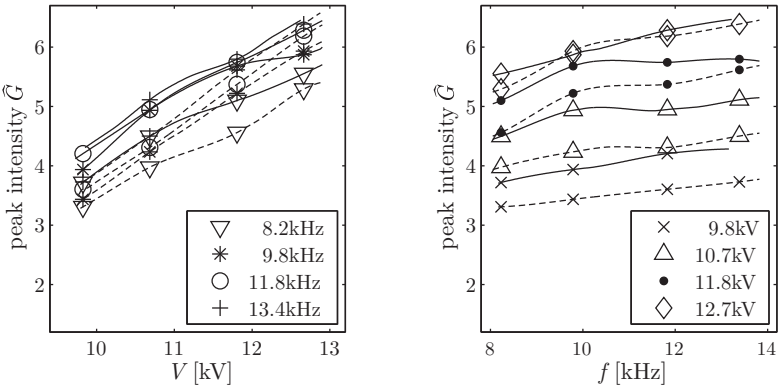

(a) $\widehat{G} - V$ diagram (b) $\widehat{G} - f$ diagram

Figure 7.12: Discharge peak intensity $\widehat{G}$ as a function of operating voltage V (a) and frequency f(b); Exp3: $U_\infty = 0$ solid lines (——); Exp4: $U_\infty = 50$ m/s dashed lines (- - -).

ing pressure levels in the range of $p = 0.2 - 1$ bar. Benard *et al.* [19, 20] furthermore identify the maximum mass flow rate of plasma-actuator wall jets at pressure levels in the range of $p = 0.4 - 0.6$ bar, which corresponds to an altitude in the range of $5 - 7$ km (cp. Benard and Moreau [22]). Abe *et al.* [1, 2] report a decreasing thrust F_t for decreasing pressure levels. This statement is in contradiction to the reports of Versailles *et al.* [225], where a decreasing body force F_b is reported for increasing pressure levels.

Pavon *et al.* [173] mention a pressure influence in combination with their airflow impact reports when changing the plasma-actuator location on an airfoil's relative chord position x/c. Based on this sensitivity of discharges to changing pressure levels, Chartier *et al.* [37] suggest an inverse application of plasma actuators as pressure sensing devices. To combine these previously reported insights of pressure sensitivity with the present knowledge about the airflow influence on the plasma-actuator performance, both parameters pressure and airflow were investigated simultaneously in the vacuum tunnel [82] of the Technische Universität Dresden.

As an introductory illustration of the parameter space, extracts of the unscaled camcorder snapshots of Exp8 and Exp9 are shown in Figures 7.13 and 7.14, respectively, representing the plasma actuator's spatial discharge distribution.

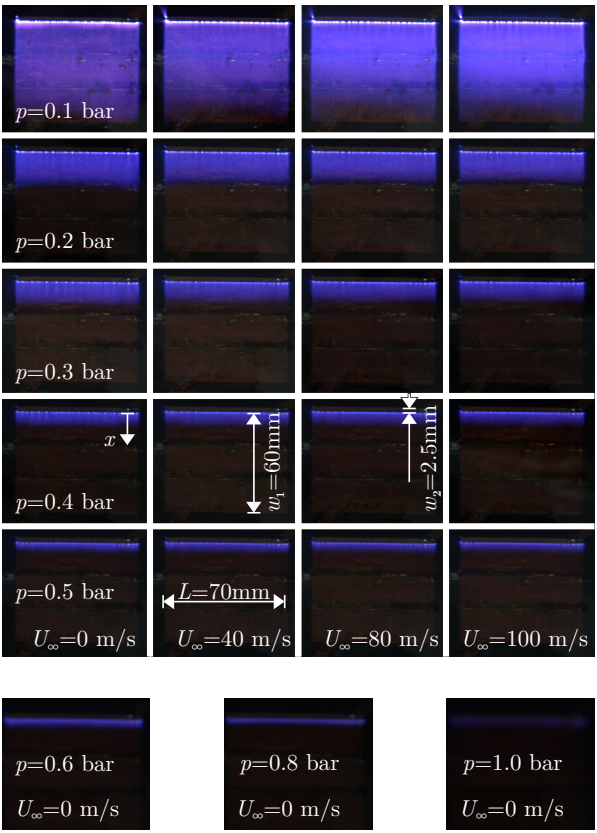

Figure 7.13: Plasma-actuator discharge distribution (Exp8); extract of unscaled camcorder snapshots; rows: constant pressure p, columns: constant airflow velocity U_∞; actuator dimensions (L, w_1, w_2) are indicated by white arrows

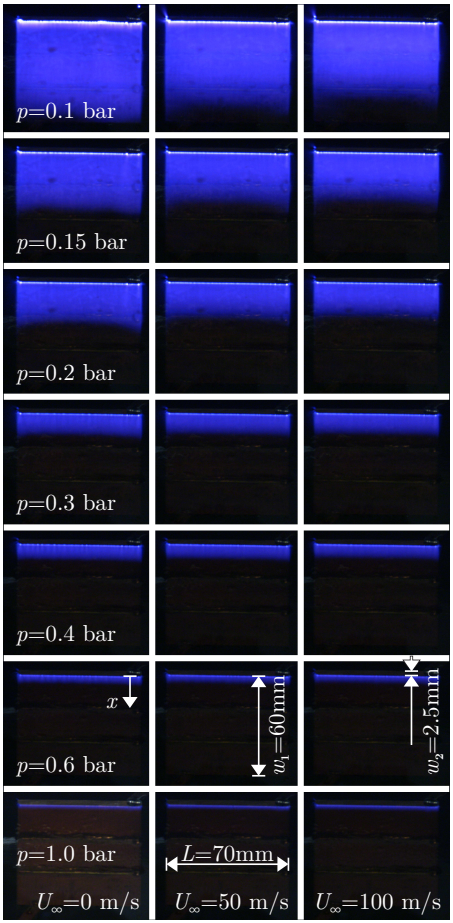

Figure 7.14: Plasma-actuator discharge distribution (Exp9); extract of unscaled camcorder snapshots; rows: constant pressure p, columns: constant airflow velocity U_∞; actuator dimensions (L, w_1, w_2) are indicated by white arrows

Identical pressure levels are displayed in rows and identical airflow velocities are orientated column-wise[3]. The quantitative results of electrical and light emission experiments are presented in Sections 7.3.1 and 7.3.2.

Similar to the published images of Abe *et al.* [1, 2] and Benard *et al.* [19, 20], the left columns of both images show the pressure influence on the discharge intensity under quiescent air condition. Obviously, the (chordwise) plasma extent increases considerably for decreasing pressure levels. Moreover, although the effect of the airflow velocity on the discharge distribution is less salient at lower pressure levels ($p = 0.1 - 0.3$ bar), the adverse influence can be recognized with the unaided eye.

7.3.1 Pressure Effects

Power consumption P_A, plasma length Δx and characteristic capacitances C_0 and C_{eff}, as obtained from Exp8 and Exp9, are plotted against the pressure p for different velocities ($U_\infty = 0 - 100$ m/s, $M = 0 - 0.29$) in a joint performance diagram in Figure 7.15. At first glance, for all quantities the set of curves of all velocities collapses to one and the same curve, which confirms the preliminary finding, that the velocity influence is considerably weaker as compared with the pressure effects. The values of either discharge specific quantity are reduced by at least one order of magnitude as the pressure level is increased by one order[4]. Note the constant values for the cold capacitance C_0 for all parameter combinations, which confirms the discharge independent pure passive component character of C_0 (cp. Section 3.4). Nevertheless, to neglect the adverse influence of the airflow with respect to the stronger pressure effect would be an invalid oversimplification as will be demonstrated in the following Section.

7.3.2 Superimposed Airflow Influence

To gain deeper insight into the airflow influence at varying pressure levels, the recorded data have to be analyzed separately for the different pressure levels. Exemplarily, the results of the data obtained from Exp8 for velocities

[3] Most images of Exp8 at higher pressure levels are not presented in Figure 7.13, since neither the pressure effect nor the airflow influence are visible with unaided eyes. Only a selection of three quiescent air results is included in the Figure for the sake of completeness.

[4] This result was expected, since it is common practice in gas discharge literature [90, 100, 182] to quantify the involved phenomena in terms of E/p, i.e. the ratio of field strength and ambient pressure. Consequently, a pressure reduction leads to the same results as an increase of the operating voltage.

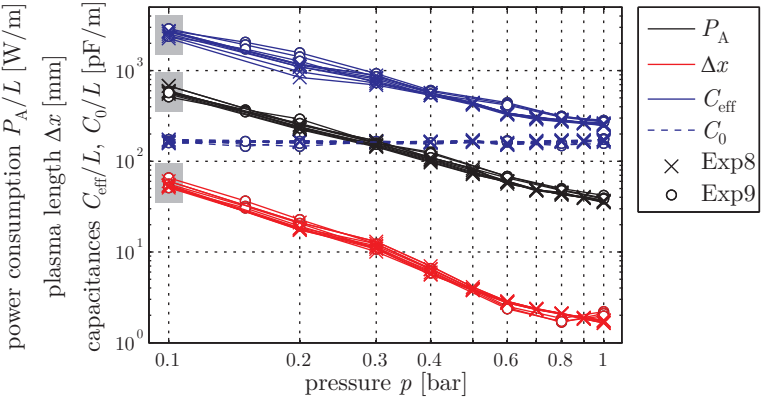

Figure 7.15: Joint performance diagram showing the results of power consumption P_A, plasma length Δx and characteristic capacitances C_0 and C_{eff} as a function of the pressure level p (Exp8, Exp9); the respective sets of curves correspond to different airflow velocities $U_\infty = 0 - 100$ m/s (■ cp. Figure 7.16).

of $U_\infty = 0 - 100$ m/s at $p = 0.1$ bar are shown in Figure 7.16, where the measured quantities P_A, Δx, C_{eff} appear on the left ordinate in the diagrams.

The accuracy of definition (7.1) for Π_ϕ depends on the quality of the quiescent-air value $\phi\big|_{M=0}$. Consequently, without further post processing any quiescent air outlier would lead to unreliable curves of relative performance. Following the findings of Section 7.2 for the lower and moderate velocity range ($M \leq 0.3$), a linear decrease of relative performance Π with increasing flow speed can be assumed. To avoid a normalization based on outliers, the regression line

$$\phi^*(M) = \phi^*\Big|_{M=0} + \beta M \tag{7.8}$$

is fit in a least-squares sense to every data set. Subsequently, all relative performances are determined according to the modified definition (7.1), i.e.

$$\overline{\Pi}_\phi = \frac{\phi(M)}{\phi^*\big|_{M=0}}, \tag{7.9}$$

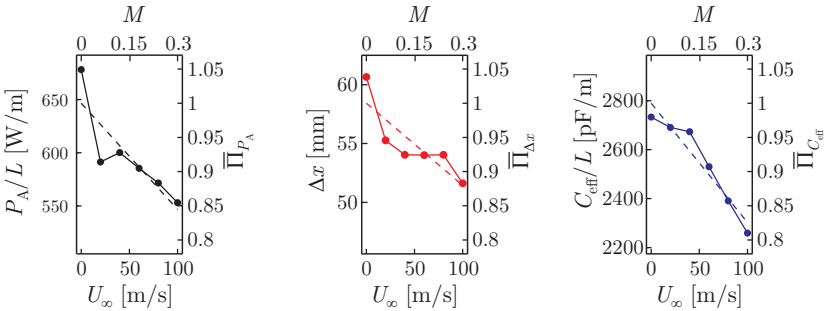

(a) power consumption (b) plasma length (c) discharge capacitance

Figure 7.16: Physical quantities ϕ and relative performance $\overline{\Pi}$ at $p = 0.1$ bar as a function of flow speed (Exp8); (a) power consumption P_A, (b) plasma length Δx, (c) discharge capacitance C_{eff}; - - - corresponding regression lines ϕ^* (respectively Π^*_ϕ).

where $\phi^*\big|_{M=0}$ is the quiescent-air value of the regression line $\phi^*(M)$. The normalized regression lines are determined according to

$$\Pi^*_\phi = \frac{\phi^*(M)}{\phi^*\big|_{M=0}} = 1 + \xi_\phi M, \tag{7.10}$$

$$\text{where} \qquad \xi_\phi = \frac{\beta}{\phi^*\big|_{M=0}} \tag{7.11}$$

is the relative slope of the performance.

The relative performances $\overline{\Pi}_\phi$ according to (7.9) are included on the right ordinates of Figure 7.16 and the normalized regression lines Π^*_ϕ are included with dashed lines in the diagrams. $\overline{\Pi}$ and the corresponding drop $\overline{\Psi} = 1 - \overline{\Pi}$ of Exp8 are shown in Figure 7.17 as function of airflow speed U_∞, M, where the different pressure levels appear in separate diagrams.

The relative error $(\overline{\Pi}_\phi - \Pi^*_\phi)/\overline{\Pi}_\phi$ of the regression-line fit is displayed in Figure 7.18 for the entire parameter space. The top, middle and bottom diagrams correspond to the power consumption P_A (black), plasma length Δx (red) and discharge capacitance C_{eff}(blue), respectively. Apart from individual outliers the error is below 3% within the measured parameter range.

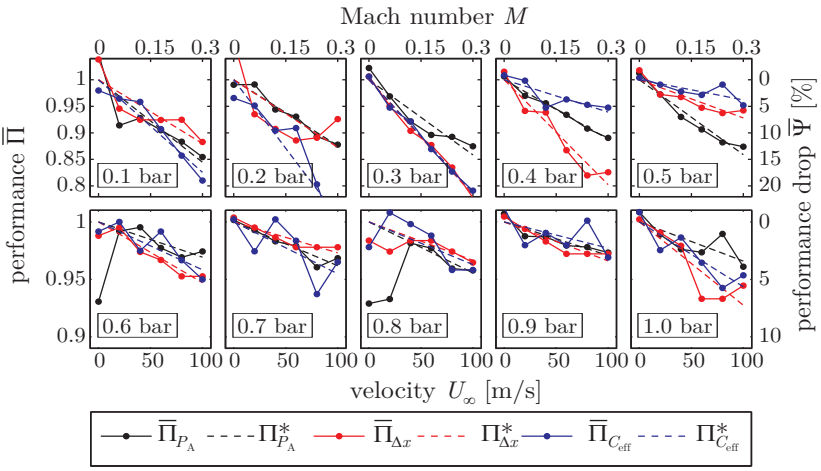

Figure 7.17: Relative performance $\overline{\Pi}_\phi$ and corresponding drop $\overline{\Psi}_\phi$ as a function of airflow speed U_∞, M for different pressure levels p (Exp8); - - - denote respective regression lines Π^*_ϕ, Ψ^*_ϕ. Note the different ordinate scales in the two rows of diagrams.

It is obvious from Figure 7.17 that the airflow impact on the discharge is not compensated by favorable pressure effects, since the relative performance drop $\overline{\Psi}$ is clearly visible. Moreover, the adverse airflow influence on the relative performance becomes more intensive at lower pressure level. This result is more clearly demonstrated by the direct comparison of the relative slopes ξ_ϕ, which are shown in Figure 7.19. The relative slopes ξ_ϕ of all quantities P_A, Δx and C_{eff}, decrease for reduced pressure levels, corresponding to a steeper decline of the relative plasma-actuator performance Π.

Despite the improved discharge intensity at lower pressure levels, the seemingly improved performance of the plasma actuators is accompanied with a more pronounced drop of the relative performance. This insight is especially important for flow-control applications with transient and/or fluctuating flow situations, as for instance different altitudes, flight velocities or shock positions in case of transsonic conditions.

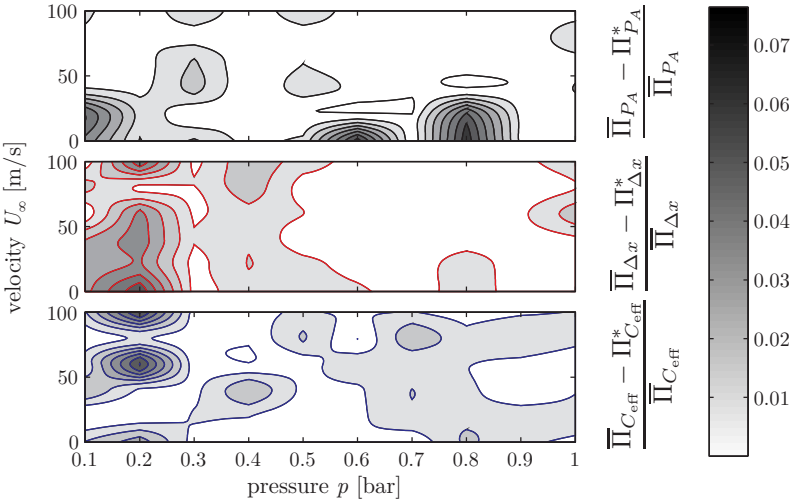

Figure 7.18: Relative error $(\overline{\Pi}_\phi - \Pi^*_\phi)/\overline{\Pi}_\phi$ for the measured parameter space of Figure 7.17; top (black): power consumption P_A, middle (red): plasma length Δx, bottom (blue): capacitance C_{eff}.

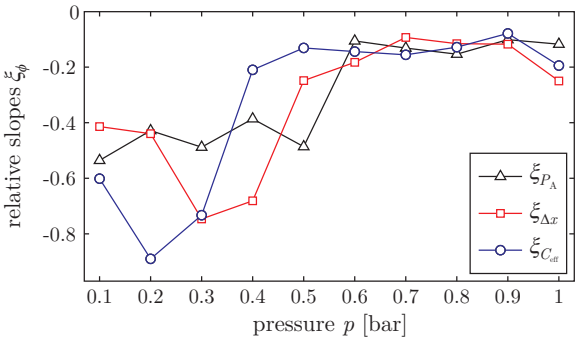

Figure 7.19: Relative slopes ξ_ϕ of the adverse airflow influence as function of the pressure level p.

Finally, it can be concluded that any advanced discharge based flow control needs to take the adverse airflow impact into account. First efforts to counteract these influences are presented in the following Section.

7.4 Online Characterization and Control

It has been demonstrated in Chapters 3-6 that the plasma-actuator performance is characterized by many closely interrelating quantities. From these interrelations conclusions have been drawn to identify the optimum operating conditions of a given plasma-actuator setup. Moreover, in Sections 7.2 and 7.3 the environmental influences (i.e. fluctuating or transient changes of state variables and/or airflow speed) on this plasma-actuator performance have been demonstrated. These influences result in a de-tuned setup of the plasma-actuator, which consequently operates at unnecessarily high energy requirements. The more important consequence is a significantly reduced control authority of the actuator as a flow-control device.

To advance beyond this retroactive performance characterization and to assure constant plasma-actuator performance, an online and in-situ evaluation of the performance is required. In a first step the performance identifying approaches have to be modified such that the required data is permanently obtained and processed to provide an online evaluation basis. Then, in a second step any identified performance changes can be counteracted in a closed-loop circuit, based on the known interrelations of the involved quantities.

Therefore, efforts have been undertaken to develop and apply such an online monitoring and controlling tool. The tool was tested by applying it to an artificial flow situation of changing pressure and Mach number. First preliminary results of these tests are reported in this Section.

7.4.1 Experimental Procedure

To implement a close-loop control of the actuator performance the existing electrical plasma-actuator setup (see Figure 3.1) had to be modified. The modified experimental procedure is sketched in Figure 7.20(a).

The electrical control circuit is built up using a computer based digital oscilloscope (Picotech PicoScope4424, 4CHs, 2500p/Ch, 10MS/s) to record the operating voltage V (Testec HVP-15HF, 1000:1) and the voltage V_p across the charge probe capacitor $C_p = 22$ nF (LeCroy PP006A, 10:1).

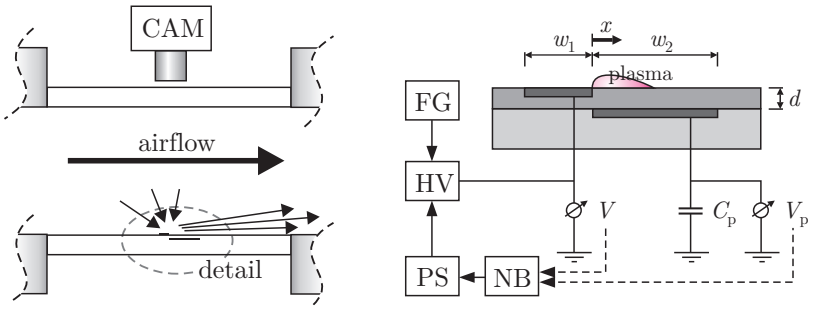

(a) TVM test section (b) detail: closed-loop circuit

Figure 7.20: Sketch of experimental setup. (a) TVM wind tunnel test section and overhead camera (CAM); (b) detailed view of electrical plasma-actuator setup and closed-loop circuit comprising function generator (FG), power supply (PS), high voltage (HV) transformer, notebook (NB) and plasma actuator.

As before, the operating voltage V was generated by a high voltage generator (GBS Elektronik, Minipuls2), which in the modified setup was driven by a laboratory power supply (Voltcraft VSP 2410) and a function generator (GW Instek, SFG-2004, fixed frequency: $f = 12.0$ kHz).

To retroactively verify the online evaluation, similar to the above experiments Exp1-5 and Exp8-9 a CMOS camera (Phantom V12.1, 512×512 pixels, 24fps; Nikon 105 mm, AF Micro NIKKOR f/2.8D) was implemented to record the spatio-temporal light emission of the discharge during the power-consumption analysis.

Reproducibly changing airflow conditions for the conducted experiments were achieved, operating the blow down wind tunnel TVM at constant valve position, thus generating a blow down from initially $M = 0.85$ down to quiescent air at changing pressure levels ($p = 0.9 - 1.4$ bar).

The resulting time traces of the state variables static and total pressure p, p_t are shown in Figure 7.21 alongside the Mach number M. In Figures 7.21 and 7.22 three characteristic times are highlighted for $p(t_1) = p_{\max}$, $p(t_2) = p_0$, $p(t_3) = p_{\min}$ with the purpose of distinguishing pressure and airspeed effects on the discharge performance. For the sake of completeness,

the interdependency of pressure and Mach number is stated, i.e.

$$\frac{p}{p_t} = \left(\frac{\gamma - 1}{2} M^2 + 1\right)^{\frac{\gamma}{1-\gamma}}, \tag{7.12}$$

where γ is the isentropic exponent of gas ($\gamma = 1.4$ for two-atomic gases).

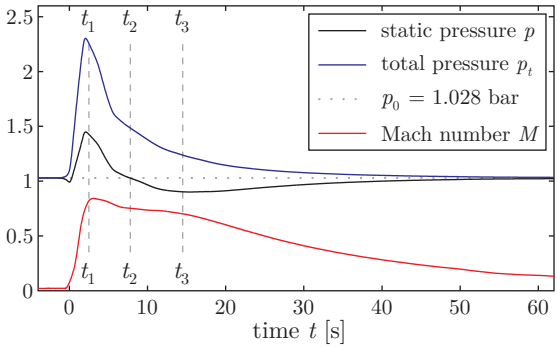

Figure 7.21: Transient flow conditions during experimentation. Time traces of static and total pressure p, p_t, Mach number M; characteristic times are labeled as t_1, t_2, t_3 (cp. Table 7.3).

Two experiments were conducted at identical flow conditions. In the first experiment (Exp6 - monitoring mode) the performance changes for a preset power consumption of $P_A^* = 7.2$ W were monitored online. In the second experiment (Exp7 - controlling mode), a simple PD control algorithm remote controlled the laboratory power supply of the electrical plasma-actuator setup, thus closing the control loop.

The recorded data of operating voltage V and probe voltage V_p were steadily forwarded from the scope to the notebook, where the online characterization was processed. The determination of the consumed power P_A for monitoring or controlling purposes occurred again from voltage-charge cyclograms, as introduced Chapter 3. According to (3.5) for every time step t^i the evaluation algorithm calculates the power consumption

$$P_A^i = f\, E^i = f \oint_{t^{i-1}}^{t^i} Q\, dV \quad \text{with} \quad Q = C_p\, V_p, \tag{7.13}$$

The computation sequence was repeated in time intervals of $\Delta t = t^i - t^{i-1} \approx 0.5$ s.

When using the diagnostic tool in closed-loop control mode, the algorithm furthermore compares P_A^i with a pre-set power level P_A^* and calculates the control signal

$$\Omega^{i+1} = \Omega^{i+1}(\Omega^i, P_A^i, P_A^*) \tag{7.14}$$

for the next time step by means of a PD control algorithm, which is then sent to the power supply (see Figure 7.20(b)). The light emission data is used to retroactively validate the online diagnostic tool by means of the temporal plasma-length evolution $\Delta x(t)$.

7.4.2 Results

The pre-set initial conditions of $f = 12$ kHz, $V = 10$ kV and $p_0 = 1.028$ bar resulted in an initial power consumption $P_A = P_A^* = 7.2$ W for $t < 0$.

In Figure 7.22(a) the results of the monitoring experiment are depicted. They clearly reveal the impact of the transient flow conditions on the actuator power P_A. Immediately after the wind tunnel valve was opened at $t = 0$ a power peak occurred due to an initial expansion wave passing the test section, which was followed by a significant performance drop ($P_A = 4.8$ W) once the blow down scenario was fully developed at t_1 under adverse pressure conditions at maximum airflow speed (see Table 7.3). At decreasing Mach number and pressure at t_2 a constantly reduced performance ($P_A = 4.9$ W) was observed, solely due to the impact of high speed airflow ($M = 0.75$) at ambient pressure conditions p_0, which agrees with the reports of Section 7.2. The influence of the minimum pressure at t_3 exceeded the adverse airflow impact ($M = 0.69$), which resulted in an increased performance $P_A = 8.7$ W as compared to the pre-set initial value $P_A^* = 7.2$ W. This augmentation is in good agreement with the reports of Abe *et al.* [1, 2] and Benard *et al.* [19, 20] and is furthermore confirmed by the observations discussed in Section 7.3. Thereafter, for $t > t_3$ all quantities asymptotically returned to their initial values again. The plasma length Δx of the simultaneously recorded light emissions further confirms the correctness of the online characterization of the power consumption.

For identical initial and airflow conditions the results of the closed-loop control experiment are shown in Figure 7.22(b). The control algorithm failed for the very strong initial power oscillation of the passing expansion wave. Thereafter the performance drop was identified at t_1 and the algorithm counteracted this drop, as shown by the slope of the control signal Ω. At $t = 5.5$ s the control algorithm collapsed for a single time step and

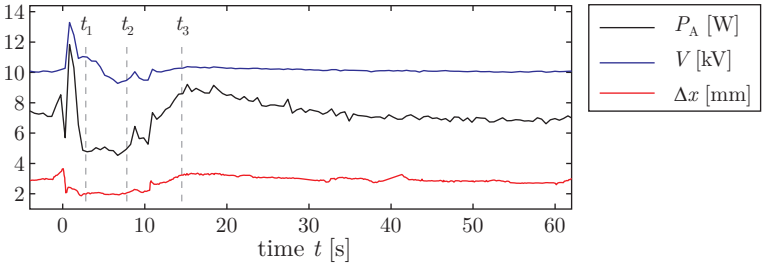

(a) monitoring mode (Exp6)

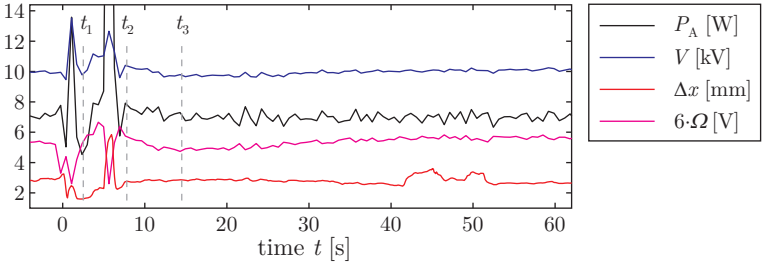

(b) controlling mode (Exp7)

Figure 7.22: Results of consumed power P_A, operating voltage V, plasma length Δx and remote-control signal Ω for (a) monitoring and (b) controlling mode of operation (cp. Table 7.3).

caused a power overshoot, due to an erratic signal. Apart from this peak the algorithm successfully conducted a closed-loop control of the power variations, which again is confirmed by the results for the plasma-length Δx. Qualitatively, the slope of the remote signal Ω of the controlled case directly mirrors the slope of the power P_A of the uncontrolled case, as demonstrated in Figure 7.23 in terms of the relative performance Π.

This direct comparison of uncontrolled performance $\Pi^m_{P_A}$ and control signal Π^c_Ω underlines the successful counteraction of the controller even in this simple proof-of-concept approach. From this result the conclusion can be drawn, that by means of steadily processed real-time performance data it is possible to achieve a constant plasma-actuator performance during operation under fluctuating and transient flow conditions. This is an important

Table 7.3: Measured data at characteristic times; ^{m} monitoring mode (Exp6), ^{c} controlling mode (Exp7); The result of Exp6 at time t_2 has already been introduced in Section 7.2; cp. Figures 7.21 and 7.22).

	p [bar]	M	P_A [W]	V [kV]	Δx [mm]	Ω [V]
$t < 0$	1.03	0	$7.2^{m,c}$	$10.0^{m,c}$	$2.9^{m,c}$	0.89^{c}
$t_1 = 2.4$ s	1.45	0.84	4.8^{m} 5.7^{c}	10.8^{m} 10.1^{c}	1.9^{m} 1.6^{c}	0.97^{c}
$t_2 = 7.8$ s	1.03	0.75	4.9^{m} 7.5^{c}	9.4^{m} 10.2^{c}	2.0^{m} 2.8^{c}	0.95^{c}
$t_3 = 14.5$ s	0.89	0.69	8.7^{m} 7.2^{c}	10.3^{m} 9.8^{c}	3.3^{m} 2.8^{c}	0.78^{c}

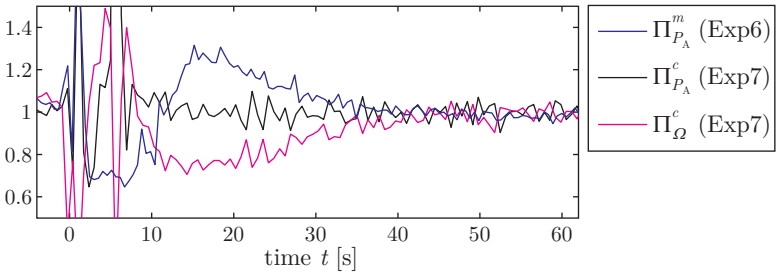

Figure 7.23: Comparison of relative performances Π_{P_A} obtained in monitoring ^{m} and controlling ^{c} mode of operation; normalized control signal Π^{c}_{Ω}.

result implying significant consequences, since beyond the common purpose of favorably manipulating the airflow, any advanced DBD-based flow control system will necessarily require an appropriate closed-loop control of the discharge device.

8 Summary and Conclusions

In the present study the requirement of improved and extended strategies to evaluate the performance of dielectric barrier discharge plasma actuators has been met. Various existing and partly well established strategies have been utilized and additional novel approaches to characterize and quantify the plasma-actuator performance have been introduced, applied and discussed extensively. Discharge specific quantities have been determined from voltage-charge cyclograms (Lissajous figures) of the gas discharge, partly in combination with light emission analysis. The momentum transfer to the air has been investigated by means of a direct method, explicitly measuring thrust and through velocity measurements. From the latter, subsequent indirect force estimation approaches have been applied based on fluid mechanic conservation equations in a comparative analysis. The environmental impact on these characteristics has been studied and the possibility of compensation of such disturbances has been outlined in an example application. The main insights and conclusions of the different investigations are recapped in the following sections.

8.1 Discharge Characterizing Quantities

In agreement with previous literature the power law $P_A \propto V^{7/2}$ is verified to be appropriate for characterizing the relation between operating voltage V and consumed actuator power P_A. However, in contradiction to previously published results, the power law $P_A \propto f^{3/2}$ has been observed for the relation of power consumption and frequency f, which was formerly assumed to be a linear relation. As a consequence of this insight, the present work demonstrates that the consumed energy per discharge cycle is indeed affected by the operating frequency.

For operation in a quiescent air environment an a priori prediction of the performance can be achieved by means of a novel scaling number Θ_A, which incorporates new insights concerning the influence of actuator size, operating voltage and frequency. For a particular configuration of the dielectric material this number has a constant value for varying operational

settings. Consequently, only one single experiment is required to determine the value for Θ_A.

The issue of power resonance interactions of the plasma actuator's discharge as an additional contribution to the load in the electrical circuit has also been studied. In order to explain these resonance changes, a new post-processing strategy is introduced, which is based on a statistical analysis of the slopes of the measured Lissajous figures. From this analysis the two characteristic capacitances C_0 and C_{eff} are extracted to quantify the geometry specific cold capacitance and the discharge specific effective capacitance of the plasma actuator, respectively.

From light-emission analysis of the discharge luminosity a close correlation between the plasma size Δx and the effective discharge capacitance C_{eff} is identified. It is therefore concluded that C_{eff} comprises the real electrode of a plasma actuator, characterized by C_0, and a discharge specific virtual electrode size enlargement, which contributes to the effective magnitude of the load by the discharge volume. Depending on the applied operating conditions, the ratio C_{eff}/C_0 exhibited values ranging between 2 and 6 for the plasma actuator materials and dimensions chosen in the present work. Moreover it proved to be very sensitive against variations of the operating conditions. Therefore, careful matching of the electrical setups for the individual application is necessary, including knowledge of the desired operating conditions. Any perfectly matched electrical circuit immediately becomes de-tuned by only changing the power level, i.e. operating voltage or frequency, which consequently leads to a reduced electrical efficiency η_{E}.

8.2 Measures for Transferred Momentum

Simultaneously performed direct actuator thrust measurement by means of a high-precision balance in combination with electrical and optical measurements revealed a close correlation between the discharge characterizing quantities P_A, C_{eff} and Δx and the resulting thrust production F_t of plasma actuators without the formerly required detailed knowledge of operating voltage V and frequency f. Consequently, a combined analysis of power consumption P_A, effective discharge capacitance C_{eff} and corresponding plasma length Δx is suggested as a powerful means to characterize, quantify and predict the DBD based thrust production for flow-control applications. In addition, the simultaneously obtained data were utilized as a benchmark for implicit estimations of thrust and body-force production

based on experimentally determined wall-jet velocity information.

Different integral and differential force-estimation approaches have been successfully applied to identical PIV-based data of plasma-actuator powered wall jets. The post-processing strategies of several research groups, each of which is available in literature, have been implemented to allow a comparison of the respective approaches for identical raw data. The variety of suggested force estimation approaches is apparently an issue of available measurement techniques and the respective simplifying assumptions for the data processing. This comparative analysis, the discussion of the corresponding simplifications and consequences for the resulting values of the actuator force F and its distribution $f(x, y)$ comprehensively reviews recent progress on the topic of force term estimation of DBD plasma actuators based on velocity-information.

It has been demonstrated that magnitude as well as the domain of the force increases with increasing operating voltages V. In agreement with previous reports about self-induced drag by Enloe *et al.* [62] the wall-shear stress is identified as playing a key role for any force estimation effort. For the observed parameter range it has been shown that 30% of the overall imparted momentum is consumed by wall friction. From this insight the conclusion must be drawn that it is of particular importance to carefully distinguish the terms induced 'actuator force F' and resulting 'actuator thrust F_t' when discussing the momentum transfer to the flow, since the imparted force remains constant downstream of the discharge domain, whereas the measured thrust decreases due to the increasing contribution of drag, as the downstream location of the chosen control volume is moved downstream. Moreover, a careful distinction between imparted momentum F and fluid mechanic power P_{FM} is essential, since the respective calculated effectiveness η^*_{FM} and efficiency η_{FM} lead to different optimization strategies, as demonstrated in a direct comparison. Due to the missing velocity information in direct thrust measurements, it is strongly recommended that both η_{FM} and η^*_{FM} are reported by research groups that characterize the momentum transfer by means of implicit velocity-based determination strategies.

A deeper insight into the spatial distribution of the plasma-actuator force is provided by two differential methods. Even though the two introduced methods contain up to third derivatives of PIV data, reasonable agreement with the results of the integral approaches is achieved. Detailed knowledge about the spatial distribution of the volume force $f(x, y)$ is essential, when modeling the plasma-actuator for numerical simulations of various flow-control scenarios. Therefore, the extracted force distributions consti-

tute a valuable step towards successful prediction of both amplitude and distribution of DBD-based volume forces for CFD applications.

The chordwise growth of the force domain with increasing operating voltage has been identified to result from a cause-effect relation between plasma presence and resulting volume force. Accordingly, a close correlation of the discharge characteristics C_{eff} and Δx and the length of the force domain Δx_F has been demonstrated. This is a valuable result, since is will improve the predictability of plasma-actuator force distributions based on simple discharge luminosity measurement.

8.3 Environmental Impact

Continuing in the direction of previous studies [133, 172] the adverse effect of the airflow on the plasma-actuator performance has been investigated. Normalization of the determined performances with the respective quiescent air results allowed a quantitative comparison of the relative performance Π and the corresponding performance drop $\Psi = 1 - \Pi$ of data performed at different power levels. It has been demonstrated that the performance drop Ψ can easily exceed 30% even at Mach numbers below 0.5, depending on the operating conditions of the plasma-actuator setup, which corresponds to a serious reduction of the plasma-actuator control authority.

In addition, it has been shown that the plasma-actuator performance is already reduced by almost 10% for Mach numbers $M < 0.2$. The identification of this drop is an important information, at least for lower velocity ranges. Obviously, it is essential to be aware of this reduction, when thinking about plasma-assisted stall control of UAVs, for instance, since 10% loss in plasma-actuator control authority will become a major issue for such flow-control scenarios. Therefore, particular care must be taken, when the calibration of any discharge based flow control device is conducted in quiescent air before it is subjected to the intended flow situation.

Furthermore, the performance drop Ψ affects the impedance of the electrical setup as well, since the effective discharge capacitance of plasma actuators is considerably affected by changing airflow velocities, which changes the size of the load in the electrical circuit. Consequently, any plasma actuator flow-control system, which has previously been impedance matched for a particular reference Mach number, can be considerably de-tuned by simply varying the free stream velocity.

Based on the velocity ratio of the airflow speed U_∞ and the ion drift v_d

a new scaling number K has been introduced. Representing the ratio of an external and an internal velocity measure of the discharge, K characterizes the performance influence of the entire measured parameter combinations of airflow speed and electrical operating conditions on one and the same curve in the $\Pi_{P_A} - K$ diagram. Consequently, this novel scaling number serves as an improved and more universal basis for the comparison of airflow-discharge interactions.

In accordance with literature [2, 19, 20] a strongly improved discharge performance has been observed at reduced pressure levels p. Despite this favorable effect, a more pronounced drop Ψ_{P_A} of the relative performance Π_{P_A} has been shown for lower pressure levels. This finding is especially important for flow-control applications, in which the pressure distribution around the airfoil entirely changes with changing altitude of the aerial vehicle or locally fluctuates due to oscillating shock positions and flow detachment relevant for buffet and stall control application, respectively.

From observed environmental influences it is therefore concluded that the calibration of any discharge based flow-control system (experimental or numerical!) is of limited validity without being aware of the base flow situation, since the error of the estimated plasma-actuator performance increases significantly with increasing deviation from the calibrated reference flow speed. A calibration conducted in quiescent air and used in numerical simulations results in either body-force source terms which are too large or a weaker than expected control authority in the flow-control experiment. Even though it is common practice to neglect any effect of the flow on the plasma actuator, the present work has demonstrated the invalidity of this assumption.

In a first proof of concept it has successfully been demonstrated that close-loop control of the electric circuit can assure a constant plasma-actuator performance over a wide range of Mach numbers M and varying pressure levels. This is an important result implying significant consequences, since beyond the common purpose of favorably manipulating the airflow, any advanced DBD based flow-control system will necessarily require an appropriate closed-loop control of the discharge device.

8.4 Concluding Remarks

The present work is the attempt to provide guidelines how to characterize and quantify the performance of dielectric barrier discharge plasma actuators for aerodynamic flow-control applications. An efficiency chain of the

plasma actuator in terms of power-flow diagram from the energy source to the flow-control success has been sketched, serving as an outline throughout the study. Existing characteristics have been verified and several new quantities and scaling numbers have been introduced and discussed extensively. A final link in evaluating how efficient an actuator is in achieving its goal concerns the actual effect on the overall flow manipulation, e.g. transition, separation or circulation control. This final link has to be investigated specifically for each individual application, since each flow-control purpose has its own guideline to characterize and quantify flow-control success, corresponding to different definitions of power saving and saving rate.

It is recommended for future research efforts to systematically investigate the influence of dielectric thickness and permittivity and the resulting C_0 on the scaling number Θ_A, since it is assumed that Θ_A is a function of C_0. A combination of both characteristics would result in one universal scaling number for plasma-actuator characterization, incorporating information of the discharge state and the material properties. It is presumed that most limitations of comparability and predictability of the plasma-actuator performance will vanish by the application of such a number.

Finally, it is hoped that the present study is a helpful contribution to an improved characterization, documentation and prediction of discharge-based flow control in aerodynamic applications.

Bibliography

[1] T. Abe, Y. Takizawa, and S. Sato. A Parametric Experimental Study for Momentum Transfer by Plasma Actuator. In *AIAA 2007-185; 45th AIAA Aerospace Sciences Meeting and Exhibit, Reno, Nevada, USA*, 2007.

[2] T. Abe, Y. Takizawa, and S. Sato. Experimental Study for Momentum Transfer in a Dielectric Barrier Discharge Plasma Actuator. *AIAA Journal*, 46(9):2248–2256, 2008.

[3] R. J. Adrian. Particle-imaging techniques for experimental fluid mechanics. *Annual Review of Fluid Mechanics*, 23:261–304, 1991.

[4] R. J. Adrian. Twenty years of particle image velocimetry. *Experiments in Fluids*, 39:159–169, 2005.

[5] T. Albrecht, R. Grundmann, G. Mutschke, and G. Gerbeth. On the stability of the boundary layer subject to a wall-parallel Lorentz force. *Physics of Fluids*, 18(9):098103–+, Sept. 2006.

[6] T. Albrecht, T. Weier, G. Gerbeth, H. Metzkes, and J. Stiller. A method to estimate the planar, instantaneous body force distribution from velocity field measurements. *Physics of Fluids*, 23(2):021702, 2011.

[7] K. Allégraud. *Plasma pour la dépollution.* PhD thesis, École Polytechnique, Palaiseau, 2008.

[8] K. Allégraud, O. Guaïtella, and A. Rousseau. Spatio-temporal breakdown in surface DBDs: evidence of collective effect. *Journal of Physics D: Applied Physics*, 40(24):7698, 2007.

[9] R. Anderson and S. Roy. Preliminary Experiments of Barrier Discharge Plasma Actuators using Dry and Humid Air. In *AIAA 2006-0369; 44th AIAA Aerospace Sciences Meeting and Exhibit, Reno, Nevada, USA*, 2006.

[10] T. Andrews and P. G. Tait. On the volumetric relations of ozone, and the action of the electrical discharge on oxygen and other gases. *Philosophical Transactions of the Royal Society of London*, 150:113–131, 1860.

[11] R. Aris. *Vectors, tensors, and the basic equations of fluid mechanics*. Englewood Cliffs, N.J., Prentice-Hall, 1962.

[12] K. Asano, T. Ajima, and Y. Higashiyama. The measurement of ion mobility by using an axisymmetric ion-flow anemometer. *Industry Applications Conference, 1995. Thirtieth IAS Annual Meeting, IAS '95., Conference Record of the 1995 IEEE*, 2:1206 –1210 vol.2, oct 1995.

[13] C. Baird, C. L. Enloe, T. E. McLaughlin, and J. W. Baughn. Acoustic testing of the dielectric barrier discharge (dbd) plasma actuator. In *AIAA 2005-565; 43rd AIAA Aerospace Sciences Meeting and Exhibit, Reno, Nevada, USA*, 2005.

[14] N. Balcon, N. Bénard, Y. Lagmich, J.-P. Boeuf, G. Touchard, and E. Moreau. Positive and negative sawtooth signals applied to a DBD plasma actuator - influence on the electric wind. *Journal of Electrostatics*, 67(2-3):140 – 145, 2009.

[15] K. Barckmann, J. Kriegseis, S. Grundmann, and C. Tropea. Dielectric-Barrier Discharge Plasmas for Flow Control at Higher Mach Numbers. In *AIAA 2010-4258; 5th Flow Control Conference, Chicago, Illinois, USA*, 2010.

[16] J. Bartels, P. T. Bruggencate, H. Hausen, K. H. Hellwege, K. Schäfer, and E. Schmidt. Teil 3: Elektrotechnik - Lichttechnik - Röntgentechnik. In *Landolt-Börnstein. Zahlenwerte und Funktionen aus Physik, Chemie, Astronomie, Geophysik und Technik.*, volume 4. Springer Berlin-Göttingen-Heidelberg, 6. edition, 1957.

[17] J. W. Baughn, C. O. Porter, B. L. Peterson, T. E. McLaughlin, C. L. Enloe, G. I. Font, and C. Baird. Momentum Transfer for an Aerodynamic Plasma Actuator with an Imposed Boundary Layer. In *AIAA 2006-166; 44th AIAA Aerospace Sciences Meeting and Exhibit, Reno, Nevada, USA*, 2006.

[18] K. Becker, U. Kogelschatz, H. Schoenbach, and R. Barker, editors. *Non-Equilibrium Air Plasmas at Atmospheric Pressure*. Inst of Physics Pub, 2005.

[19] N. Bénard, N. Balcon, and E. Moreau. Electric Wind Produced by a Single Dielectric Barrier Discharge Actuator Operating in Atmospheric Flight Conditions - Pressure Outcome. In *AIAA 2008-3792; 39th Plasmadynamics and Lasers Conference, Seattle, Washington, USA*, 2008.

[20] N. Bénard, N. Balcon, and E. Moreau. Electric wind produced by a surface dielectric barrier discharge operating in air at different pressures: aeronautical control insights. *Journal of Physics D: Applied Physics*, 41(4):042002 (5pp), 2008.

[21] N. Bénard, N. Balcon, and E. Moreau. Electric Wind Produced by a Surface Dielectric Barrier Discharge Operating Over a Wide Range of Relative Humidity. In *AIAA 2009-488; 47th AIAA Aerospace Sciences Meeting, Orlando, Florida, USA*, 2009.

[22] N. Bénard and E. Moreau. Effects of Altitude on the Electromechanical Characteristics of a Single Dielectric Barrier Discharge Plasma Actuator. In *AIAA 2010-4633; 41st Plasmadynamics and Lasers Conference, Chicago, Illinois, USA*, 2010.

[23] N. Bénard and E. Moreau. On the Vortex Dynamic of Airflow Reattachment Forced by a Single Non-thermal Plasma Discharge Actuator. *Flow, Turbulence and Combustion*, 87:1–31, 2011.

[24] N. Bénard, E. Moreau, J. Griffin, and L. N. Cattafesta III. Plasma Flow Control Ű Autonomous Lift Improvement by Slope-Seeking. In *AIAA 2009-4182; 39th AIAA Fluid Dynamics Conference; San Antonio, Texas, USA*, 2009.

[25] J. P. Boeuf. Applications and modeling of non-equilibrium plasmas. In *Mathematical Modeling and Computational Challenges in Plasma Physics*, 2004.

[26] J. P. Boeuf, Y. Lagmich, T. Challegari, and L. Pitchford. Electrohydrodynamic force and acceleration in surfaces discharges. In *AIAA 2006-3574; 37th AIAA Plasmadynamics and Lasers Conference, San Francisco, California, USA*, 2006.

[27] J. P. Boeuf, Y. Lagmich, and L. C. Pitchford. Contribution of positive and negative ions to the electrohydrodynamic force in a dielectric barrier discharge plasma actuator operating in air. *Journal of Applied Physics*, 106(2):023115, 2009.

[28] J. P. Boeuf, Y. Lagmich, T. Unfer, T. Callegari, and L. C. Pitchford. Electrohydrodynamic force in dielectric barrier discharge plasma actuators. *Journal of Physics D: Applied Physics*, 40:652–662, Feb. 2007.

[29] J. P. Boeuf and L. Pitchford. Electrohydrodynamic force and aerodynamic flow acceleration in surface dielectric barrier discharge. *Journal of Applied Physics*, 97:103307, 2005.

[30] A. Bogaerts, E. Neyts, R. Gijbels, and J. van der Mullen. Gas discharge plasmas and their applications. *Spectrochimica Acta Part B: Atomic Spectroscopy*, 57(4):609 – 658, 2002.

[31] G. Borcia, C. A. Anderson, and N. M. D. Brown. Dielectric Barrier Discharge for Surface Treatment: Application to Selected Polymers in Film and Fibre Form. *Plasma Sources Science and Technology*, 12(3):335–344, 2003.

[32] V. Boucinha, R. Joussot, P. Magnier, R. Weber, and A. Leroy-Chesneau. Characterization of the Ionic Wind Produced by a DBD Actuator Designed to Control the Laminar-to-Turbulent Transition. In *14th Int Symp on Applications of Laser Techniques to Fluid Mechanics*, 2008.

[33] N. S. J. Braithwaite. Introduction to gas discharges. *Plasma Sources Science and Technology*, 9(4):517–527, 2000.

[34] S. C. Brown. *Introduction to electrical discharges in gases.* John Wiley & Sons, 1966.

[35] A. R. Byerley, T. E. McLaughlin, and R. D. Van Dyken. Using a Plasma Actuator to Control Laminar Separation on a Linear Cascade Trubine Blade. In *AIAA 2003-1026; 41st AIAA Aerospace Sciences Meeting, Reno, Nevada, USA*, 2003.

[36] L. N. Cattafesta and M. Sheplak. Actuators for Active Flow Control. *Annual Review of Fluid Mechanics*, 43:247–272, 2011.

[37] B. J. Chartier, M. Arjomandi, and C. B. S. An Investigation on the Application of DBD Plasma Actuators as Pressure Sensors. In *AIAA 2009-651;47th AIAA Aerospace Sciences Meeting, Orlando, Florida, USA*, 2009.

[38] Z. Chen. Impedance Matching for One Atmosphere Uniform Glow Discharge Plasma (OAUGDP) Reactors. *IEEE Transaction on Plasma Science*, 30(5):1922 – 1930, 2002.

[39] Z. Chen. *Impedance Matching and PSpice Simulation of One Atmosphere Uniform Glow Discharge Plasma (OAUGDP) Reactor/Actuator Systems*. PhD thesis, The University of Tennessee, Knoxville, 2007.

[40] J. H. Choi, T. I. Lee, I. Han, H. K. Baik, K. M. Song, Y. S. Lim, and E. S. Lee. Investigation of the transition between glow and streamer discharges in atmospheric air. *Plasma Sources Science and Technology*, 15(3):416, 2006.

[41] L. G. Christophorou and J. K. Olthoff. *Fundamental Electron Interactions with Plasma Processing Gases*. Physics of Atoms and Molecules. Kluwer Academic / Plenum Publishers, 2004.

[42] J. J. Coogan. Pathogen control in complex fluids with water-coupled excimer lamps at 282 and 308 nm. *Photochemistry and Photobiology*, 81:1511–1517, 2005.

[43] T. C. Corke, C. L. Enloe, and S. P. Wilkinson. Dielectric barrier discharge plasma actuators for flow control. *Annual Review of Fluid Mechanics*, 42(1):505–529, 2010.

[44] T. C. Corke, E. J. Jumper, M. L. Post, D. Orlov, and T. E. McLaughlin. Application of Weakly-Ionized Plasmas as Wing Flow-Control Devices. In *AIAA 2002-0350;*, 2002.

[45] T. C. Corke, M. L. Post, and D. M. Orlov. SDBD Plasma Enhanced Aerodynamics: Concepts, Optimization and Applications. *Progress in Aerospace Sciences*, 43:193–217, 2007.

[46] T. C. Corke, M. L. Post, and D. M. Orlov. Single Dielectric Barrier Discharge Plasma Enhanced Aerodynamics: Physics, Modeling and Applications. *Experiments in Fluids*, 46:1–26, 2009.

[47] J. Cross. *Electrostatics: Principles, Problems and Applications*. Institute of Physics Publishing, 1987.

[48] J. O. Dabiri. On the estimation of swimming and flying forces from wake measurements. *Journal of Experimental Biology*, 208:3519–3532, 2005.

[49] J. Dedrick, R. W. Boswell, P. Audier, H. Rabat, D. Hong, and C. Charles. Plasma propagation of a 13.56 MHz asymmetric surface barrier discharge in atmospheric pressure air. *Journal of Physics D: Applied Physics*, 44(20):205202, 2011.

[50] F. Delobeau. *The environment of the earth*. Reidel, 1972.

[51] P. Donald, Rizzetta, and M. R. Visbal. Numerical Investigation of Plasma-Based Flow Control for a Transitional Highly-Loaded Low-Pressure Turbine. In *AIAA 2007-938; 45th AIAA Aerospace Sciences Meeting and Exhibit, Reno, Nevada, USA*, 2007.

[52] B. Dong, J. M. Bauchire, J. M. Pouvesle, P. Magnier, and D. Hong. Experimental Study of a DBD Surface Discharge for the Active Control of Subsonic Airflow. *Journal of Physics D: Applied Physics*, 41(15):155201 (9pp), 2008.

[53] B. Dramane, N. Zouzou, E. Moreau, and G. Touchard. Characterization of a dielectric barrier discharge in axisymmetric and planar configurations -electrical properties-. *International Journal of Plasma Environmental Science and Technology*, 2:89–94, 2008.

[54] M. J. Druyvesteyn and F. M. Penning. The mechanism of electrical discharges in gases of low pressure. *Reviews of Modern Physics*, 12(2):87–174, Apr 1940.

[55] M. J. Druyvesteyn and F. M. Penning. Errata: Mechanism of electrical discharges in gases of low pressure. *Reviews of Modern Physics*, 13(1):72–73, Jan 1941.

[56] A. Duchmann, J. Kriegseis, S. Grundmann, and C. Tropea. Customizing DBD Actuators for Flow-Control Applications using PIV. In *8th International Symposium on Particle Image Velocimetry, Melbourne, Australia*, 2009.

[57] R. Durscher and S. Roy. Novel Multi-Barrier Plasma Actuators for Increased Thrust. In *AIAA 2010-965; 48th AIAA Aerospace Sciences Meeting Including the New Horizons Forum and Aerospace Exposition, Orlando, Florida, USA*, 2010.

[58] R. Durscher and S. Roy. Force Measurement Techniques and Preliminary Results Using Aerogels and Ferroelectrics for Dielectric Barrier Discharge Actuators. In *AIAA 2011-3735; 42nd AIAA Plasmadynamics and Lasers Conference, Honolulu, Hawaii, USA*, 2011.

[59] B. Eliasson and U. Kogelschatz. Modeling and applications of silent discharge plasmas. *IEEE Transactions on Plasma Science*, 19:309–323, 1991.

[60] C. Enloe, J. Baughn, G. Font, and T. McLaughlin. Parameterization of Temporal Structure in the Single-Dielectric-Barrier Aerodynamic Plasma Actuator. *AIAA Journal*, 44:1127–1136, 2006.

[61] C. L. Enloe, G. I. Font, T. E. McLaughlin, and D. M. Orlov. Surface Potential and Longitudinal Electric Field Measurements in the Aerodynamic Plasma Actuator. *AIAA Journal*, 46:2730–2740, 2008.

[62] C. L. Enloe, M. G. McHarg, G. I. Font, and T. E. McLaughlin. Plasma-Induced Force and Self-Induced Drag in the Dielectric Barrier Discharge Aerodynamic Plasma Actuator. In *AIAA-2009-1622; 47th AIAA Aerospace Sciences Meeting, Orlando, Florida, USA*, 2009.

[63] C. L. Enloe, M. G. McHarg, and T. E. McLaughlin. Time-correlated force production measurements of the dielectric barrier discharge plasma aerodynamic actuator. *Journal of Applied Physics*, 103(7):073302–+, 2008.

[64] C. L. Enloe, G. J. W. McLaughlin, T. E., R. A. Medina, and W. S. Miller. Surface Potential and Electric Field Sturcture in the Areodynamic Plasma Actuator. In *AIAA 2008-1103; 46th AIAA Aerospace Sciences Meeting and Exhibit, Reno, Nevada, USA*, 2008.

[65] C. L. Enloe, T. E. McLaughlin, G. I. Font, and J. W. Baughn. Parameterization of Temporal Structure in the Single Dielectric Barrier Aerodynamic Plasma Actuator. In *AIAA 2005-0564*, 2005.

[66] C. L. Enloe, T. E. McLaughlin, G. I. Font, and J. W. Baughn. Frequency Effects on the Efficiency of the Aerodynamic Plasma Actuator. In *AIAA 2006-166; 44th AIAA Aerospace Sciences Meeting and Exhibit, Reno, Nevada, USA*, 2006.

[67] C. L. Enloe, T. E. McLaughlin, R. D. VanDyken, and J. C. Fischer. Plasma Structure in the Aerodynamic Plasma Actuator. In *AIAA-2004-0844; 42nd AIAA Aerospace Sciences Meeting and Exhibit, Reno, Nevada, USA*, 2004.

[68] C. L. Enloe, T. E. McLaughlin, R. D. VanDyken, K. D. Kachner, E. J. Jumper, and T. C. Corke. Mechanisms and Responses of a Single Dielectric Barrier Plasma Actuator: Plasma Morphology. *AIAA Journal*, 42(3):589–594, 2004.

[69] C. L. Enloe, T. E. McLaughlin, R. D. VanDyken, K. D. Kachner, E. J. Jumper, T. C. Corke, M. Post, and O. Haddad. Mechanisms and Responses of a Single Dielectric Barrier Plasma Actuator: Geometric Effects. *AIAA Journal*, 42(3):595–604, 2004.

[70] Z. Falkenstein and J. J. Coogan. Microdischarge Behaviour in the Silent Discharge of Nitrogen - Oxygen and Water - Air Mixtures. *Journal of Physics D: Applied Physics*, 30(5):817–825, 1997.

[71] J. W. Ferry and L. Rovey. Thrust Measurement of Dielectric Barrier Discharge Plasma Actuators and Power Requirements for Aerodynamic Control. In *AIAA 2010-4982; 5th Flow Control Conference, Chicago, Illinois, USA*, 2010.

[72] S. Flügge, editor. *Encyclopedia of Physics*, volume Volume 21: Electron-Emission / Gas Discharges 1. Springer, 1956.

[73] S. Flügge, editor. *Encyclopedia of Physics*, volume Volume 22: Gas Discharges 2. Springer, 1956.

[74] G. I. Font, C. L. Enloe, and T. E. McLaughlin. Effect of Volumetric Momentum Addition on the Total Force Production of a Plasma Actuator. In *AIAA 2009-4285; 39th AIAA Fluid Dynamics Conference, San Antonio, Texas, USA*, 2009.

[75] G. I. Font, C. L. Enloe, and T. E. McLaughlin. Plasma Volumetric Effects on the Force Production of a Plasma Actuator. *AIAA Journal*, 48:1869–1874, 2010.

[76] G. I. Font, C. L. Enloe, J. Y. Newcomb, A. L. Teague, A. R. Vasso, and T. E. McLaughlin. Effects of Oxygen Content on the Behavior of the Dielectric Barrier Discharge Aerodynamic Plasma Actuator. In *AIAA 2010-545; 48th AIAA Aerospace Sciences Meeting, Orlando, Florida, USA*, 2010.

[77] G. I. Font and W. L. Morgan. Plasma Discharges in Atmospheric Pressure Oxygen for Boundary Layer Separation Control. In *AIAA 2005-4632; 35th AIAA Fluid Dynamics Conference and Exhibit, Toronto, Ontario, Canada*, 2005.

[78] M. Forte, J. Jolibois, E. Moreau, G. Touchard, and M. Cazalens. Optimization of a Dielectric Barrier Discharge Actuator by Stationary and Non-stationary Measurements of the Induced Flow Velocity - Application to Airflow Control. In *AIAA 2006-2863; 3rd AIAA Flow Control Conference, San Francisco, California, USA*, 2006.

[79] M. Forte, J. Jolibois, J. Pons, E. Moreau, G. Touchard, and M. Cazalens. Optimization of a Dielectric Barrier Discharge Actuator by Stationary and Non-Stationary Measurements of the Induced Flow Velocity: Application to Airflow Control. *Experiments in Fluids*, 43:917–928, 2007.

[80] G. Francis. The glow discharge at low pressure. In S. Flügge, editor, *Encyclopedia of Physics*, volume Volume 22: Gas Discharges 2, pages 53–61. Springer, 1956.

[81] K.-P. Francke, R. Rudolph, and H. Miessner. Design and operating characteristics of a simple and reliable dbd reactor for use with atmospheric air. *Plasma Chemistry and Plasma Processing*, 23:47–57, 2003.

[82] J. Frey. Dichteabhängige Kalibrierung von Hitzdrahtsonden im Strömungskanal für verdünnte Gase ("Höhenwindkanal"). Technical report, TU Dresden, 2011.

[83] A. Fridman, A. Chirokov, and A. Gutsol. Non-thermal atmospheric pressure discharges. *Journal of Physics D: Applied Physics*, 38(2):R1, 2005.

[84] R. Gadri and J. Roth. Glow discharge-like characteristics of a oaugdp revealed by computer modeling. In *Plasma Science, 1998. 25th An-*

niversary. IEEE Conference Record - Abstracts. 1998 IEEE International on Plasma Science, page 288, jun 1998.

[85] N. Gherardi, G. Gouda, E. Gat, A. Ricard, and F. Massines. Transition from glow silent discharge to micro-discharges in nitrogen gas. *Plasma Sources Science and Technology*, 9(3):340, 2000.

[86] N. Gherardi and F. Massines. Mechanisms controlling the transition from glow silent discharge to streamer discharge in nitrogen. *IEEE Transactions on Plasma Science*, 29:536–544, 2001.

[87] V. I. Gibalov and G. J. Pietsch. The Development of Dielectric Barrier Discharges in Gas Gaps and on Surfaces. *Journal of Physics D: Applied Physics*, 33(20):2618, 2000.

[88] R. H. M. Giepman and M. Kotsonis. On the mechanical efficiency of dielectric barrier discharge plasma actuators. *Applied Physics Letters*, 98(22):221504, 2011.

[89] M. B. Glauert. The wall jet. *Journal of Fluid Mechanics*, 1(06):625–643, 1956.

[90] R. J. Goldston and P. H. Rutherford. *Introduction to Plasma Physics*. Institute of Physics Publishing, 1995.

[91] D. Greenblatt, B. Göksel, I. Rechenberg, C. Y. Schüle, D. Romann, and C. O. Paschereit. Dielectric Barrier Discharge Flow Control at Very Low Flight Reynolds Numbers. *AIAA Journal*, 46:1528–1541, 2008.

[92] J. W. Gregory, C. L. Enloe, G. I. Font, and T. E. McLaughlin. Force Production Mechanisms of a Dielectric-Barrier Discharge Plasma Actuator. In *AIAA 2007-185; 45th AIAA Aerospace Sciences Meeting and Exhibit, Reno, Nevada, USA*, 2007.

[93] S. Grundmann. *Transition Control using Dielectric Barrier Discharge Actuators*. PhD thesis, Technische Universität Darmstadt, 2008.

[94] S. Grundmann, M. Frey, and C. Tropea. Unmanned Aerial Vehicle (UAV) with Plasma Actuators for Separation Control. In *AIAA-2009-698; 47th AIAA Aerospace Science Meeting; Orlando, Florida, USA*, 2009.

[95] S. Grundmann, E. Sayles, and J. Eaton. Sensitivity of an Asymmetric 3D Diffuser to Plasma-Actuator Induced Inlet Condition Perturbations. *Experiments in Fluids*, 50:1–15, 2011.

[96] S. Grundmann and C. Tropea. Active Cancellation of Artificially Introduced Tollmien-Schlichting Waves using Plasma Actuators. *Experiments in Fluids*, 44:795–806, 2007.

[97] S. Grundmann and C. Tropea. Experimental Transition Delay Using Glow-Discharge Plasma Actuators. *Experiments in Fluids*, 42(4):653–657, 2007.

[98] S. Grundmann and C. Tropea. Experimental Damping of Boundary-Layer Oscillations using DBD Plasma Actuators. *International Journal of Heat and Fluid Flow*, 30:394–402, 2009.

[99] O. Guaïtella. *Nature de la synergie plasma-photocatalyseur pour la destruction d'un composé organique volatil type : l'acétylène.* PhD thesis, École Polytechnique, Palaiseau, 2006.

[100] J. R. Hollahan. *Techniques and Applications of Plasma Chemistry.* John Wiley & Sons Inc, 1974.

[101] A. Hoskinson and N. Hershkowitz. Differences between dielectric barrier discharge plasma actuators with cylindrical and rectangular exposed electrodes. *Journal of Physics D: Applied Physics*, 43:065205, 2010.

[102] A. Hoskinson, N. Hershkowitz, and D. Ashpis. Comparisons of Force Measurement Methods for DBD Plasma Actuators in Quiescent Air. In *AIAA 2009-485; 47th AIAA Aerospace Sciences Meeting, Orlando, Florida, USA*, 2009.

[103] A. R. Hoskinson, N. Hershkowitz, and D. E. Ashpis. Force Measurements of Single and Double Barrier DBD Plasma Actuators in Quiescent Air. *Journal of Physics D: Applied Physics*, 41(24):245209 (9pp), 2008.

[104] X. Huang and X. Zhang. Streamwise and spanwise plasma actuators for flow-induced cavity noise control. *Physics of Fluids*, 20(3):037101, 2008.

[105] X. Huang, X. Zhang, and Y. Li. Broadband Flow-Induced Sound Control using Plasma Actuators. *Journal of Sound and Vibration*, 329:2477 – 2489, 2010.

[106] G. M. Janssen. *Design of a General Plasma Simulation Model, Fundamental Aspects and Applications*. PhD thesis, Technische Universität Eindhoven, 2000.

[107] B. Jayaraman and W. Shyy. Modeling of dielectric barrier discharge-induced fluid dynamics and heat transfer. *Progress in Aerospace Sciences*, 44(3):139 – 191, 2008.

[108] J. Jolibois. *Etude et développement d'un actionneur plasma à décharge à barrière diélectrique - application au contrôle d'écoulement sur profil d'aile*. PhD thesis, Université de Poitiers, 2008.

[109] J. Jolibois, M. Forte, and r. Moreau. Application of an AC Barrier Discharge Actuator to Control Airflow Separation above a NACA 0015 Airfoil: Optimization of the Actuation Location along the Chord. *Journal of Electrostatics*, 66(9-10):496–503, 2008.

[110] J. Jolibois and E. Moreau. Enhancement of the Electromechanical Performances of a Single Dielectric Barrier Discharge Actuator. *IEEE Transactions on Dielectrics and Electrical Insulation*, 16(3):758–767, 2009.

[111] J. Jolibois, N. Zouzou, E. Moreau, and J. Tatibouët. Generation of surface dbd on rough dielectric: Electrical properties, discharge-induced electric wind and generated chemical species. *Journal of Electrostatics*, 69(6):522 – 528, 2011.

[112] T. Jukes, K. Choi, G. Johnson, and S. Scott. Characterization of Surface Plasma-Induced Wall Flows Through Velocity and Temperature Measurements. *AIAA Journal*, 44:764–771, Apr. 2006.

[113] T. N. Jukes and K.-S. Choi. Long Lasting Modifications to Vortex Shedding Using a Short Plasma Excitation. *Physical Review Letters*, 102(25):254501, 2009.

[114] W. Kim, H. Do, M. G. Mungal, and M. A. Capelli. On the role of oxygen in dielectric barrier discharge actuation of aerodynamic flows. *Applied Physics Letters*, 91:181501, 2007.

[115] U. Kogelschatz. Dielectric-Barrier Discharges: Their History, Discharge Physics, and Industrial Applications. *Plasma Chemistry and Plasma Processing*, 23:1–46, 2003.

[116] U. Kogelschatz, B. Eliasson, and W. Egli. From ozone generators to flat television screens: history and future potential of dielectric-barrier discharges. *Pure and Applied Chemistry*, 71(10):1819–1828, 1999.

[117] M. Kotsonis, S. Ghaemi, R. Giepman, and L. Veldhuis. Experimental study on the body force field of dielectric barrier discharge actuators. In *AIAA 2010-4630; 41st Plasmadynamics and Lasers Conference, Chicago, Illinois, USA*, 2010.

[118] M. Kotsonis, S. Ghaemi, L. Veldhuis, and F. Scarano. Measurement of the body force field of plasma actuators. *Journal of Physics D: Applied Physics*, 44(4):045204, 2011.

[119] A. V. Kozlov and F. O. Thomas. Bluff-body flow control via two types of dielectric barrier discharge plasma actuation. *AIAA Journal*, 49:1919–1931, 2011.

[120] A. V. Kozlov and F. O. Thomas. Plasma flow control of cylinders in a tandem configuration. *AIAA Journal*, 49:2183–2193, 2011.

[121] J. Kriegseis, T. Dehler, M. Gnirß, and C. Tropea. Common-Base Proper Orthogonal Decomposition (CPOD) as a Means of Quantitative Data Comparison. *Measurement Science and Technology*, 21:085403 (7pp), 2010.

[122] J. Kriegseis, T. Dehler, S. Grundmann, and C. Tropea. Flowfield-Characteristics Generated by DBD Plasma Actuators. In A. Dillmann, G. Heller, M. Klaas, H.-P. Kreplin, W. Nitsche, and W. Schröder, editors, *New Results in Numerical and Experimental Fluid Mechanics VII*, volume 112 of *Notes on Numerical Fluid Mechanics and Multidisciplinary Design*, pages 233–240. Springer Berlin / Heidelberg, 2010.

[123] J. Kriegseis, T. Dehler, M. Pawlik, and C. Tropea. Pattern-Identification Study of the Flow in Proximity of a Plasma Actuator. In *AIAA-2009-1001; 47th AIAA Aerospace Science Meeting; Orlando, Florida, USA*, 2009.

[124] J. Kriegseis, S. Grundmann, and C. Tropea. Power Consumption, Discharge Capacitance and Light Emission as Measures for Thrust Production of Dielectric Barrier Discharge Plasma Actuators. *Journal of Applied Physics*, 110(1):013305, 2011.

[125] J. Kriegseis, S. Grundmann, and C. Tropea. Performance Reduction of Dielectric Barrier Discharge Plasma Actuators at Higher Mach Numbers. In *New Results in Numerical and Experimental Fluid Mechanics VIII*, Notes on Numerical Fluid Mechanics and Multidisciplinary Design. Springer Berlin / Heidelberg, (under review).

[126] J. Kriegseis, A. Kurz, A. Duchmann, S. Grundmann, and C. Tropea. Influence of air flow on the performance of DBD Plasma Actuators. In *50th AIAA Aerospace Sciences Meeting, Nashville, Tennessee, USA (accepted)*, 2012.

[127] J. Kriegseis, B. Möller, S. Grundmann, and C. Tropea. Capacitance and power consumption quantification of dielectric barrier discharge (DBD) plasma actuators. *Journal of Electrostatics*, 69(4):302 – 312, 2011.

[128] J. Kriegseis, B. Möller, S. Grundmann, and C. Tropea. Light Emission, Discharge Capacitance and Thrust Production of DBD Plasma Actuators. In *AIAA 2011-155; 49th AIAA Aerospace Sciences Meeting, Orlando, Florida, USA*, 2011.

[129] J. Kriegseis, D. Schröter, S. Grundmann, and C. Tropea. Online-characterization of dielectric barrier discharge plasma actuators for optimized efficiency of aerodynamical flow control applications. *Journal of Physics: Conference Series*, 301(1):012020, 2011.

[130] J. Kriegseis, C. Schwarz, A. Duchmann, S. Grundmann, and C. Tropea. PIV-based Estimation of DBD Plasma-Actuator Force terms. In *50th AIAA Aerospace Sciences Meeting, Nashville, Tennessee, USA (accepted)*, 2012.

[131] E. E. Kunhardt. Generation of large-volume, atmospheric-pressure, nonequilibrium plasmas. *IEEE Transactions on Plasma Science*, 28:189–200, 2000.

[132] A. Labergue. *Etude de décharges électriques dans lŠair pour le développement dŠactionneurs plasmas Ű Application au contrôle de décollements dŠécoulements*. PhD thesis, Université de Poitiers, 2002.

[133] A. Labergue, L. Léger, E. Moreau, G. Touchard, and J.-P. Bonnet. Experimental study of the detachment and the reattachment of an airflow along an inclined wall controlled by a surface corona dischargeŮapplication to a plane turbulent mixing layer. *IEEE Transactions on Industry Applications*, 40:1205–1214, 2004.

[134] Y. Lagmich, T. Callegari, L. C. Pitchford, and J. P. Boeuf. Model description of surface dielectric barrier discharges for flow control. *Journal of Physics D: Applied Physics*, 41(9):095205, 2008.

[135] L. Léger, E. Moreau, and G. Touchard. Electrohydrodynamic airflow control along a flat plate by a dc surface corona discharge - velocity profile and wall pressure measurements. In *AIAA 2002 - 2833, 1st Flow Control Conference, St. Louis, Missouri, USA*, 2002.

[136] S. Lemire, H. D. Vo, and M. W. Benner. Performance Improvement of Axial Compressors and Fans with Plasma Actuation. *International Journal of Rotating Machinery*, 2009:13 pages, 2009.

[137] S. Leonov, D. Opaits, R. Miles, and V. Soloviev. Time-resolved measurements of plasma-induced momentum in air and nitrogen under dielectric barrier discharge actuation. *Physics of Plasmas*, 17(11):113505, 2010.

[138] S. B. Leonov and D. A. Yarantsev. Near-Surface Electrical Discharge in Supersonic Airflow: Properties and Flow Control. *Journal of Propulsion and Power*, 24(6):1168–1181, 2008.

[139] Y.-h. Li, Y. Wu, M. Zhou, C.-b. Su, X.-w. Zhang, and J.-q. Zhu. Control of the corner separation in a compressor cascade by steady and unsteady plasma aerodynamic actuation. *Experiments in Fluids*, 48:1015–1023, 2010.

[140] E. Lifshitz and L. Pitaevskiĭ. *Physical kinetics*. Course of theoretical physics. Butterworth-Heinemann, 1981.

[141] A. V. Likhanskii, M. N. Shneider, S. O. Macheret, and R. B. Miles. Modeling of Interaction Between Weakly Ionized Near-Surface Plasmas and Gas Flow. In *AIAA 2006-1204; 44th AIAA Aerospace Sciences Meeting and Exhibit, Reno, Nevada, USA*, 2006.

[142] A. V. Likhanskii, M. N. Shneider, S. O. Macheret, and R. B. Miles. Modeling of dielectric barrier discharge plasma actuators driven by repetitive nanosecond pulses. *Physics of Plasmas*, 14(7):073501, 2007.

[143] A. V. Likhanskii, M. N. Shneider, S. O. Macheret, and R. B. Miles. Modeling of dielectric barrier discharge plasma actuator in air. *Journal of Applied Physics*, 103(5):053305, 2008.

[144] J. Little, M. Nishihara, I. Adamovich, and M. Samimy. High-Lift Airfoil Trailing Edge Separation Control using a Single Dielectric Barrier Discharge Plasma Actuator. *Experiments in Fluids*, 48:521–537, 2010.

[145] S. Liu and M. Neiger. Excitation of Dielectric Barrier Discharges by Unipolar Submicrosecond Square Pulses. *Journal of Physics D: Applied Physics*, 34:1632–1638, 2001.

[146] L. B. Loeb. Electrical breakdown of gases with steady or direct current impulse potentials. In S. Flügge, editor, *Encyclopedia of Physics*, volume Volume 22: Gas Discharges 2, pages 445–530. Springer, 1956.

[147] S. O. Macheret, M. N. Shneider, and R. C. Murray. Ionization in strong electric fields and dynamics of nanosecond-pulse plasmas. *Physics of Plasmas*, 13(2):023502, 2006.

[148] P. Magnier, V. Boucinha, B. Dong, R. Weber, A. Leroy-Chesneau, and D. Hong. Experimental Study of the Flow Induced by a Sinusoidal Dielectric Barrier Discharge Actuator and Its Effect on a Flat Plate Natural Boundary Layer. *Journal of Fluids Engineering*, 131:011203, 2009.

[149] T. C. Manley. The Electric Characteristics of the Ozonator Discharge. *Journal of The Electrochemical Society*, 84(1):83–96, 1943.

[150] J. Meek and J. Craggs, editors. *Electrical Breakdown of Gases*. John Wiley & Sons, 1978.

[151] R. Mestiri, R. Hadaji, and S. B. Nasrallah. An experimental study of a plasma actuator in absence of free airflow: Ionic wind velocity profile. *Physics of Plasmas*, 17(8):083503, 2010.

[152] A. Mizuno. Industrial applications of atmospheric non-thermal plasma in environmental remediation. *Plasma Physics and Controlled Fusion*, 49:A1–A15, 2007.

[153] A. Mizuno. Recent development of electrostatic technologies in environmental remediation. In *Industry Applications Society Annual Meeting, 2009. IAS 2009. IEEE*, pages 1 –7, oct. 2009.

[154] B. Möller. Development and Experimental Investigation of Valuation Methods for the Energetic Efficiency of DBD Plasma Actuators. Master's thesis, Technische Universität Darmstadt, 2010.

[155] E. Moreau. Airflow Control by Non-Thermal Plasma Actuators. *Journal of Physics D: Applied Physics*, 40:605–636, 2007.

[156] E. Moreau, L. Léger, and G. Touchard. Effect of a dc surface-corona discharge on a flat plate boundary layer for air flow velocity up to 25 m/s. *Journal of Electrostatics*, 64(3-4):215 – 225, 2006.

[157] E. Moreau, R. Sosa, and G. Artana. Electric wind produced by surface plasma actuators: a new dielectric barrier discharge based on a three-electrode geometry. *Journal of Physics D: Applied Physics*, 41, 2008.

[158] D. Nelson, M. Benhenni, O. Eichwald, and M. Yousfi. Ion swarm data for electrical discharge modeling in air and flue gas mixtures. *Journal of Applied Physics*, 94:96, 2003.

[159] G. Nersisyan and W. G. Graham. Characterization of a Dielectric Barrier Discharge Operating in an Open Reactor with Flowing Helium. *Plasma Sources Science Technology*, 13:582–587, Nov. 2004.

[160] H. Nobach and E. Bodenschatz. Limitations of accuracy in piv due to individual variations of particle image intensities. *Experiments in Fluids*, 47:27–38, 2009.

[161] D. F. Opaits, A. V. Likhanskii, G. Neretti, S. Zaidi, M. N. Shneider, and S. O. Miles, R B Macheret. Experimental Investigation of Dielectric Barrier Discharge Plasma Actuators Driven by Repetitive High-Voltage Nanosecond Pulses with DC or Low Frequency Sinusoidal Bias. *Journal of Applied Physics*, 104:043304–+, 2008.

[162] D. F. Opaits, G. Neretti, A. V. Likhanskii, S. Zaidi, M. N. Shneider, and R. B. Miles. Experimental Investigation of DBD Plasma Actuators Driven by Repetitive High Voltage Nanosecond Pulses with DC or Low-Frequency Sinusoidal Bias. In *AIAA 2007-4532; 38th AIAA Plasmadynamics and Lasers Conference, Miami, FL, USA*, 2007.

[163] D. F. Opaits, G. Neretti, S. H. Zaidi, M. N. Shneider, R. B. Miles, A. V. Likhanskii, and S. O. Macheret. DBD Plasma Actuators Driven by a Combination of Low Frequency Bias Voltage and Nanosecond

Pulses. In *AIAA 2008-1372; 46th AIAA Aerospace Sciences Meeting and Exhibit, Reno, Nevada, USA*, 2008.

[164] D. Orlov. *Modelling and Simulation of Single Dielectric Barrier Discharge Plasma Actuators*. PhD thesis, University of Notre Dame, USA, 2006.

[165] D. Orlov, T. Apker, C. He, H. Othman, and T. Corke. Modeling and Experiment of Leading Edge Separation Control Using SDBD Plasma Actuators. In *AIAA 2007-0877; 45th Aerospace Sciences Meeting, 8-11 January 2007, Reno, Nevada, USA*, 2007.

[166] D. Orlov, T. Corke, and M. Patel. Electric Circuit Model for Aerodynamic Plasma Actuator. In *AIAA 2006-1206; 44th AIAA Aerospace Science Meeting and Exhibit; Reno, Nevada, USA*, 2006.

[167] D. Orlov and T. C. Corke. Numerical Simulation of Aerodynamic Plasma Actuator Effects. In *AIAA 2005-1083; AIAA 43rd Aerospace Sciences Meeting, Reno, Nevada, USA*, 2005.

[168] D. M. Orlov, G. I. Font, and D. Edelstein. Characterization of Discharge Modes of Plasma Actuators. *AIAA Journal*, 46(12):3142–3148, 2008.

[169] F. Paschen. Ueber die zum funkenübergang in luft, wasserstoff und kohlensäure bei verschiedenen drucken erforderliche potentialdifferenz. *Annalen der Physik*, 273(5):69–96, 1889.

[170] M. P. Patel, T. T. Ng, S. Vasudevan, T. Corke, M. Post, T. McLaughlin, and C. F. Suchomel. Scaling effects of an Aerodynamic Plasma Actuator. *Journal of Aircraft*, 45:223–236, 2008.

[171] S. Pavon. *Interaction Between a Surface Dielectric Barrier Discharge and Transonic Airflows*. PhD thesis, Lausanne, 2008.

[172] S. Pavon, J.-L. Dorier, C. Hollenstein, P. Ott, and P. Leyland. Effects of High-Speed Airflows on a Surface Dielectric Barrier Discharge. *Journal of Physics D: Applied Physics*, 40:1733–1741, 2007.

[173] S. Pavon, P. Ott, P. Leyland, J.-L. Dorier, and C. Hollenstein. Effects of a surface dielectric barrier discharge on transonic flows around an airfoil. In *AIAA 2009-649; 47th AIAA Aerospace Sciences Meeting, Orlando, Florida, USA*, 2009.

[174] J. Poggie, C. P. Tilmann, P. M. Flick, J. S. Silkey, B. A. Osborne, G. Ervin, D. Maric, S. Mangalam, and A. Mangalam. Closed-Loop Stall Control on a Morphing Airfoil Using Hot-Film Sensors and DBD Actuators. In *AIAA 2010-547; 48th AIAA Aerospace Sciences Meeting, Orlando, Florida, USA*, 2010.

[175] J. Pons, E. Moreau, and G. Touchard. Asymmetric Surface Dielectric Barrier Discharge in Air at Atmospheric Pressure: Electrical Properties and Induced Airflow Characteristics. *Journal of Physics D: Applied Physics*, 38(19):3635, 2005.

[176] C. Porter, A. Abbas, K. Cohen, T. McLaughlin, and C. Enloe. Spatially Distributed Forcing and Jet Vectoring with a Plasma Actuator. *AIAA Journal*, 47(6):1368–1378, 2009.

[177] C. O. Porter, J. W. Baughn, T. E. McLaughlin, C. L. Enloe, and G. I. Font. Plasma Actuator Force Measurements. *AIAA Journal*, 45:1562–1570, July 2007.

[178] C. O. Porter, T. E. McLaughlin, C. L. Enloe, G. I. Font, J. Roney, and J. W. Baughn. Boundary Layer Control Using a DBD Plasma Actuator. In *AIAA 2007-786; 45th AIAA Aerospace Sciences Meeting and Exhibit, Reno, Nevada, USA*, 2007.

[179] C. O. Porter, B. J. W, T. E. McLaughlin, C. L. Enloe, and G. I. Font. Temporal Force Measurements on an Aerodynamic Plasma Actuator. In *AIAA 2006-1206; 44th AIAA Aerospace Science Meeting and Exhibit; Reno, Nevada, USA*, 2006.

[180] M. L. Post and T. C. Corke. Separation control on high angle of attack airfoil using plasma actuators. *AIAA Journal*, 42:2177 – 2184, 2004.

[181] M. Raffel, C. Willert, S. Wereley, and J. Kompenhans. *Particle Image Velocimetry: A Practical Guide*. Springer, 2007.

[182] Y. P. Raizer. *Gas Discharge Physics*. Springer, 1991.

[183] Y. P. Raizer, M. N. Shneider, and N. A. Yatsenko. *Radio-Frequency Capacitive Discharges*. CRC Press, 1995.

[184] G. G. Raju. *Dielectrics in Electric Fields*. Marcel Dekker, Inc., 2003.

[185] D. Rival, R. Manejev, and C. Tropea. Measurement of parallel blade–vortex interaction at low Reynolds numbers. *Experiments in Fluids*, 1:2, 2010.

[186] D. Rival, D. Schönweitz, and C. Tropea. Vortex interaction of tandem pitching and plunging plates: a two-dimensional model of hovering dragonfly-like flight. *Bioinspiration & Biomimetics*, 6:016008, 2011.

[187] M. Robinson. Movement of Air in the Electric Wind of the Corona Discharge. Technical report, Trans. of AIEE, 1960.

[188] J. Roth. United States Patent, *Patent Number 5,387,842*, Date of Patent: Feb. 7, 1995.

[189] J. R. Roth. *Industrial Plasma Engineering; Volume 1: Principles*. IOP, 1995.

[190] J. R. Roth. *Industrial Plasma Engineering; Volume 2: Applications*. IOP, 2001.

[191] J. R. Roth, D. Sherman, and S. P. Wilkinson. Boundary Layer Flow Control with a One Atmosphere Uniform Glow Discharge Surface Plasma. In *AIAA 1998-0328; 36th AIAA Aerospace Science Meeting and Exhibit; Reno, Nevada, USA*, 1998.

[192] R. J. Roth and X. Dai. Optimization of the Aerodynamic Plasma Actuator as an Electrohydrodynamic (EHD) Electrical Device. In *AIAA 2006-1203, 44th AIAA Aerospace Sciences Meeting and Exhibit, Reno, Nevada, USA*, 2006.

[193] R. J. Roth, J. Rahel, X. Dai, and D. M. Sherman. The Physics and Phenomenology of One Atmosphere Uniform Glow Discharge Plasma Reactors for Surface Treatment Applications. *Journal of Physics D: Applied Physics*, 38:555–567, 2005.

[194] S. Roy and C.-C. Wang. Bulk flow modification with horseshoe and serpentine plasma actuators. *Journal of Physics D: Applied Physics*, 42:032004, 2009.

[195] H. Ryzko. Drift velocity of electrons and ions in dry and humid air and in water vapour. *Proceedings of the Physical Society*, 85:1283, 1965.

[196] A. Santhanakrishnan and J. Jacob. Effect of plasma morphology on flow control using plasma synthetic jet actuators. In *45th AIAA Aerospace Sciences Meeting and Exhibit, Jan.8-11 2007, Reno, NV, USA*, 2007.

[197] A. Santhanakrishnan and J. Jacob. Flow control with plasma synthetic jet actuators. *Journal of Physics D: Applied Physics*, 40(3):637, 2007.

[198] A. Savitzky and M. J. E. Golay. Smoothing and Differentiation of Data by Simplified Least Squares Procedures. *Analytical Chemistry*, 36(8):1627–1639, July 1964.

[199] A. Séraudie, O. Vermeersch, and D. Arnal. DBD Plasma actuator effect on a 2D model laminar boundary layer. Transition delay under ionic wind effect. In *AIAA 2011-3515; 29th AIAA Applied Aerodynamics Conference, Honolulu, Hawaii, USA*, 2011.

[200] M. Shneider, A. Likhanskii, S. Macheret, D. Opaits, and D. Miles. State-of-the-art high-fidelity dbd plasma simulations. In *AFOSR DBD Plasma Actuator Workshop, 24-25 February 2010, Gainesville, FL*, 2010.

[201] W. Shyy, B. Jayaraman, and A. Andersson. Modeling of glow discharge-induced fluid dynamics. *Journal of Applied Physics*, 92:6434, 2002.

[202] W. Siemens. Ueber die elektrostatische Induction und die Verzögerung des Stroms in Flaschendrähten. *Annalen der Physik*, 178(9):66–122, 1857.

[203] K. P. Singh and S. Roy. Impedance Matching for an Asymmetric Dielectric Barrier Discharge Plasma Actuator. *Applied Physics Letters*, 91(8):081504, 2007.

[204] K. P. Singh and S. Roy. Force approximation for a plasma actuator operating in atmospheric air. *Journal of applied Physics 103, 013305*, 2008.

[205] K. P. Singh and S. Roy. Physics of plasma actuator operating in atmospheric air. *Applied Physics Letters*, 92(11):111502, 2008.

[206] B. Smirnov. *Physics of weakly ionized gases*. Mir Publishers Moscow, 1981.

[207] B. M. Smirnov. *Physics of Ionized Gases*. Wiley Interscience, 2001.

[208] A. Soldati. Modulation of turbulent boundary layer by ehd flows. *ERCOFTAC Bulletin*, (44):50 – 56, 2000.

[209] A. Soldati and S. Banerjee. Turbulence modification by large-scale organized electrohydrodynamic flows. *Physics of Fluids*, 10(7):1742–1756, 1998.

[210] J. H. Spurk. *Fluid Mechanics*. Springer, 1997.

[211] S. A. Stanfield. *A Spectroscopic Investigation of a Surface-Discharge-Mode, Dielectric Barrier Discharge*. PhD thesis, Wright State University, 2005.

[212] C. Steffes. Erste Ansätze einer neuen Strategie zur effizienten Modellierung eines Plasma-Aktuators auf Basis des Verständnisses bestehender Modelle. Master's thesis, TU Darmstadt, 2008.

[213] M. Takagaki, S. Isono, H. Nagai, and K. Asai. Evaluation of Plasma Actuator Performance in Martian Atmosphere for Applications to Mars airplanes. In *AIAA 2008-3762; 4th AIAA Flow Control Conference, Seattle, Washington, USA*, 2008.

[214] K. Takashima, N. Zouzou, E. Moreau, A. Mizuno, and G. Touchard. Generation of Extended Surface Barrier Discharge on Dielectric Surface - Electrical Properties - . *International Journal of Plasma Environmental Science and Technology*, 1:14–20, 2007.

[215] E. Temmerman. *Experimental Study of Non-Thermal Plasmas at Atmospheric Pressure for Surface Modification*. PhD thesis, Universiteit Gent, 2006.

[216] F. O. Thomas, T. C. Corke, M. Iqbal, A. Kozlov, and D. Schatzman. Optimization of Dielectric Barrier Discharge Plasma Actuators for Active Aerodynamic Flow Control. *AIAA Journal*, 47:2169–2178, 2009.

[217] C. Tropea, F. Scarano, J. Westerweel, A. A. Cavone, J. F. Meyers, J. W. Lee, and R. Schodl. Particle-Based Techniques. In C. Tropea, A. L. Yarin, and J. F. Foss, editors, *Springer Handbook of Experimental Fluid Mechanics*, chapter Velocity, Vorticity and Mach Number, pages 287–362. Springer, Heidelberg, 2007.

[218] X. Tu, H. J. Gallon, M. V. Twigg, P. A. Gorry, and J. C. Whitehead. Dry reforming of methane over a Ni/Al2O3 catalyst in a coaxial dielectric barrier discharge reactor. *Journal of Physics D: Applied Physics*, 44(27):274007, 2011.

[219] T. Unfer and J.-P. Boeuf. Modeling and comparison of sinusoidal and nanosecond pulsed surface dielectric barrier discharges for flow control. *Plasma Physics and Controlled Fusion*, 52:1–11, 2010.

[220] T. Unfer, R. F. Boeuf, J.-P., and F. Thivet. Modeling of Dielectric Barrier Discharge and coupling with Computational Fluid Dynamics. In *AIAA 2008-1375; 46th AIAA Aerospace Sciences Meeting and Exhibit, Reno, Nevada, USA*, 2008.

[221] R. Van Dyken, T. E. McLaughlin, and C. L. Enloe. Parametric Investigations of a Single Dielectric Barrier Plasma Actuator. In *AIAA 2004-0846*, 2004.

[222] B. van Oudheusden, F. Scarano, E. Roosenboom, E. Casimiri, and L. Souverein. Evaluation of integral forces and pressure fields from planar velocimetry data for incompressible and compressible flows. *Experiments in Fluids*, 43(2):153–162, 2007.

[223] B. W. van Oudheusden, F. Scarano, and E. W. F. Casimiri. Non-intrusive load characterization of an airfoil using piv. *Experiments in Fluids*, 40:988–992, 2006.

[224] H. R. Velkoff and J. Ketcham. Effect of an Electrostatic Field on Boundary-Layer Transition. *AIAA Journal*, 6:1381–1383, 1968.

[225] P. Versailles, V. Gingras-Gosselin, and H. Vo. Impact of Pressure and Temperature on the Performance of Plasma Actuators. *AIAA Journal*, 48:859–863, 2010.

[226] H. D. Vo, J. D. Cameron, and S. C. Morris. Control of short length-scale rotating stall inception on a high-speed axial compressor with plasma actuation. In *GT2008-50967, Proceedings of ASME Turbo Expo 2008: Power of Land, Sea and Air, Berlin, Germany*, 2008.

[227] K. Vollrath. Funkenlichtquellen und Hochfrequenz-Funkenkinematographie. In K. Vollrath and G. Thomer, editors, *Kurzzeitphysik*, pages 76–165. Springer, 1967.

[228] A. von Engel. Ionization in gases by electrons in electric fields. In S. Flügge, editor, *Encyclopedia of Physics*, volume Volume 21: Electron-Emission Gas Discharges 1, pages 504–573. Springer, 1956.

[229] H. E. Wagner, R. Brandenburg, K. V. Kozlov, A. Sonnenfeld, P. Michel, and J. F. Behnke. The Barrier Discharge: Basic Properties and Applications to Surface Treatment. *Vacuum*, 71(3):417 – 436, 2003.

[230] C.-C. Wang, R. Durscher, and S. Roy. Three-dimensional effects of curved plasma actuators in quiescent air. *Journal of Applied Physics*, 109(8):083305, 2011.

[231] J. Westerweel. Fundamentals of digital particle image velocimetry. *Measurement Science and Technology*, 8:1379–1392, 1997.

[232] F. M. White. *Viscous Fluid Flow*. McGraw-Hill Education, 1974.

[233] A. Widmann, A. Duchmann, A. Kurz, S. Grundmann, and C. Tropea. Measuring Tollmien-Schlichting Waves using Phase-Averaged Particle Image Velocimetry. *Experiments in Fluids*, page 16pp, (under review).

[234] B. Wilke. *Aerodynamische Strömungssteuerung mittels dielektrischen Barriereentladungs-Plasmaaktuatoren*. PhD thesis, Technische Universität Darmstadt, DLR Göttingen, 2009.

[235] S. P. Wilkinson. Investigation of an Oscillating Surface Plasma for Turbulent Drag Reduction. In *AIAA 2003 - 1023; 41st Aerospace Sciences Meeting and Exhibit, Reno, Nevada, USA*, 2003.

[236] Y. Wu, Y. Li, M. Jia, H. Song, Z. Guo, X. Zhu, and Y. Pu. Influence of operating pressure on surface dielectric barrier discharge plasma aerodynamic actuation characteristics. *Applied Physics Letters*, 93(3):031503, 2008.

[237] X. Yang, Z. Zhitao, L. Cheng, and X. Yu. Effect of systematic resonance on dbd device. *Plasma Science and Technology*, 7(5):3030, 2005.

[238] J. C. Zito, D. P. Arnold, R. J. Durscher, and S. Roy. Investigation of Impedance Characteristics and Power Delivery for Dielectric Barrier Discharge Plasma Actuators. In *AIAA-2010-0964; 48th AIAA Aerospace Science Meeting; Orlando, Florida, USA*, 2010.

Nomenclature

Latin letters

upper case

symbol	SI unit	description
A	m^2	enclosed area of example functions $\varphi_1(t)$ and $\varphi_2(t)$
A_{CV}	m^2	area of CV
A_{s}	V^2	enclosed area of V and V_{p}
Ar	–	argon
C, $C(t)$	F	capacitance
C_{a}	F	actuator capacitance
C_{d}	F	dielectric capacitance
C_{eff}	F	effective capacitance
C_{eff}^{+}	F	effective capacitance of positive half-cycle
C_{eff}^{-}	F	effective capacitance of negative half-cycle
C_{g}	F	gas capacitance
C_{p}	F	charge-probe capacitance
C_{p}	F	capacitance of plasma
C_{t}	F	total capacitance
C_{VD}	F	capacitance of volume discharge
C_0	F	pure passive-component capacitance / cold capacitance
$\vec{E}$, E	V/m	electric field
$\vec{E}_{\mathrm{b}}$	V/m	electric breakdown field strength
E_k	W s	consumed energy per discharge cycle k
E_0	V/m	reference (maximum) field strength
E^i	V/m	electric field for time step i

F	$\mathrm{N} = \mathrm{kg\,m/s^2}$	steady force
F, F_i	N	plasma force
F_t	N	thrust
F_b	N	body force
F_f	N	friction force
$F_i^{(V)}$	N	volume forces
$F_i^{(S)}$	N	surface forces
$G(x,t)$	–	gray value as a function of chord and time
$G(x)$	–	spanwise averaged light intensity
G_b	–	gray value of background
G_p	–	gray value of light-emission peak
G_peak	–	maximum gray value
$\widehat{G}$	–	relative discharge peak intensity /
	–	peak luminosity
H_1, H_2	m	lengths of rocker
H_2	–	molecular hydrogen
He	–	helium
I, $I(t)$	A	electric current
I_i	$\mathrm{Ns} = \mathrm{kg\,m/s}$	momentum
I_input	A	input current
J	–	number of raw images
K	–	scaling number
K	–	number of discharge cycles k
L, L_1, L_2	m	actuator length
$L(x,z,t)$	W	spatio-temporal luminosity distribution
L_p	$\mathrm{H} = \Omega\mathrm{s}$	inductance of plasma
M	–	Mach number
M	kg	sum of mass elements
N	–	number of images
N_z	–	spanwise number of gray-value informations
Ne	–	neon
N_W	–	number of plateaus of $W(t)$

N_2	–	molecular nitrogen
P_A	W	power consumption / actuator power
$P_{\mathrm{A},k}$	W	consumed power per discharge cycle k
P_A^i	W	Power consumption for time step i
P_A^*	W	pre-set power level
P_FM	W	fluid-mechanical power
P_input	W	input power
P_loss	W	power loss
P_S	W	power saving
Q, $Q(t)$	C	electric charge
Q_max	C	maximum electric charge
R	Ω	electric resistance
R_g	Ω	electrical resistance of gas
R_p	Ω	resistance of plasma
$S, S(t)$	m^2	surface
T	s	period of periodic function
T	K	temperature
T_e	K	temperature of electrons
T_i	K	temperature of ions
T_g	K	temperature of neutral gas
T_n	K	temperature of neutrals
T'	eV	kinetic temperature
T'_e	eV	kinetic electron temperature
U_i	m/s	flow fields snapshot
U_max	m/s	maximum wall-jet velocity
U_∞	m/s	free-stream velocity
V, $V(t)$	V	operating voltage (peak-to-peak)
V, $V(t)$	m^3	volume/ bounded volume
V_b	V	breakdown voltage (ignition potential)
$V_{\mathrm{b}_\mathrm{min}}$	V	minimum breakdown voltage
V_input	V	input voltage
V_max	V	maximum operating voltage (peak-to-peak)
V_p, $V_\mathrm{p}(t)$	V	charge-probe voltage (peak-to-peak)

V_{supply}	V	supply voltage
$W(t)$	kg	weight balance signal
$\overline{W}_n$	kg	average of balance signals

lower case

symbol	SI unit	description
a_∞	m/s	sonic speed
d	m	electrode distance
d	m	thickness of dielectric
d_N	m	diameter of nozzle
e	C	electron charge
f	$\text{Hz} = 1/\text{s}$	operating frequency
f_i	$\text{kg/m}^2\text{s}^2$	volume-force density
f_{res}	Hz	natural resonant frequency
f_{x}	$\text{kg/m}^2\text{s}^2$	chordwise force density
f_{y}	$\text{kg/m}^2\text{s}^2$	wall normal force density
g	m/s^2	acceleration of gravity
$g_j(x, z)$	–	j^{th} spatial gray-value distribution
$\overline{g}(x, z)$	–	average spatial gray-value distribution
i	–	spanwise location ($i \in N_z$)
i, j, k	–	control variables of the coordinates
j	–	raw-image number ($j \in J$)
k	$\text{kg m}^2/\text{s}^2\text{K}$	Boltzmann's constant
k	–	discharge-cycle number ($k \in K$)
k_i, $\vec{k}$	m/s^2	specific body force
m	kg	mass
n	$1/\text{m}^3$	electron number density / charge number density
n	–	n^{th} plateau of weight balance signal $W(t)$
n	–	n^{th} flow field $U_i(x, y)$
n_{i}	$1/\text{m}^3$	number density of ions

n_i	–	surface normal
n_n	$1/\mathrm{m}^3$	number density of neutrals
p	$\mathrm{bar} = \mathrm{kg/m\,s^2}$	gas/static pressure
p_max	bar	maximum static pressure
p_min	bar	minimum static pressure
p_t	bar	total pressure
p_0	bar	ambient pressure
t	s	time
t_i, t^i	s	time step i
t_1, t_2, t_3	s	characteristic time
t_i, $\vec{t}$	$\mathrm{kg/m\,s^2}$	stress vector
u	m/s	velocity component in x-direction
u_i	m/s	velocity (free index i)
u_max	m/s	maximum velocity
u^*	–	normalized velocity
v	m/s	velocity component in y-direction
$\vec{v}_\mathrm{d}$, v_d	m/s	drift velocity
w_1	m	dimension upper electrode
w_2	m	dimension lower electrode
x	m	chordwise coordinate
x_max	m	maximum x-coordinate
x_min	m	minimum x-coordinate
y	m	wall normal coordinate
y_max	m	maximum y-coordinate
y_min	m	minimum y-coordinate
y^*	–	normalized wall normal distance
z	m	spanwise coordinate

Greek letters

upper case

symbol	SI unit	description
Δt	s	exposure time
Δt	s	computation sequence of control circuit
Δx	m	chordwise plasma length (light-emission based)
Δx_{F}	m	chordwise penetration length (force-determination based)
ΔW_n	kg	difference between two consecutive averaged balance signals $\overline{W}_n$
$\Delta\rho$	kg/m^3	maximal density deviations
$\Delta\phi$	–	phase relation
Θ_{A}	$\mathrm{s}^{\frac{3}{2}}\mathrm{A}^{\frac{7}{2}}/\mathrm{W}^{\frac{5}{2}}\mathrm{m}$	scaling number
Π_ϕ	–	relative performance of general variable ϕ
Π_ϕ^c	–	relative performance (controlling mode)
Π_ϕ^m	–	relative performance (monitoring mode)
Π_ϕ^*	–	normalized regression line
$\overline{\Pi}_\phi$	–	relative performance based on $\phi^*\vert_{M=0}$
Ψ_ϕ	–	relative performance drop of gen. var. ϕ
$\overline{\Psi}_\phi$	–	relative performance drop based on $\phi^*\vert_{M=0}$
Ω, Ω^i	–	remote-control signal / for time step i

lower case

symbol	SI unit	description
α	–	degree of ionization
β	–	regression coefficient
δ	m	wall-jet thickness
$\delta_{1/2}$	m	wall-normal distance of 50% wall-jet velocity
ε_0	C/Vm	permittivity of free space

η	Pa s=Ns/m^2	dynamical viscosity
η_{E}	–	electrical efficiency
η_{FM}	–	fluid-mechanical efficiency
η^*_{FM}	N/W	fluid-mechanical effectiveness
η'_{FC}	–	overall effectiveness of the plasma actuator
η'_{S}	–	saving rate
λ_{D}	m	Debye length
λ^i_{DBD}	–	species-dependent i^{th} wavelength
λ^*	m^2/s	bulk viscosity
μ, μ_e, μ_i	m^2/Vs	mobility, of electrons, of ions
ν_{m}	1/s	collision frequency
ξ_ϕ	–	relative slope of the performance Π_ϕ
σ_{G}	–	standard deviation of gray values
$\sigma_{\overline{g}}$	–	standard deviation of J light-emission
$\sigma_{\mathrm{P_A}}$	–	standard deviation of calculated power
σ_{u_i}	–	standard deviation of time-averaged velocity distribution
$\sigma_{\mathrm{W_n}}$	–	standard deviation of weight balance signal
$\sigma_{\Delta W_n}$	–	standard deviation of ΔW_n
τ_{ij}	Pa=N/m^2	stress tensor
τ_{w}	Pa=N/m^2	wall-shear stress
ρ, $\rho(\vec{x},t)$	kg/m^3	density
$\overline{\rho}$	kg/m^3	mean density
ϕ	–	general variable
$\phi(t)$	–	phase angle
ϕ^*	–	regression line of ϕ
$\varphi_1(t)$, $\varphi_2(t)$	–	example functions
ω , ω_k , ω_z	1/s	vorticity

Mathematical symbols

symbol	description
$\mathrm{D}/\mathrm{D}t$	material derivative, see (5.3)
e_{ij}	deformation tensor, see (5.16)
δ_{ij}	Kronecker delta
ϵ_{ijk}	epsilon tensor, (permutation symbol)

Abbreviations

symbol	description
AC	Alternating current
AWC	active wave cancelation
CAM	camera
CCD	Charged Coupled Device
CMOS	Complementary Metal Oxide Semiconductor
CTA	Constant Temperature Anemometry
CV	control volume
DBD	Dielectric Barrier Discharge
DC	Direct current
DEHS	Di-Ethyl-Hexyl-Sebacat
EHD	electro hydro dynamic
Exp#	experiment number #
GB	Gigabyte
FG	function generator
FOV	fields of view
fps	frames per second
HoWK	Göttinger-type vacuum wind tunnel facility
HV	high voltage
IA	interrogation area
lam	laminar

LC-circuit	resonant circuit (inductor and capacitor)
LDA	Laser Doppler Anemometry
max	maximum
min	minimum
NB	notebook
neg	negative
NSE	Navier-Stokes equations
NWK2	Eiffel-type wind tunnel facility
OAUGDP™	One Atmosphere Uniform Glow Discharge Plasma
PIV	Particle Image Velocimetry
pos	positive
PS	power supply
RF	Radio frequency
ROI	range of interest
SD	Surface discharges
SNR	signal-to-noise ratio
turb	turbulent
TU	Technische Universität
TVM	blow-down wind tunnel facility
UAV	unmanned aerial vehicle
VD	Volume discharges
WB	weight balance
2D	two-dimensional
3D	three-dimensional

List of Figures

List of Tables

Jochen Kriegseis

Institute for
Fluid Mechanics and Aerodynamics
Technische Universität Darmstadt
Flughafenstr. 19
D-64347 Griesheim
Germany

phone: +49 6151 16-6210
fax: +49 6151 16-6246
email:
kriegseis@sla.tu-darmstadt.de

Personal

Born on September 02, 1977, in Lahn-Gießen, Germany
(German citizenship)

Education

10/2006 - 12/2011	Doctoral research in Mechanical Engineering (Dr.-Ing.), Technische Universität Darmstadt, Darmstadt, Germany
10/2000 - 09/2006	Studies in Mechanical Engineering (Dipl.-Ing.), Technische Universität Darmstadt, Darmstadt, Germany

Employment

since 10/2006	Research assistant at Institute for Fluid Mechanics and Aerodynamics, Technische Universität Darmstadt, Darmstadt, Germany
02/2006 - 09/2006	Research assistant at Department of Energy and Power Plant Technology, Technische Universität Darmstadt, Darmstadt, Germany
03/2005 - 09/2005	Research assistant at Institute for Fluid Mechanics and Aerodynamics, Technische Universität Darmstadt, Darmstadt, Germany
02/2003 - 08/2003	Teaching assistant at Institute for Product Development and Machine Elements, Technische Universität Darmstadt, Darmstadt, Germany
10/1997 - 07/1999	Professional education as Engineering Draftsman (completed) at IBF - Ingenieurbüro Fischer, Lich, Germany